Correlated low temperature states of YFe_2Ge_2 and pressure metallised NiS_2

Konstantin Semeniuk

Dissertation submitted for the degree of Doctor of Philosophy

Schoenberg Laboratory for Quantum Matter,
Cavendish Laboratory, University of Cambridge

Robinson College, University of Cambridge

Tuesday 20th March, 2018

Correlated low temperature states of YFe$_2$Ge$_2$ and pressure metallised NiS$_2$

Konstantin Semeniuk

Abstract

While the free electron model can often be surprisingly successful in describing properties of solids, there are plenty of materials in which interactions between electrons are too significant to be neglected. These strongly correlated systems sometimes exhibit rather unexpected, unusual and useful phenomena, understanding of which is one of the aims of condensed matter physics.

Heat capacity measurements of paramagnetic YFe$_2$Ge$_2$ give a Sommerfeld coefficient of about $100\,\mathrm{mJ\,mol^{-1}\,K^{-2}}$, which is about an order of magnitude higher than the value predicted by band structure calculations. This suggests the existence of strong electronic correlations in the compound, potentially due to proximity to an antiferromagnetic quantum critical point (QCP). Existence of the latter is also indicated by the non-Fermi liquid $T^{3/2}$ behaviour of the low temperature resistivity. Below 1.8 K a superconducting phase develops in the material, making it a rare case of a non-pnictide and non-chalcogenide iron based superconductor with the 1-2-2 structure. This thesis describes growth and study of a new generation of high quality YFe$_2$Ge$_2$ samples with residual resistance ratios reaching 200. Measurements of resistivity, heat capacity and magnetic susceptibility confirm the intrinsic and bulk character of the superconductivity, which is also argued to be of an unconventional nature. In order to test the hypothesis of the nearby QCP, resistance measurements under high pressure of up to 35 kbar have been conducted. Pressure dependence of the critical temperature of the superconductivity has been found to be rather weak. μSR measurements have been performed, but provided limited information due to sample inhomogeneity resulting in a broad distribution of the critical temperature.

While the superconductivity is the result of an effective attraction between electrons, under different circumstances the electronic properties of a system can instead be dictated by the Coulomb repulsion. This is the case for another transition metal based compound NiS$_2$, which is a Mott insulator. Applying hydrostatic pressure of about 30 kbar brings the material across the Mott metal-insulator transition (MIT) into the metallic phase. We have used the tunnel diode oscillator (TDO) technique to measure quantum oscillations in the metallised state of NiS$_2$, making it possible to track the evolution of the principal Fermi surface and the associated effective mass as a function of pressure. New results are presented which access a wider pressure range than previous studies and provide strong evidence that the effective carrier mass diverges close to the Mott MIT, as expected within the Brinkman-Rice scenario and predicted in dynamical mean field theory calculations. Quantum oscillations have been measured at pressures as close to the insulating phase as 33 kbar and as high as 97 kbar. In addition to providing a valuable insight into the mechanism of the Mott MIT, this study has also demonstrated the potential of the TDO technique for studying materials at high pressures.

Acknowledgements

Throughout my PhD I have been surrounded by many wonderful people, who have helped me to become a better researcher and who I have shared a lot of pleasant and memorable experiences with. I am indebted to my fellow members of the Quantum Matter group for creating such a pleasant working environment.

First of all, I would like to thank my supervisor Malte Grosche for being an invaluable mentor. His inspiring optimism and continuous trust in me have been incredibly motivating, and I sincerely appreciate numerous productive discussions we have had thanks to his approachability and open mindedness. I would also like to express a special gratitude to Patricia Alireza for teaching me the skills of working with high-pressure anvil cells. Her kind guidance in this rather challenging field has been extremely encouraging. Experiments at high magnetic field facilities would not be so successful without the insight and hard work of Jordan Baglo and Hui Chang. My everyday life both in the laboratory and outside of it has been much more exciting thanks to my good friends Philip Brown and Matthew Coak. I am also grateful to Michael Sutherland, Siân Dutton, Montu Saxena, Seb Haines, Cheng Liu, Jiasheng Chen, Keiron Murphy, Xiaoye Chen, Sofia Taylor-Coronel, Aleksandar Vasiljkovic, Paromita Mukherjee and Corentin Morice for their friendliness and helpfulness.

Last but not least, I would like to thank my parents and sister for their continued support.

Publications

Aspects of this dissertation have been published in the following journal articles and contributions at international conferences.

Papers

- Jiasheng Chen, <u>Konstantin Semeniuk</u>, Zhuo Feng, Pascal Reiss, Philip Brown, Yang Zou, Peter W. Logg, Giulio I. Lampronti, and F. Malte Grosche. "Unconventional Superconductivity in the Layered Iron Germanide". Physical Review Letters **116**, 127001, 2016

Conference presentations

- Poster: "Pressure dependence of superconductivity in YFe_2Ge_2", International Conference on Magnetism, July 5-10 2015, Barcelona, Spain.

- Poster: "Pressure dependence of superconductivity in YFe_2Ge_2", Concepts and Discoveries in Quantum Matter, July 12-15 2015, Cambridge, UK.

- Talk: "Superconductivity in YFe_2Ge_2 and its dependence on composition and pressure", German Physics Society Spring Meeting, March 6-11 2016, Regensburg, Germany.

- Poster: "Superconductivity in YFe_2Ge_2 and its dependence on composition and pressure", International Conference on Strongly Correlated Electron Systems, May 8-13 2016, Hangzhou, China.

- Talk: "Quantum oscillations in the pressure metallised Mott insulator NiS_2", German Physics Society Spring Meeting, March 19-24 2017, Dresden, Germany.

- Talk: "Quantum oscillations in the pressure metallised Mott insulator NiS_2", Frontiers in Condensed Matter, January 11-12 2018, Bristol, UK

Contents

1 Introduction

1.1 Motivation

Quantum mechanics is amongst the most advanced theories in physics ever developed. But despite its ability to predict physical properties with immense precision [1], exact application of the theory's equations is limited to systems with no more than a few particles. In order to describe a macroscopic object, such as a crystal, one has to account for all pair wise interactions between particles of the system. This has proven to be nearly impossible not just analytically but even numerically, without making various approximations. In some cases it is enough to consider the interaction of electrons with the ionic lattice in order to make sufficiently accurate predictions of properties of solid matter. However, there are systems in which electron-electron interactions are so strong that they substantially influence the physical properties and therefore cannot be neglected. These materials are known as strongly correlated electron systems and their study is central to current condensed matter research. Not only are such compounds interesting from the fundamental point of view, but they also promise useful practical applications. Phenomena caused by strong electronic correlations relevant in the context of this dissertation are superconductivity and Mott insulators.

This thesis is about two projects. The first one concerns the superconductor YFe_2Ge_2. While the field of iron-based superconductors is very active, this compound has been rather overlooked. Known iron-based superconductors with the 1-2-2 structure are almost exclusively iron arsenides, making YFe_2Ge_2 stand out as the first iron-based layered superconductor without chalcogenide or pnictide elements, even despite having a relatively low T_c just below 2 K. Its enhanced Sommerfeld coefficient, collapsed tetragonal structure (not typical for ambient conditions) and indications of unconventional superconductivity attract further interest in this material. Initial low temperature studies of YFe_2Ge_2 in the Quantum Matter group of the Cavendish Laboratory revealed the challenge of growing high quality crystals [2]. Great progress in this direction has been accomplished by Jiasheng Chen, a summer student in the Quantum Matter group at that time and now a PhD student in it. A new growth method developed by him resulted in a significant improvement of the sample quality. The study described in this thesis involved the characterisation of this new generation of YFe_2Ge_2 samples and aims to gain more insight into the properties of normal and superconducting states of the compound.

The second project is a study of the electronic structure of pressure metallised NiS_2 via quantum oscillation measurements. NiS_2 belongs to the class of compounds known as Mott insulators. They are a very clear example of how strong electron-electron interactions can drastically change properties of a material. The discovery of Mott insulators marked the beginning of the field of strongly correlated materials, but even to this day there are unanswered questions associated with the effect. Of particular interest is how the electronic structure evolves when a material is gradually tuned between conducting and insulating states. While theoretical models of such a transition have

existed for a long time, there have been few reported experimental investigations on this topic due to the challenges associated with carrying out such studies. The most established experimental techniques for probing electronic band structure are quantum oscillations and angle-resolved photoemission spectroscopy (ARPES). Tuning a Mott insulator back to the metallic state is typically done by applying physical pressure or through chemical doping. The former method requires use of pressure cells which limit access to a sample (making ARPES inapplicable) and put strict constraints on its size. The latter type of tuning inevitably makes the system more disordered, negatively affecting signal quality.

To detect quantum oscillations under pressure, we use the tunnel diode oscillator (TDO) technique. It has sufficiently high sensitivity for the task and can be adapted for samples inside anvil cells. The implementation of this method for measuring quantum oscillations in NiS_2 has been the thesis project of Hui Chang, a PhD student of the Quantum Matter group [3]. He successfully managed to detect oscillations associated with the Fermi surface in the metallic phase of NiS_2, and he tracked its evolution over a substantial pressure range. Work described in this thesis is the continuation of Hui's project, aimed at further expanding the range of pressures accessed with the TDO technique and conducting a clearer experimental observation of the electronic structure change during the Mott metal-insulator transition.

This thesis is split into six parts. The current chapter provides background information about the studied compounds. Chapter 2 outlines relevant theoretical concepts, while chapter 3 describes experimental techniques employed throughout this work. The next two parts contain the results of the studies of YFe_2Ge_2 and NiS_2. The final chapter summarises the findings and provides some concluding thoughts.

1.2   Iron-based superconductors

Certain iron containing compounds exhibiting superconductivity have been known for a considerable time [4, 5, 6, 7]. However, before the discovery of superconductivity in cuprates in 1986 [8], the strong magnetic moment of iron was believed to greatly disfavour the phenomenon. For the superconductors known at that time, described by BCS theory [9], and nowadays categorised as conventional superconductors, this statement was true, as magnetic atoms had a tendency of breaking the Cooper pairs [10]. In the cuprate superconductors, paradoxically, the magnetic moment of the copper atom was found not only to be tolerated by the superconducting phase, but also to play a crucial role in the pairing of electrons.

The history of iron-based superconductors formally starts with the discovery of superconductivity at 5 K in LaOFeP in 2006 [11]. It was, however, the observation of T_c of 26 K in electron doped LaOFeAs in 2008 [12] which really sparked a widespread interest in the iron-based compounds and started a chain of discoveries of new superconductors. The existence of high-temperature superconductivity in this family of materials, with examples such as $Sr_{0.5}Sm_{0.5}FeAsF$ ($T_c = 56$ K) [13] and $Ba_{0.6}K_{0.4}FeAs$ ($T_c = 38$ K) [14], makes iron-based compounds a viable alternative to cuprates in
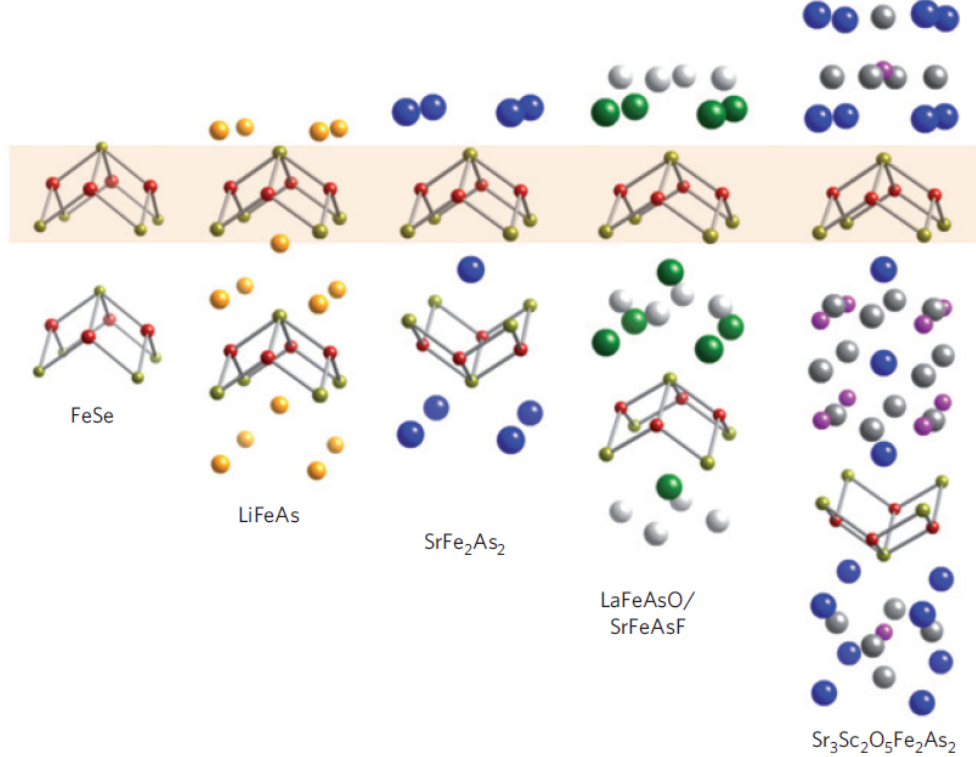
Figure 1.1: Structures of some of the iron-based superconductor families. Iron pnictide/chalcogenide layers are highlighted, with red spheres representing iron atoms (source: [16]).

applications and in pursuit of room temperature superconductivity. Moreover, a fairly broad range of electronic and magnetic properties as well as generally high critical fields and critical currents also make them quite promising materials for future practical uses [15].

Iron-based superconductors are typically divided into different groups according to the number of constituent elements and their stoichiometry. These include the more commonly known 1-1-1-1 (for example, LaFeAsO, SmFeAsO), 1-2-2 (KFe_2As_2, $BaFe_2As_2$), 1-1 (FeSe, $FeSe_{1-x}Te_x$) and 1-1-1 (LiFeAs, NaFeAs) families, as well as more exotic ones such as 2-1-3-1-1 (Sr_2ScO_3FeP [17]), 10-4-8 (($CaFe_{1-x}Pt_xAs)_{10}Pt_{4-y}As_8$ [18]) or 3-2-5-2-2 ($Ca_3Al_2O_{5-y}Fe_2As_2$ [19]). A feature that appears to be common to all these structures is the existence of layers of tetrahedrally coordinated iron and pnictogen or chalcogen atoms (Figure 1.1). Another defining characteristic of the iron-based superconductors is the prevalence of magnetic interactions. It is commonly accepted that they play an important role in the emergence of the superconductivity, which, for example, in the phase diagram of 1-1-1-1 compounds sets in after the antiferromagnetic order has been suppressed, or, in case of 1-2-2 structure, can even coexist with antiferromagnetism. A typical phase diagram of 1-2-2 type iron-based superconductors can be seen in Figure 1.2.

There does not yet exist a microscopic model which would describe from first principles how the superconductivity arises in the iron-based superconductors, along with giving a closed form expression for the critical temperature. Neither is there unanimity regarding
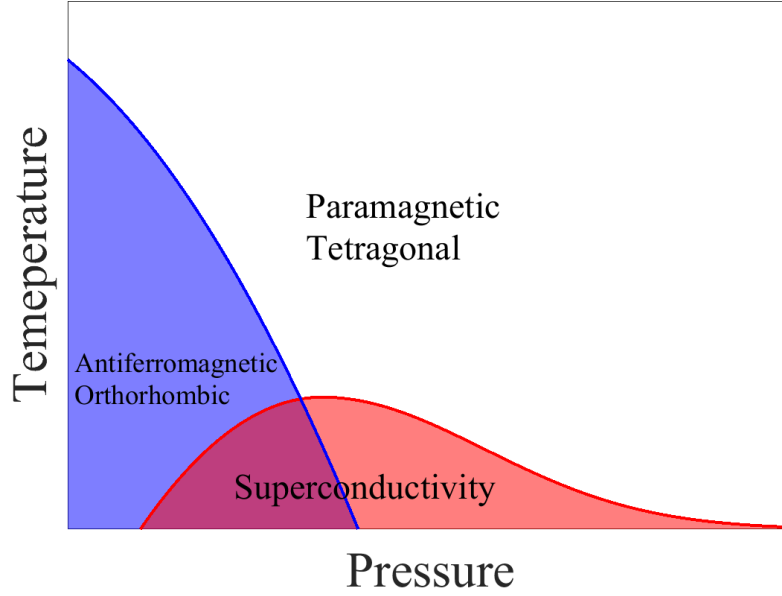
Figure 1.2: Pressure-temperature phase diagram characteristic for iron-based superconductors with the 1-2-2 struture (after [16]).

the symmetry of the superconducting gap function and the electron pairing mechanism. Perhaps the most popular description of the gap structure is believed to be the *s*-wave symmetry, in particular the $s_\pm$ [20] and s_{++} [21] models. Common elements of the Fermi surfaces of iron-based superconductors include quasi-two-dimensional cylindrical sheets [22]. In the $s_\pm$ and s_{++} models, the gap is isotropic but there is a change in sign between different Fermi sheets for $s_\pm$ whereas the sign remains unaltered in the s_{++} model. At the same time, some experiments point to the *d*-wave symmetry [23]. The pairing of electrons is most likely mediated by magnetic interactions [16], however the specifics of it as well as validity of the idea itself are still a subject of ongoing research.

1.3   Overview of YFe₂Ge₂

Despite the structural similarity to the above-listed 1-2-2 iron-based superconductors, YFe₂Ge₂ differs from them by combining iron with the group IV element germanium, rather than a pnictogen or a chalcogen. Earliest studies of the magnetic properties of rare earth iron germanides were conducted in the 70s [24, 25], but YFe₂Ge₂ in particular was first mentioned in 1986 in context of electronic structure calculations for YMn₂Ge₂, in which the former was predicted to be weakly ferromagnetic [26]. The first known explicit study of YFe₂Ge₂ was a crystallographic characterisation published in 1996 [27]. The material crystallises with a body-centered tetragonal structure, known as the ThCr₂Si₂ type structure ($I4/mmm$ symmetry, space group 139), common for 1-2-2 iron-based superconductors (Figure 1.3). The lattice constants found at the time were $a = 3.9617(5)$ Å and $c = 10.421(1)$ Å with the z coordinate of atomic position of Ge atom being 0.3789(3). It must be noted that in YFe₂Ge₂ there exists a covalent bond between adjacent Ge atoms, making iron have the oxidation state of $+1.5$, compared to $+2.5$ in KFe₂As₂, which would superficially appear to be isoelectronic to YFe₂Ge₂, but
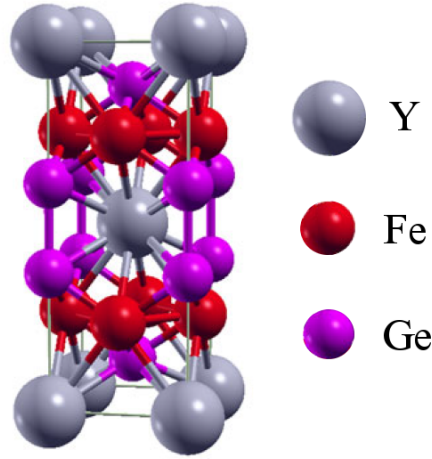
Figure 1.3: Unit cell of YFe$_2$Ge$_2$.

has no As-As bonds. This difference between the two compounds also manifests itself as a discrepancy in the aspect ratio of their respective unit cells. The ratio of c and a lattice parameters for YFe$_2$Ge$_2$ is 2.64, giving it a much stronger three-dimensional character than KFe$_2$As$_2$, with $c/a = 3.608$ [28]. It is noteworthy that the collapsed tetragonal phase can be induced in KFe$_2$As$_2$ at hydrostatic pressure of about 13–15 GPa [29, 30]. The structural transition brings the c/a ratio of the KFe$_2$As$_2$ unit cell down to a value close to that of the YFe$_2$Ge$_2$ unit cell and increases the critical temperature of superconductivity by a factor of more than 3.

The low temperature properties of YFe$_2$Ge$_2$ were unknown until a study of resistivity, magnetisation and heat capacity of rare earth iron germanide single crystals by Avila et al. was published in 2004 [31]. The investigated materials included the two sibling compounds YFe$_2$Ge$_2$ and LuFe$_2$Ge$_2$, properties of which were measured down to 2 K. Magnetic susceptibility data (Figure 1.4, left) indicated that the former was a paramagnet with a small upturn attributed to ferromagnetic impurities, while the latter exhibited a clear anomaly at 9 K, which at the time was thought to be the onset of charge or spin density wave order. The anomaly also manifested itself in the heat capacity (Figure 1.4, right), while YFe$_2$Ge$_2$ was found to have a high Sommerfeld coefficient of about 100 mJ mol^{-1} K^{-2}, indicating strong electronic correlations. Both compounds had very similar electrical resistivity with a temperature dependence characteristic for metals and a very weak trace of the 9 K anomaly for LuFe$_2$Ge$_2$.

LuFe$_2$Ge$_2$ was subsequently studied by neutron diffraction [32], which identified the 9 K anomaly as the onset of antiferromagnetic order. Iron moments were found to be ferromagnetically ordered within a basal plane with antiferromagnetic coupling between the layers. The same study also investigated the effect of hydrostatic pressure on the ordering temperature. It was found that increasing pressure up to at least 3 GPa enhances antiferromagnetism (Figure 1.5). Contrary to the effect of pressure, substituting lutetium by yttrium reduces the ordering temperature, which is consistent with yttrium having a larger atomic radius than lutetium [33, 34]. While the studied compositions did not extend to the point of complete suppression of the antiferromagnetism, the extrapolation
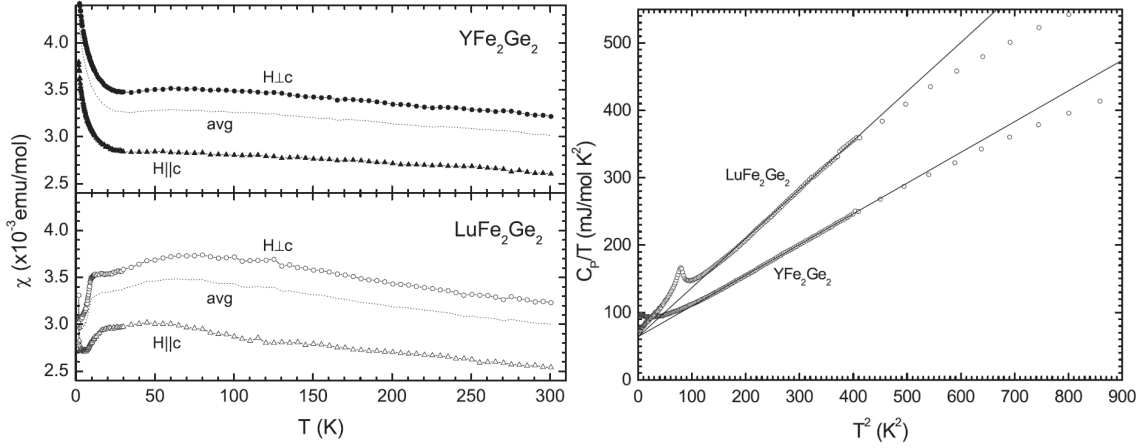
Figure 1.4:   Magnetic susceptibility (left) and heat capacity (right) of YFe_2Ge_2 and $LuFe_2Ge_2$ against temperature [31].

suggested that replacing roughly 20% of lutetium atoms with yttrium should bring the Néel temperature down to zero (Figure 1.5). The resultant phase diagram resembles the typical scenario leading to the emergence of superconductivity in iron-based compounds. One might therefore hypothesise that the complete suppression of the antiferromagnetic order marks a quantum critical point (QCP) surrounded by a dome of superconducting phase, which could possibly extend to YFe_2Ge_2. Another potential way of approaching the QCP could be applying hydrostatic pressure to YFe_2Ge_2. None of the studies described above, however, detected superconductivity in the explored temperature range with the minimum of 2 K.

A study of YFe_2Ge_2 down to sub-Kelvin temperatures by Zou et al. [35] did eventually reveal the superconductivity (a more detailed description of the study is presented in the PhD thesis of Yang Zou [2]). The T_c was found to correlate quite strongly with the purity of the samples, quantified by the residual resistivity ratio (RRR). It was discovered that annealing the material in vacuum or argon at 800 °C for 7 days leads to a significant improvement of the quality of the samples, increasing their RRR from just above 20 to about 50. For a sample with RRR = 41 onset of superconductivity in resistivity measurements was at 1.8 K, while the complete suppression of resistance happened at 0.6 K. Dirtier samples showed lower transition temperatures and sometimes failed to become perfectly conducting by 0.35 K (the lowest temperature of the cryostat). Remarkably, single crystals grown by the flux method generally had a substantially lower RRR and T_c than polycrystalline samples produced using the induction melting. Based on the resistivity measurements in magnetic field, the upper critical field was found to be 1.65 T (Figure 1.6). A diamagnetic signature consistent with the superconductivity was also observed in the magnetic susceptibility. Heat capacity measurements, on the other hand, did not show a clear anomaly characteristic for a transition into a superconducting state (Figure 1.6). While the observed behavior of the heat capacity could be a result of a broad distribution of T_c within the sample, absence of the clear signature did not allow one to conclude that the superconductivity was intrinsic to YFe_2Ge_2. The observed transition could have been, in
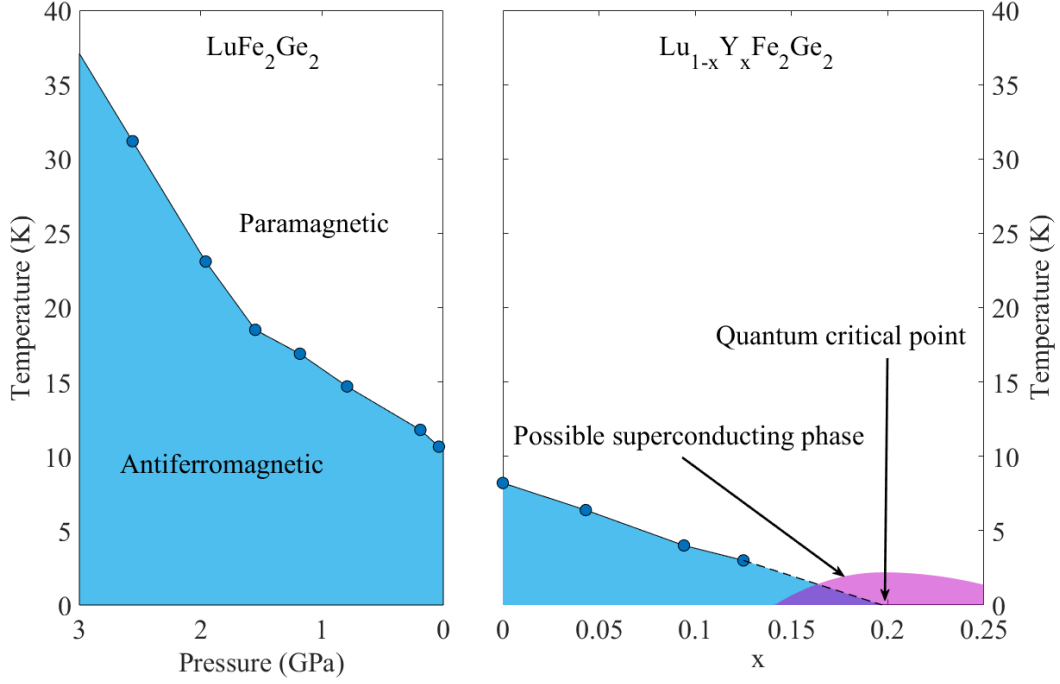
6

Figure 1.5:   Effect of hydrostatic pressure and Lu substitution by Y on the Néel temperature of LuFe$_2$Ge$_2$ (using data from [32, 34]).

principle, caused by an alien phase, or the superconductivity could be filamentary in nature.

YFe$_2$Ge$_2$ samples were also characterised via powder X-ray diffraction. The resultant lattice constants of $a = 3.96447$ Å and $c = 10.45368$ Å were consistent with the previously reported values [31]. Analysis of the diffraction pattern indicated that the material contained a small amount of iron and germanium based alien phases. The exact amount of them varied across different samples, but did not exceed 5% in weight. It was, however, noted that some of the inclusions were ferromagnetic, which could affect measurements of certain properties.

The paper by Zou et al. also mentions the non-Fermi liquid behaviour of the normal state resistivity at low temperatures. As can be seen in Figure 1.6, above T_c, the resistivity follows a power law temperature dependence with the exponent 3/2. Such behaviour is consistent with YFe$_2$Ge$_2$ being located in a quantum critical regime, caused by close proximity to the antiferromagnetic quantum critical point. A high pressure study did not provide conclusive information regarding the location of the QCP. Suppression of the critical temperature was observed in magnetic susceptibility measurements, but no significant variation of the resistive T_c was detected up a pressure of 25 kbar.

At around the same time a similar study was independently conducted by the Ames Laboratory group of the Iowa State University using single crystals of YFe$_2$Ge$_2$ grown in tin flux [36]. Immediately after the growth, the samples did not show any signs of superconductivity. The transition was only observed after annealing the crystals. The best parameters were obtained after about one week of annealing at approximately 500°C – 600°C. Such treatment resulted in observation of a full transition to a superconducting
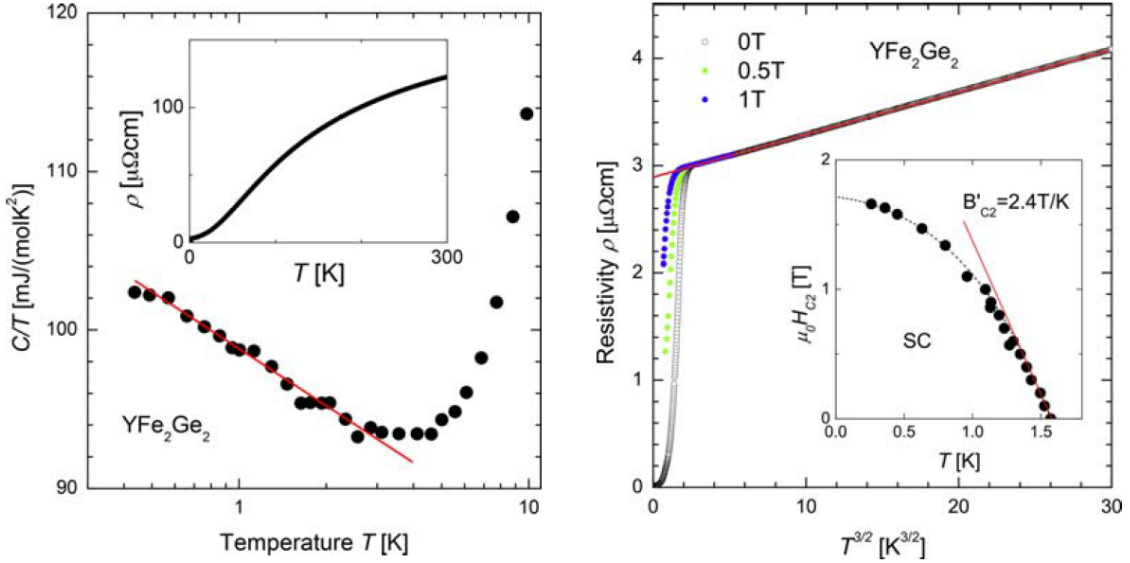
Figure 1.6: Results of the measurements of electronic and thermodynamic properties of YFe$_2$Ge$_2$ from the study of Zou et al. [35]. Left: Heat capacity divided by temperature as a function of temperature; inset shows the electrical resistivity across 0 to 300 K temperature range (RRR = 41). Right: Low temperature resistivity and the transition to the superconducting state at different magnetic fields; upper critical curve is shown in the inset.

state in resistivity. The transition was centered at 1.2 K and had an extent of about 0.4 K, making it noticeably sharper than in the polycrystalline samples of Zou et al. The specific heat measurements did not reveal any signatures associated with the transition (Figure 1.7). The authors proposed that the observed superconductivity is either strain stabilised and associated with stressed YFe$_2$Ge$_2$ at twin boundaries and dislocations or comes from another undetected crystalline phase.

Soon after superconductivity in YFe$_2$Ge$_2$ was first discovered, a first principles calculation of its electronic structure and magnetic interactions was performed by Subedi [37]. Density functional theory calculations within the local density approximation (LDA) predicted a Fermi surface structure consisting of five sheets: a cylindrical electron pocket centered at the X point of the Brillouin zone, a large three dimensional disc shaped hole pocket situated around the Z point, enclosing a cylindrical and two almost spherical hole pockets. The band structure near the Fermi level was found to be heavily influenced by the 3d states of iron. Presence of a Ge-4p_z character band on either side of the Fermi level indicated a covalent bond between germanium ions, consistent with the collapsed tetragonal structure. The calculated Sommerfeld coefficient was 10.63 mJ mol^{-1} K^{-2}, which is less than the experimental value by almost an order of magnitude. It was proposed that antiferromagnetic spin fluctuations give rise to a singlet $s_\pm$ superconductivity, similar to some other iron-based superconductors [38, 20]. Relatively low T_c was noted and was attributed to a competition between different magnetic configurations located energetically quite close to each other (corresponding Fe moments lay within the 0.6 μ_B to 0.8 μ_B range). This phenomenon was also proposed to be responsible for driving the non-Fermi liquid behaviour.
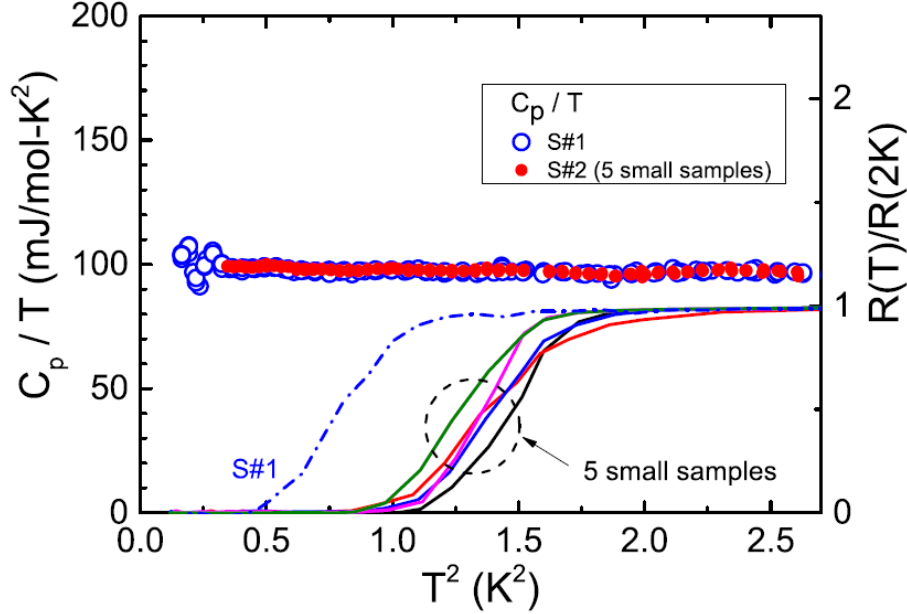
Figure 1.7: Heat capacity divided by temperature and relative resistance of annealed YFe_2Ge_2 single crystals as functions of temperature. Data from the Ames Laboratory [36].

Another computational analysis was simultaneously performed by Singh [39]. Instead of using the LDA for the exchange correlation functional, the author employed the Perdew, Burke, and Ernzerhof generalised gradient approximation (PBE GGA). The results are in overall agreement with those of Subedi, with slight differences concerning the magnetic structure. Similar Fermi surfaces were obtained with the 3-dimensional character being emphasized. The disk shaped Fermi surface centered at the Z point was marked as the dominant pocket for determining the electronic properties of YFe_2Ge_2. Calculations also significantly underestimated the Sommerfeld coefficient by a similar factor. In-plane ferromagnetic interaction of itinerant Stoner type was identified as the primary driver of magnetism. Antiferromagnetic stacking of layers was favoured, although magnetic interaction between the iron planes was found to be very weak. The dominant interaction resulted in an iron moment of about 1 μ_B. Electronic interlayer coupling, on the other hand, turned out to be significant, with the conductivity along the c axis predicted to be the highest. YFe_2Ge_2 was proposed to be either a triplet superconductor with pair interactions mediated by ferromagnetic spin fluctuations or a conventional electron-phonon superconductor with the T_c strongly suppressed by the magnetism.

The next iteration of the investigation of YFe_2Ge_2 in Cambridge started with another refinement of the material production. Using purer reactants and an optimised annealing schedule polycrystalline samples with RRR reaching 200 were obtained [40]. Study of this new generation of YFe_2Ge_2 samples is a topic of this thesis.

1.4 Mott transition

According to simple band theory of solids, compounds with partially filled bands are conductors, but already in 1937 it was noted [41] that many transition metal oxides with partially filled *d*-electron bands are rather poor conductors or even insulators. The proposed explanation [42] of this phenomenon revolved around the electrostatic repulsion between electrons, which reduces their mobility. The idea was correct and it pointed out the limitations of the free electron model, effectively starting the field of strongly correlated electron systems. The insulating behaviour of many materials, which are superficially expected to be metals, is understood as the effect of electronic interactions, which drive the system through a metal-insulator transition (MIT). Nevill Mott did a lot of early work [43] on developing a theoretical description of insulating compounds with singly occupied orbitals, and today these systems are known as Mott insulators.

The phenomenon of Mott localisation can be illustrated with a lattice of orbitals, each accommodating up to two electrons. When the system is half-filled (one electron per lattice site), ability of electrons to hop between neighbouring orbitals (manifesting as electrical conductivity) is determined by the competition of two effects. Good overlap between the orbitals makes it more likely for electrons to move, but when one electron hops into an adjacent site already containing another electron, the resultant double occupancy increases the potential energy of the system due to the repulsive Coulomb interaction. Mathematically this description is formulated as the Hubbard Hamiltonian:

$$H = -t \sum_{\langle i,j \rangle, \sigma} \left(\hat{c}^{\dagger}_{i,\sigma} \hat{c}_{j,\sigma} + \hat{c}^{\dagger}_{j,\sigma} \hat{c}_{i,\sigma} \right) + U \sum_{i=1}^{N} \hat{n}_{i\uparrow} \hat{n}_{i\downarrow}, \tag{1.1}$$

where $\hat{c}^{\dagger}_{i,\sigma}$ and $\hat{c}_{i,\sigma}$ are respectively operators for creating and annihilating an electron with spin σ on site i. Operators $\hat{n}_{i\uparrow}$ and $\hat{n}_{i\downarrow}$ count the number of electrons on site i of the corresponding spin (up or down). Expression $\langle i, j \rangle$ stands for all the pairs of adjacent lattice sites, and N is the total number of sites. The parameter t is called the overlap integral and is directly related to the electronic bandwidth W (the direct relationship between the two parameters can be seen in, for example, the tight binding model). U is the energy penalty associated with the double occupancy of one lattice site. The degree to which the electrons are free to move is quantified by the relative magnitudes of W and U. If $U/W \ll 1$, then the hopping is not significantly impeded, which results in metallic behaviour, described by a single half filled band. As the ratio increases, the Coulomb repulsion becomes stronger relative to the kinetic energy of electrons, making hopping less and less likely. Eventually U becomes dominant enough for the electrons to become localised on their lattice sites and the system turns insulating. The resultant regime is described by two bands (called the Hubbard bands) separated by a gap. The lower band corresponds to the states occupied by the unpaired electrons and is full, while the upper band represents the states of doubly occupied orbitals. Such a change from the metallic to the insulating state while the system remains half-filled known as the bandwidth-controlled Mott MIT. An alternative scenario is the filling-controlled Mott
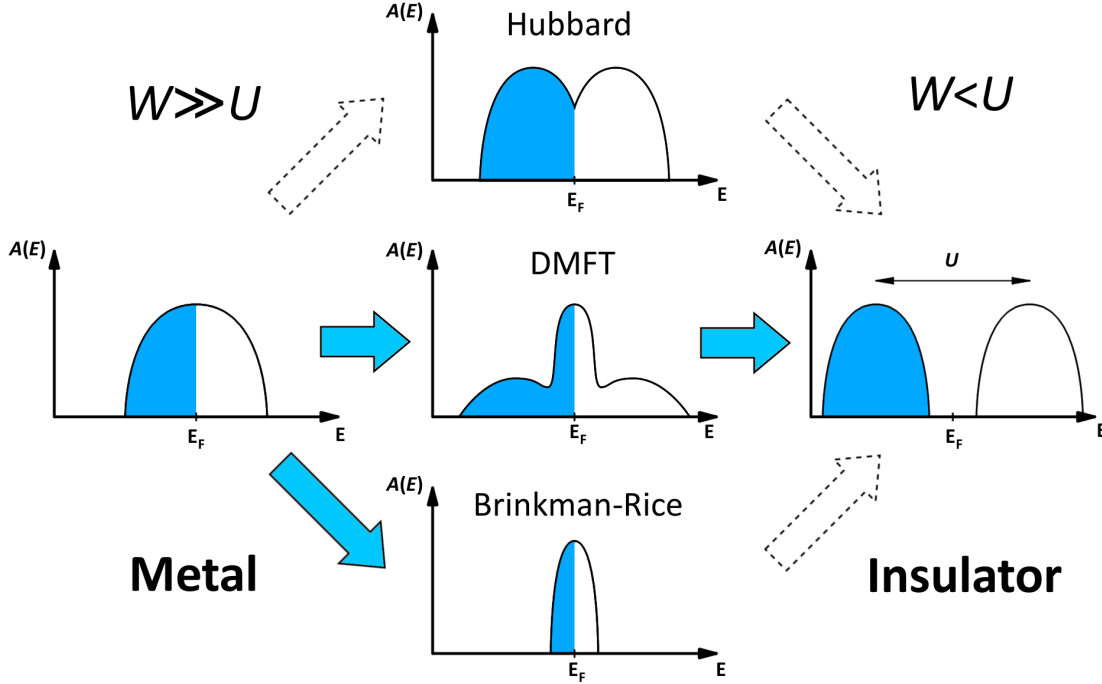
Figure 1.8: Schematic evolution of the *d*-band spectral function during the Mott metal-insulator transition according to various theoretical descriptions. *W* is the energy range of the *d*-band, and *U* is the on-site Coulomb repulsion energy.

MIT, in which U/W remains large and constant, while the transition is induced by tuning the material towards the half-filling with charge doping. The former control mechanism is the relevant one in context of this dissertation.

Even though the model above can be represented with a rather simple Hubbard Hamiltonian, a proper quantitative description of the Mott MIT has proven difficult to achieve. Several approaches are mentioned below and are summarised in Figure 1.8. The Hubbard approximation [44] neglects dynamic charge fluctuations, but manages to correctly predict two Hubbard bands of separation U between their centers in the insulating state and a single band well within the metallic state. The resultant evolution of the spectral function between the two states, however, implies a gradual increase of the Fermi surface volume upon entering the metallic state. This contradicts Luttinger's theorem, which states that the Fermi surface volume is determined by the electron density and is not changed by interactions. A better description of the metallic state is provided by the Brinkman-Rice model [45] using the Gutzwiller approximation [46]. According to this model, the width of the quasiparticle band in the metallic state decreases, and the effective mass diverges upon approaching the phase boundary from the metallic side. At the critical value of U, the metallic band narrows down to zero and disappears. The obvious drawback of the Brinkman-Rice model is that it does not describe the appearance of the Hubbard bands in the insulating state. A numerical approach based on the dynamical mean-field theory (DMFT) [47] takes care of the problems of both previously mentioned models. According to it, as the spectral function peak in the metallic state becomes more narrow with increasing U/W, the Hubbard
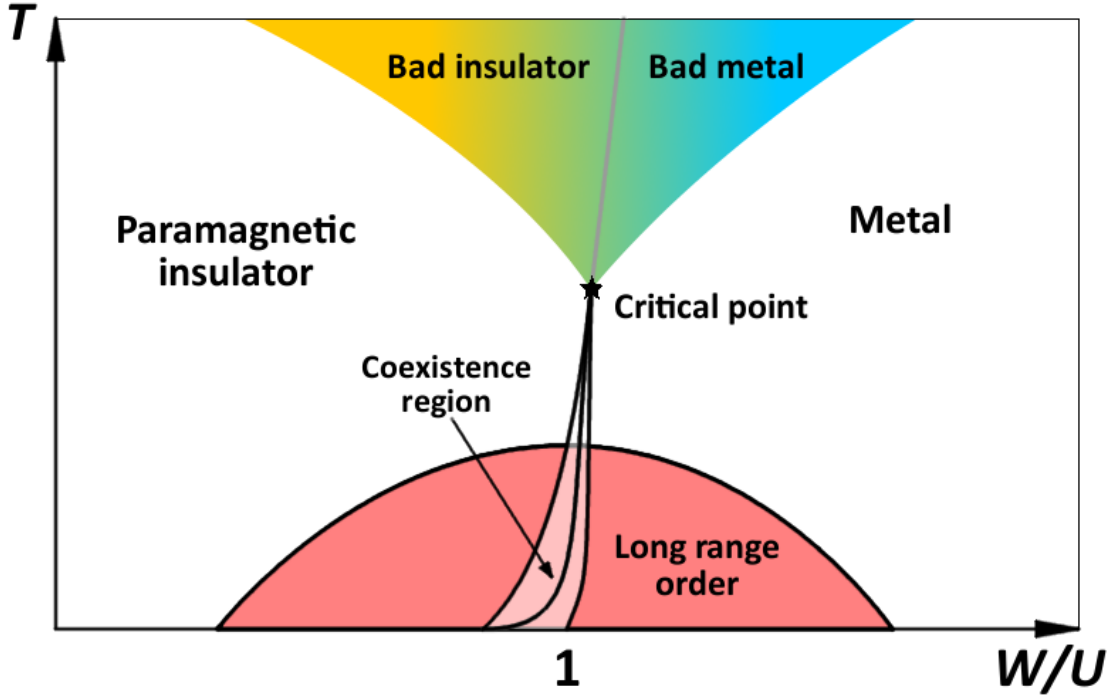
Figure 1.9: Schematic phase diagram of a system with a partially filled band as a function of correlation strength and temperature, as described by dynamical mean-field theory (after diagram from reference [48]).

bands start to emerge and are fully formed as the peak shrinks to zero. Like in the Brinkman-Rice model, the divergence of the effective quasiparticle mass is also expected.

The DMFT predicts a characteristic phase diagram as a function of temperature and W/U (the ratio is inverted for easier comparison with the experimental phase diagram presented in the next section), schematically displayed in Figure 1.9. At low temperature, long range magnetic order sets in in the vicinity of the MIT. The character of the order is material specific. There exist distinct solutions corresponding to metallic and insulating states which can coexist in a certain region, indicated on the diagram by the light pink area. The solid line in the middle of the coexistence region is the first order transition line which terminates with the second order points at $T = 0$ and at a finite temperature critical point [47]. Above the critical point, there is a so called Mott critical regime in which the change between the metallic and the insulating states happens continuously upon increasing the interaction strength.

It is common for lattices of Mott insulators to consist of transition metal cations separated by anions (V_2O_3, NiO). Hopping of electrons between the metal atoms is mediated by the p orbitals of the anions. In such systems there are two scenarios of the bandwidth controlled Mott MIT that can be distinguished (illustrated in Figure 1.10). In Mott-Hubbard insulators the band gap opening in the insulating state is formed just by the Hubbard bands. However, if the top of the lower Hubbard band lies lower in energy than the top of the anion p band, the band gap exists between the upper Hubbard band and that p band. Systems where this is the case are called charge transfer insulators [49]. While the previous paragraphs used an example of the Mott-Hubbard
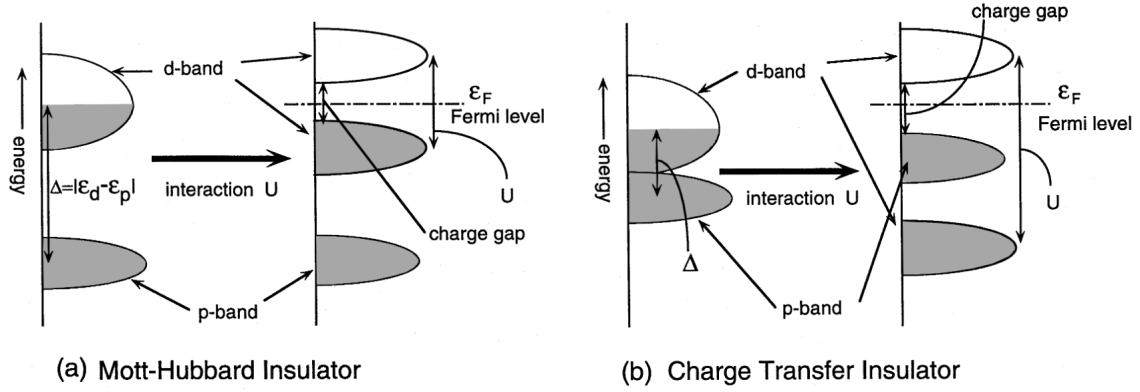
Figure 1.10: Schematic illustration of the difference between Mott-Hubbard (a) and charge transfer (b) insulators (from reference [53]).

configuration, calculations performed for the charge transfer insulator $NiS_{2-x}Se_x$ show that the mechanism of Mott MIT predicted by the DMFT is also valid for charge transfer insulators [50, 51, 52].

Despite the fact that detailed theoretical descriptions of the bandwidth controlled Mott MIT had been produced more than two decades ago, not many attempts to verify the predictions experimentally were reported since. Photoemission spectroscopy studies conducted on $NiS_{2-x}Se_x$ [54] and $Ca_{1-x}Sr_xVO_3$ [55] were generally in agreement with DMFT, although with minor deviations. Quantum oscillations were measured in some pressure tuned charge transfer salts [56, 57], and effective mass enhancement was detected. No such studies have been conducted on clean transition metal based systems before recent measurements of quantum oscillations in NiS_2 under high pressure.

1.5   Overview of NiS₂

The study of Mott transitions started about 80 years ago with the realisation that NiO was an excellent insulator, while the theory existing at that time predicted it to be a conductor, due to partially filled d bands [42]. Experimental investigation of the pressure induced MIT in this compound is barely feasible even to this day, as pressure over 240 GPa is needed to metallise it fully [58]. Other Mott insulators have been discovered since then and NiS_2 is one such example. The pyrite NiS_2 is closely related to NiO, as they both crystallise in a NaCl type face centered cubic structure, with O^{2-} anions replaced by S_2^{2-} dimers. On the other hand, NiS_2 becomes metallic at merely 3 GPa and thus is a much better candidate for high pressure experiments. An alternative route towards the metallic phase is isovalent substitution of sulfur by selenium. Metallisation occurs at around the $NiS_{1.55}Se_{0.45}$ composition. One has to be cautious when drawing parallels between the two ways of tuning, as chemical pressure is unavoidably associated with disorder.
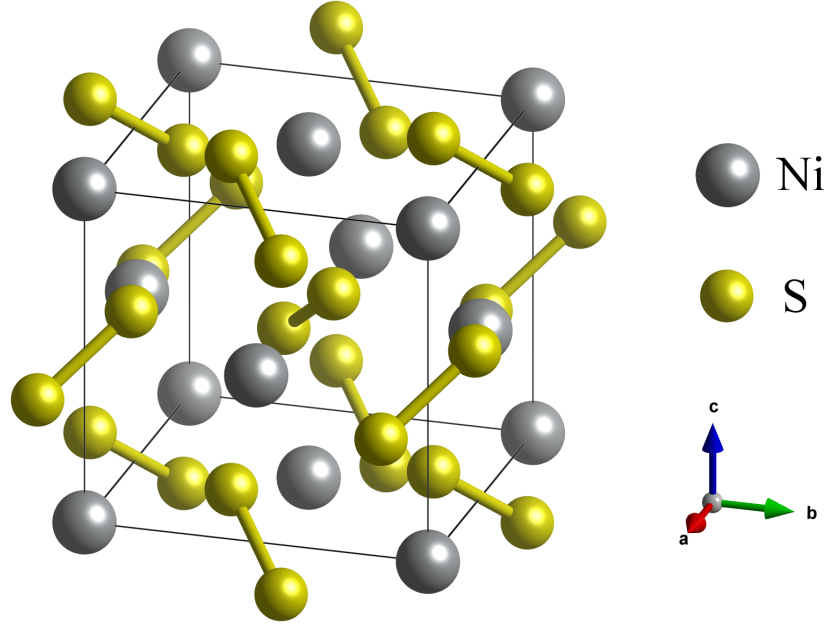
Figure 1.11: NiS$_2$ crystal lattice structure. Black lines mark the unit cell.

The crystal structure of NiS$_2$ is displayed in Figure 1.11. At ambient pressure the lattice constant is 5.6894 Å [59]. NiS$_2$ has a reduced symmetry compared to NaCl due to varying orientations of the dimers' axes. High pressure induces a structural transition into a slightly monoclinic phase with $a = 5.5748(9)$ Å, $b = c = 5.5853(6)$ Å and $\beta = 89.949(1)°$ at 38.6 kbar [60]. The same study suggests that the transition happens over a broad pressure interval, starting at 8.5 kbar in some parts of the crystal and completing by 28.4 kbar. Recent measurements [3] conducted on tellurium flux grown samples (also used in this study) are generally in agreement with the earlier results.

The pressure-temperature phase diagram of NiS$_2$ compiled from the results of various experimental studies [61, 62, 63] is shown in Figure 1.12. Antiferromagnetic long range order is dominant at low temperature in the vicinity of the MIT, in accordance with the DMFT prediction. At ambient pressure, antiferromagnetism with (1,0,0) wavevector develops at 38 K with non-collinear spin arrangement. Below 30 K it coexists with another antiferromagnetic structure with (1/2,1/2,1/2) wavevector and weakly ferromagnetic order due to canting of antiferromagnetically ordered spins [64, 65, 66]. For a given pressure, insulator-metal transition occurs in several stages spread over a temperature interval of up to 30 K (Figure 1.12 inset). Published information on magnetic structure of NiS$_2$ close to the MIT and in the metallic phase is limited to results of transport measurements [62] or studies of the Se doped compound [67]. Based on these sources, one can expect the high temperature antiferromagnetic structure of the insulating state to survive the transition and get gradually suppressed at higher pressures. The Néel temperature most likely falls to zero at around 76 kbar, when the A coefficient of the temperature dependence of resistivity ($\rho = \rho_0 + AT^2$; ρ – resistivity, T – temperature) exhibits a peak [68]. Little is known about the nature of this critical point. It was proposed that for pure NiS$_2$ the transition is first order, while for the doped and hence more disordered systems, it becomes second order [62].
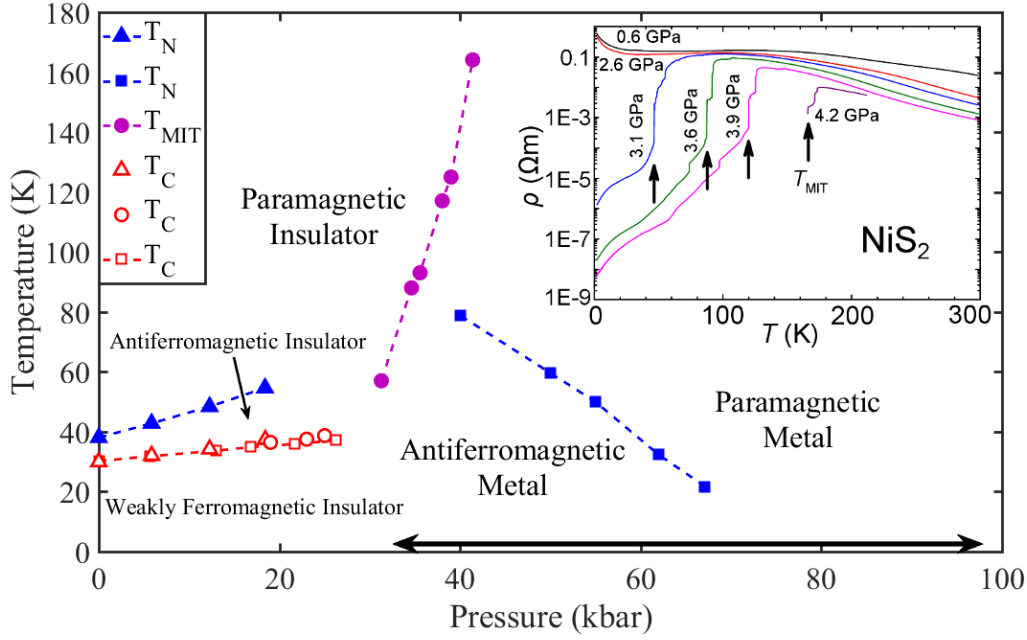
Figure 1.12: Phase diagram of NiS$_2$ according to the experimental studies (triangles – [61], blue squares – [62], circles and red squares – [63]). T_C, T_N and T_{MIT} stand for Curie, Néel and metal-insulator transition temperatures respectively. Double headed arrow indicates the pressure range spanned by this study. Resistivity as a function of temperature [63] is shown in the inset, arrows indicate the metal-insulator transition temperatures.

The electronic structure of NiS$_2$ involves $3d$ orbitals of Ni^{2+} ion and $3p$ orbitals of sulfur in form of S$_2^{2-}$ dimers. Five Ni $3d$ orbitals are split by the crystal field into three filled t_{2g} orbitals and two singly occupied e_g orbitals. Strong Coulomb repulsion between electrons on Ni^{2+} sites causes the partially filled e_g band to split into lower and upper Hubbard bands (Figure 1.13). Calculations, however, show that the band gap exists between the upper Hubbard band and a broad band due to π-antibonding molecular orbitals of sulfur dimers ($pp\pi^*$ band). According to the previously mentioned classification this makes NiS$_2$ a charge transfer insulator [69, 70].

Density functional theory (DFT) calculations suggest that applying hydrostatic pressure to NiS$_2$ reduces the distance between Ni and S atoms without changing the length of the dimers [71]. This increases the overlap between the Ni $3d$ and S $3p$ orbitals. The corresponding bands move towards each other and eventually close the band gap, turning the compound into a metal.

In-house DFT calculations using the generalised gradient approximation exchange-correlation functional [72] were performed in Wien2K in order to predict the electronic structure of NiS$_2$ in the metallic state [3]. The ambient-pressure cubic lattice was used, but electronic correlations beyond DFT and magnetic order were neglected. The results were therefore expected to be valid in the paramagnetic state far away from the MIT. Spin-orbit coupling was included, but its effect was found not to be significant. The resultant band structure close to the Fermi level was dominated by the Ni-d contribution (which was about 3 times stronger than the S-p one) and is displayed in Figure 1.14.
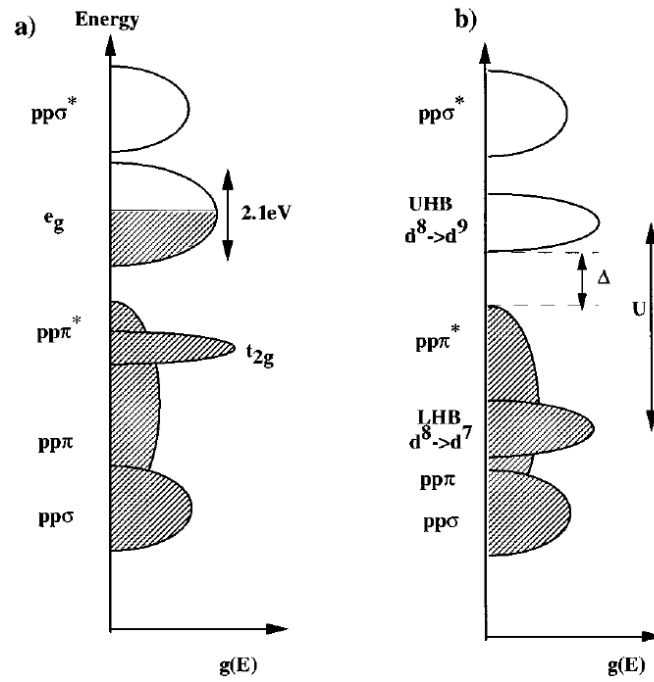
Figure 1.13: Schematic representation of NiS$_2$ spectral function: a) without and b) with intra-atomic Coulomb repulsion on Ni$^+$ sites according to the LDA calculation [69]. e_g band formed by the $3d$ orbitals of Ni splits into the upper (UHB) and lower (LHB) Hubbard bands.
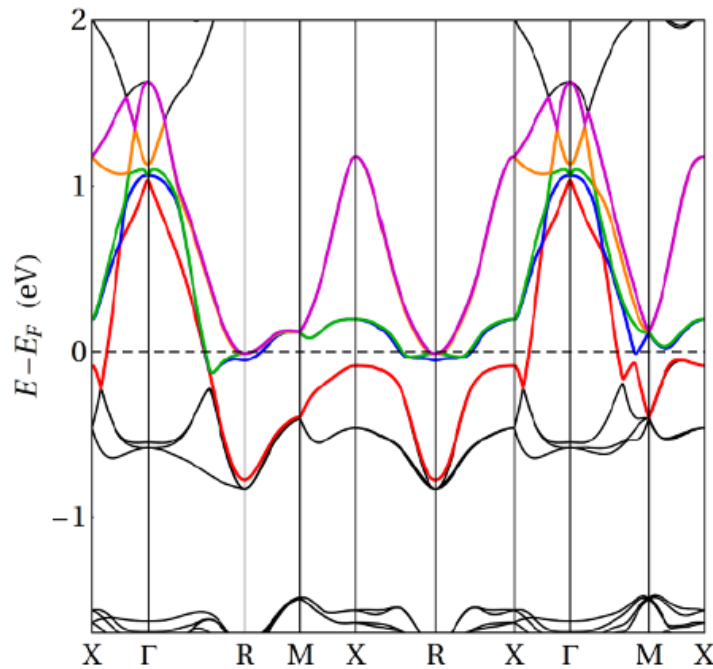
Figure 1.14: Band structure of NiS$_2$ in metallic state, according to the in-house DFT calculations [3].
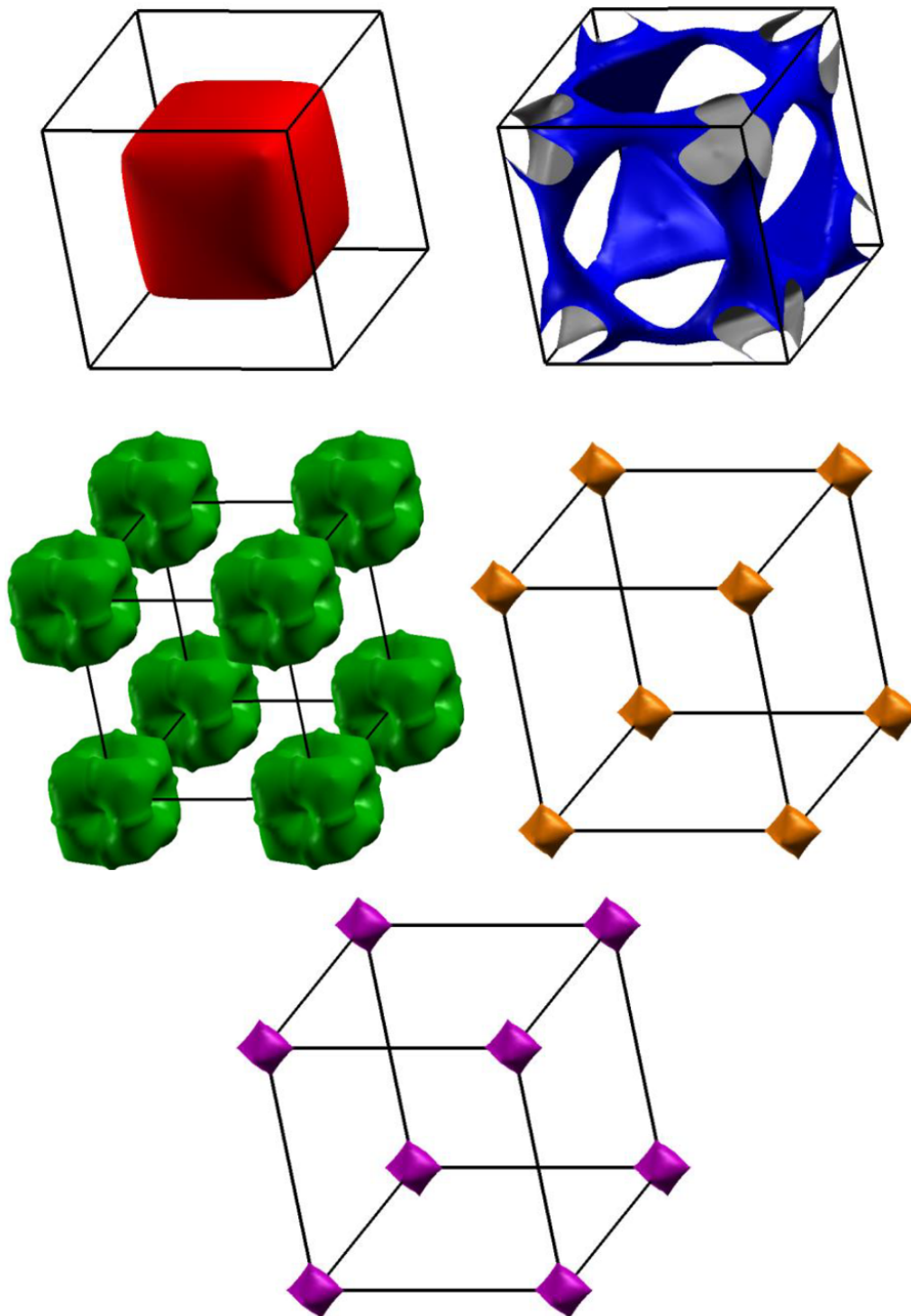
Figure 1.15: Shapes of the Fermi surfaces in metallic NiS$_2$ according to the in-house DFT calculations [3]. Colours are consistent with Figure 1.14.
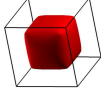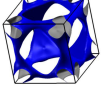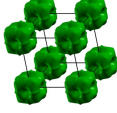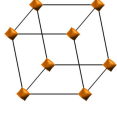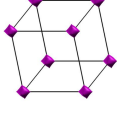
Fermi surface	Carrier type	Effective mass (m_e)	Quantum oscillations frequency (kT)
	Holes	0.8	6.23
	Electrons	0.3 5.3	0.07 2.67
	Electrons	4.5 2.0	2.46 3.00
	Electrons	1.3	0.30
	Electrons	1.4	0.31

Table 1.1: Carrier types and band masses as well as quantum oscillation frequencies of the Fermi surfaces of NiS₂ according to the in-house DFT calculations [3]. The frequencies correspond to the magnetic field applied along one of the principal crystallographic axes.

The corresponding Fermi surfaces are displayed in Figure 1.15, and their properties are summarised in Table 1.1. There are five bands crossing the Fermi level, giving rise to four electron and one hole Fermi surfaces. The latter one has by far the largest volume, which is consistent with NiS₂ being a compensated metal. That being said, the cubic Fermi surface only contributes approximately 11% of the total density of states. 59% and 26% come from the Fermi surfaces coloured blue and green respectively, and the rest is accounted for by the smallest two.

The first successful experimental investigation of the electronic structure of metallised NiS₂ (as opposed to the Se doped variant) was conducted in 2014 in the National High Magnetic Field Laboratory in Tallahassee (NHMFL) by members of the Quantum Matter group of the Cavendish Laboratory. Quantum oscillations in NiS₂ under high pressure were observed using a tunnel diode oscillator technique in conjunction with a moissanite anvil cell [63]. At a pressure of 37.8 kbar and temperatures above 0.3 K oscillations at about 6 kT frequency were detected. The corresponding effective mass was approximately 4 electron masses.

Several subsequent experiments were performed in the Cavendish Laboratory, the NHMFL and the High Field Magnet Laboratory in Nijmegen (HFML). Results described in the rest of this chapter, summarised in Figures 1.16, 1.17 and 1.18, come from the thesis of Hui Chang [3] and do not contain the new data presented in this thesis. Measurements conducted as of summer 2016 spanned the pressure interval between 37 kbar and 55 kbar. Quantum oscillations of about 6 kT frequency have been
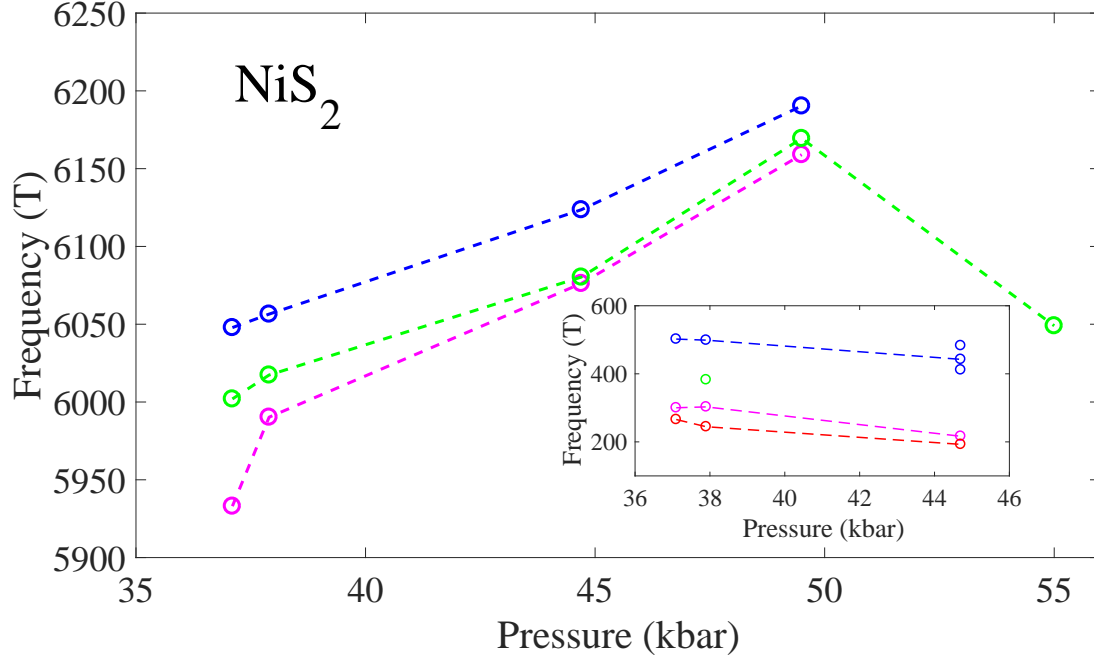
Figure 1.16: Summary of quantum oscillation frequencies detected in pressure metallised NiS_2 as of summer 2016 [3] (data presented in this thesis is not included). High frequencies are shown in the main plot, while the inset contains low frequencies.

consistently observed, however at certain pressures, the analysis showed that the signal could be interpreted as a sum of oscillations at three close-lying frequencies. In some field sweeps, much lower frequency oscillations were resolved. The effective masses varied between 2.6 and 5.4 electron masses for the high frequencies and between 1 and 6 for the low frequencies. The mean free paths were in the range of 80-280 nm and 16-35 nm for high and low frequencies respectively.

So far the high frequency oscillations have been predominantly considered when interpreting the results. Genuineness of the low frequency oscillations is still a matter of discussion, since the Fourier spectrum is generally rather noisy in the corresponding range and vulnerable to artifacts resulting from the data processing. With five pressure points, the overall trend seems to exist but it is not very pronounced. The effective mass, according to the expectations, does in general increase upon moving closer to the MIT, but the 50 kbar point seems rather out of place. While the frequency does appear to change with pressure, the relative variation is less than 5%. That being said, the increase between 38 kbar and 50 kbar cannot be accounted for by the compression of the lattice alone and could imply a change in the carrier concentration. The frequency value at 55 kbar is unreliable as it clearly does not follow the established trend. Mean free path values are of the correct order of magnitude, but no pattern seems to exist over the studied pressure range.

Based on the DFT calculations described above, the quantum oscillations at 6 kT frequency can be associated with the large hole Fermi surface. A rotation study was performed to check this hypothesis and produced results in good enough agreement with
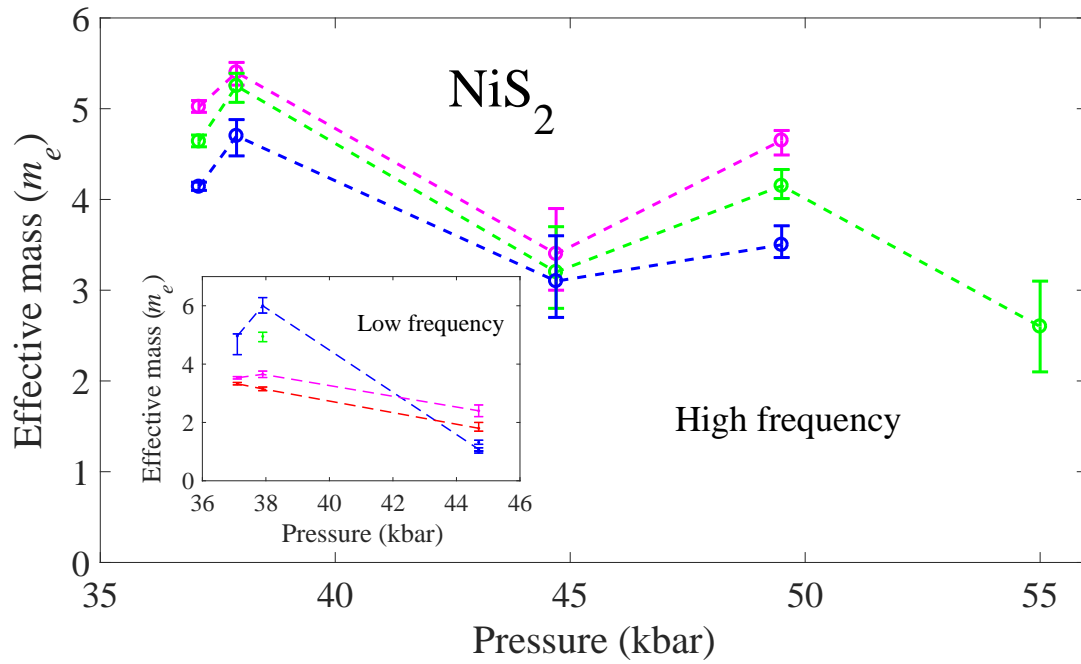
Figure 1.17: Effective masses associated with the oscillation frequencies presented in Figure 1.16. Matching frequencies and masses are marked with the same colour in both figures.
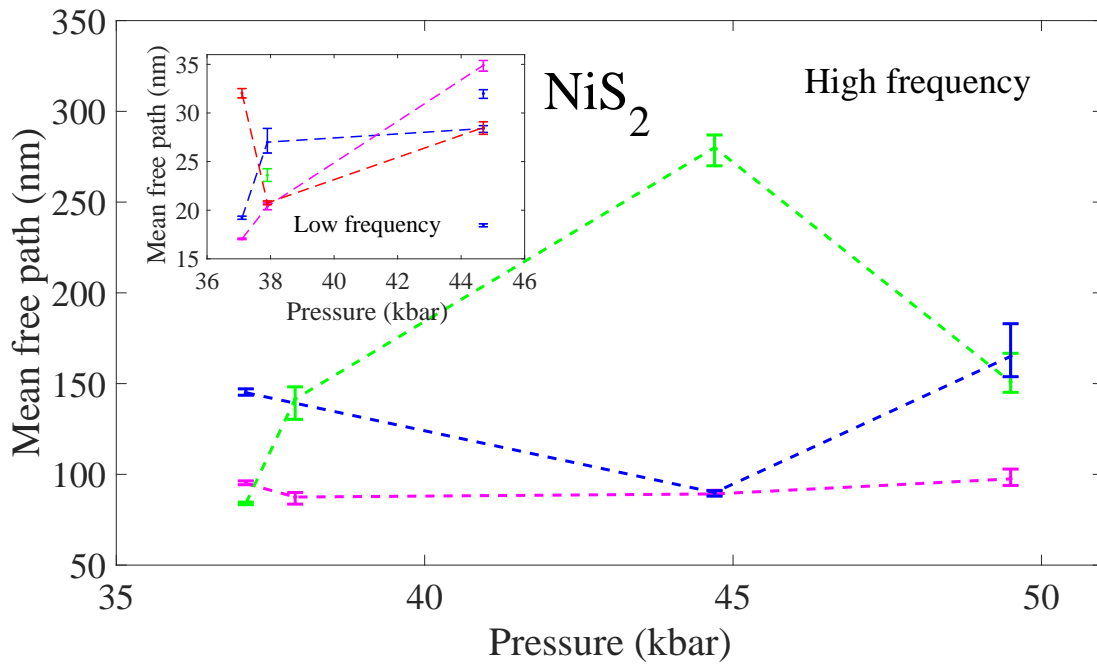
Figure 1.18: Mean free paths corresponding to the quantum oscillations presented above (Figures 1.16, 1.17). Colours are consistent between all three figures.
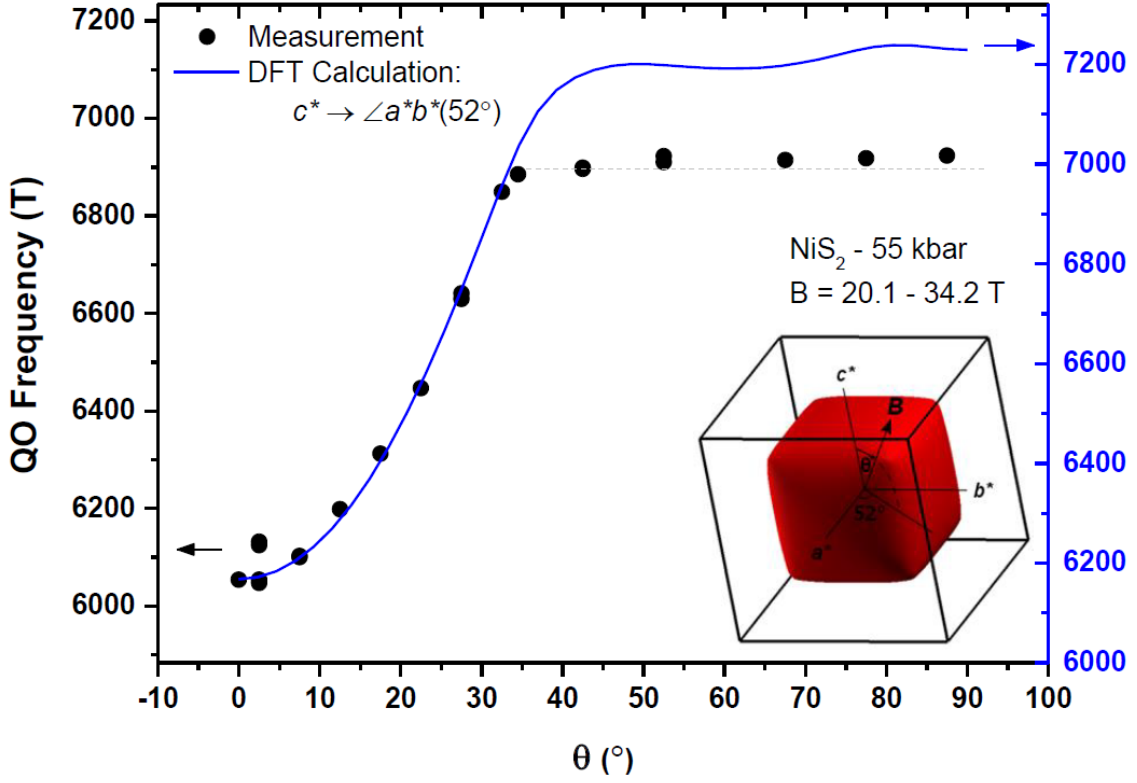
Figure 1.19: Frequency of quantum oscillations as a function of angle between the *c*-axis of the sample and the magnetic field direction [3]. The plane of rotation is at $52°$ angle with respect to the *ac* plane. Frequency predicted from the DFT results for the hole Fermi surface is plotted on the right vertical axis.

the predictions (Figure 1.19).

There is no solid explanation yet regarding the notion of three close-lying frequencies at most pressures. So far, the most likely explanation for it has been the breaking of the three-fold cubic symmetry by the antiferromagnetic order. This deforms the Fermi surfaces resulting in different extremal areas for different magnetic domains.

This thesis describes the experiments conducted throughout two recent trips to high magnetic field facilities. These measurements allowed to expand the studied pressure interval to 33–97 kbar, providing a clearer picture of the evolution of the Fermi surface when approaching the Mott MIT.

2 Theoretical concepts

2.1 Phase transitions and quantum critical phenomena

Under varying external conditions, such as temperature, pressure, magnetic field, etc., solid matter of fixed chemical composition can exist in different states, also known as phases, characterised by a set of physical properties. Transitions between different phases often result in a change of order, for example a change of lattice symmetry or an appearance of a well defined orientation within a system, as opposed to it being isotropic. In order to mathematically describe phase transitions a quantity called the order parameter was introduced, which is a function of external conditions and serves as a measure of the degree of ordering. For a given type of ordering (magnetic, structural, etc.) the order parameter is equal to zero in the disordered phase and is finite in the ordered phase. Transitions between these states are classified into two kinds: first order and second order phase transitions, characterised respectively by discontinuous or continuous change of the order parameter.

Given a number of possible phases, the favoured one can be determined by the minimisation of the relevant thermodynamic function, called the free energy [73]. For example, if the external conditions are defined by the temperature T and the pressure P, the order parameter η will take the value which minimises the Gibbs free energy $\Phi(P, T, \eta)$. In the phenomenological approach to describing phase transitions developed by Landau the free energy is expanded as Taylor series in the order parameter. Suppose that upon cooling down, a certain system undergoes a change from a disordered into an ordered phase at the critical temperature T_c. For such system, without any external fields applied, the Gibbs free energy can be expanded as a power series in η:

$$\Phi = \Phi_0 + A\eta^2 + B\eta^4 + \cdots . \tag{2.1}$$

No term linear in η is present because it would result in a non-zero value of the order parameter at all temperatures. The odd powers of η are also omitted because it is assumed that in this case there is no physical significance in the sign of the order parameter. Let us disregard the terms of higher order than η^4. Since this is a phenomenological theory, which terms are included in the expansion and at which point is the series truncated needs to be determined empirically for a phase transition in question. The requirement that $\eta = 0$ above T_c dictates that $A(P, T) > 0$ for $T > T_c$, and $A(P, T) < 0$ for $T < T_c$. Close to the transition temperature one can assume $A(P, T) = a(T - T_c)$, with $a > 0$. In this case:

$$\Phi = \Phi_0 + a\,(T - T_c)\,\eta^2 + B\eta^4, \tag{2.2}$$

and the minimisation of the Gibbs free energy results in the order parameter

$$\eta^2 = \frac{a}{2B}\,(T - T_c). \tag{2.3}$$

The behaviour of Φ and η as a function of temperature are illustrated in Figure 2.1, and it can be seen that such a model describes a second order phase transition. The
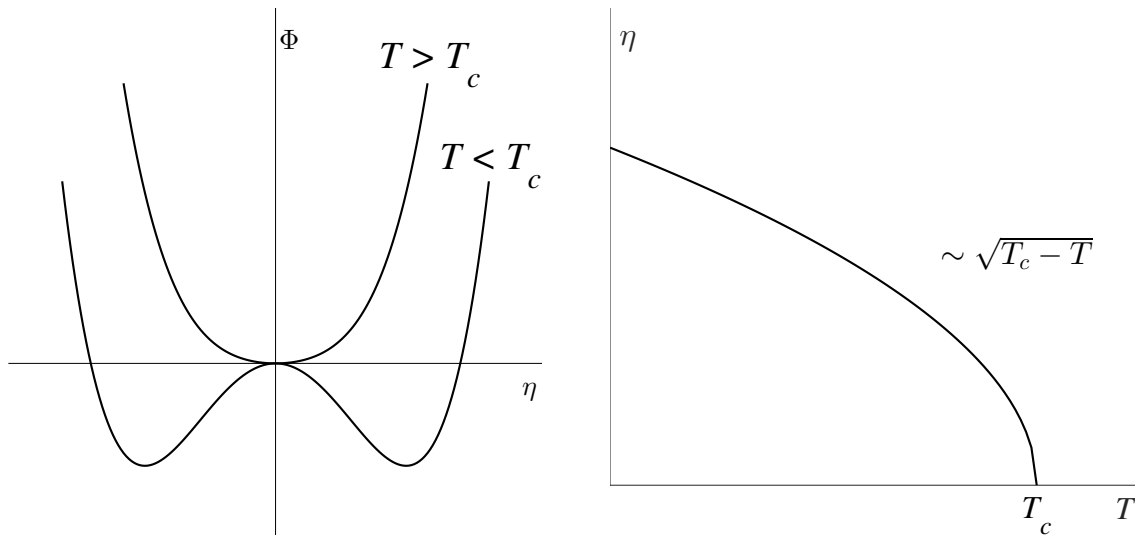
Figure 2.1: The Gibbs free energy as a function of the order parameter (left) and the order parameter as a function of temperature (right) for the case of the second order phase transition described in the text.

resultant expression for the free energy can be used for predicting how various related thermodynamic quantities behave at the phase transition and close to it.

The approach can be generalised to the case of a spatially varying order parameter, which is a function of position, $\eta = \eta(\mathbf{r})$. A slow spatial variation of the order parameter has an energy cost $\nabla \eta$ associated with it. Thus, invariants containing $\nabla \eta$ need to be included into the Gibbs free energy density. The lowest order term of this kind is proportional to $(\nabla \eta)^2$ and the simpliest expression for the total free energy is therefore given by the integral

$$\Phi = \int d^3 \mathbf{r} \left[A \eta^2 (\mathbf{r}) + B \eta^4 (\mathbf{r}) + C \left(\nabla \eta (\mathbf{r}) \right)^2 \right], \qquad (2.4)$$

which is known as the Ginzburg-Landau functional. The optimal $\eta(\mathbf{r})$ can once again be found by minimising Φ, which in this case requires solving differential equations. Positive C favours states with homogeneous order parameters. For $C < 0$ an extra term needs to be added, such as, for instance, $D \left(\nabla^2 \eta \right)^2$ with positive D. This typically results in $\eta(\mathbf{r})$ being periodic in space, describing, for example, the emergence of spin waves.

In case of a second order phase transition, when a system is close enough to the critical temperature a small disturbance of conditions (for example, due to a thermal noise) can locally push the system across the phase boundary. This results in spatial and temporal fluctuations of the order parameter. These fluctuations are crucial for a proper theoretical description of second order phase transitions and can substantially modify the behaviour of thermodynamic quantities predicted by the Landau model. Fluctuations of the order parameter at two different points are correlated:

$$\langle \Delta \eta (0) \, \Delta \eta (r) \rangle \sim \frac{T}{r} \exp \left(-\frac{r}{\zeta} \right), \qquad (2.5)$$
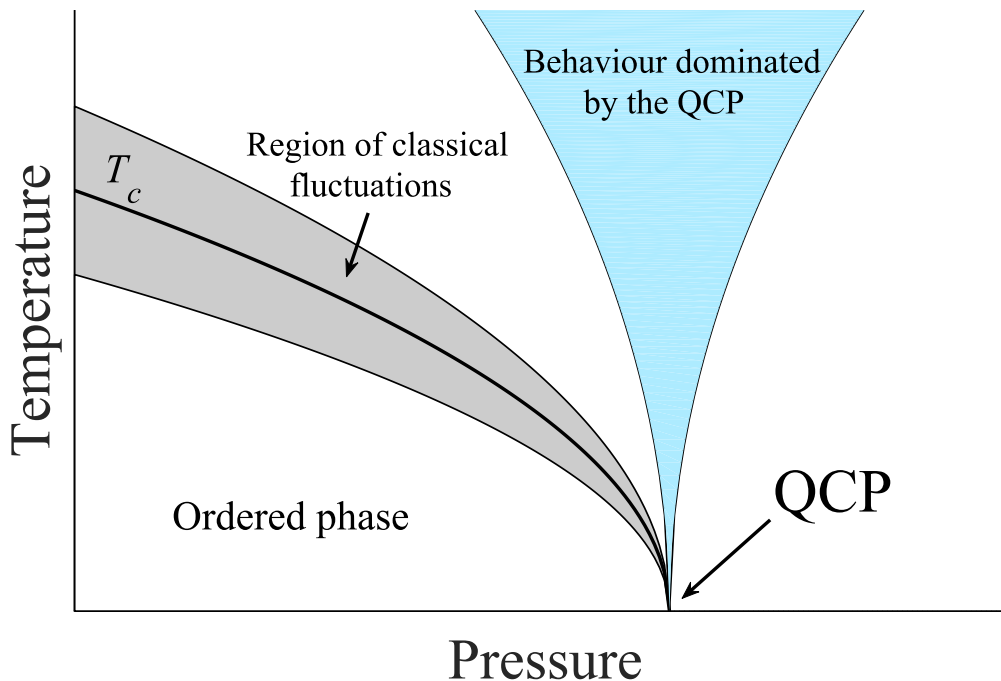
Figure 2.2: Phase diagram showing a quantum critical point (QCP) located at the pressure at which the critical temperature of a second order phase transition goes to zero.

where ζ is the correlation length and the angled brackets denote the cross correlation. The temperature dependence of ζ is given by

$$\zeta\left(T\right)=\sqrt{\frac{C}{a\left|T-T_c\right|}}. \qquad (2.6)$$

When the fluctuations are taken into account, a lot of quantities are predicted to have singularities at the T_c of type $\left|\left(T-T_c\right)/T_c\right|^{-\lambda}$, where λ is called the critical exponent. Close to the critical temperature the correlation length diverges and all microscopic details, which are important at short distances, become irrelevant. As a result, systems with different microscopic structures can have similar properties, characterised by a common set of critical exponents. Each such set applies to a distinct universality class. Systems with the same dimensionality and order type typically belong to the same universality class.

It may be possible to suppress the critical temperature of a second order phase transition by varying some parameter, such as pressure or magnetic field. A point in the phase diagram at which the T_c is reduced to zero is called the quantum critical point (QCP). This scenario is illustrated in Figure 2.2. Even at zero temperature the fluctuations exist in the vicinity of a phase transition, but they are now of quantum mechanical nature. Thermodynamic and transport properties of systems close to a QCP are strongly affected by these quantum fluctuations. In metallic systems proximity to the QCP can, for instance, cause non-Fermi liquid behaviour, divergence of effective charge carrier mass and emergence of superconductivity [74, 75].

2.2   Electrons in crystals

2.2.1   Basic theories of electronic structure

The most primitive theoretical description of electrons in a metal, the free electron model, assumes that valence electrons in a crystal behave like a gas of particles not interacting either with the lattice or with each other. According to the Schrödinger equation, wavefunctions of such electrons are plane waves :

$$\Psi\left(\mathbf{r}\right) = \frac{1}{\sqrt{V}}\exp\left(i\mathbf{k}\cdot\mathbf{r}\right), \tag{2.7}$$

where $\mathbf{r}$ is the position vector, V is the volume available for the electrons, $\mathbf{k}$ is the electron wavevector (related to the momentum via $\mathbf{p} = \hbar\mathbf{k}$) and i is the imaginary unit.

A free electron in such a state has energy $\varepsilon = \hbar^2 k^2/2m$, where m is the electron mass, $k = |\mathbf{k}|$ and $\hbar$ is the Planck constant. Taking the length of the lattice to be L in any of the principal directions and imposing periodic boundary conditions puts a constraint on $\mathbf{k}$ (and hence the allowed electronic states), allowing components for each principal direction (labeled with i) to take discrete values $k_i = 2\pi N/L$, where N is an integer. In the zero temperature limit electrons occupy the lowest available energy levels, but the Pauli exclusion principle limits the occupation of each one to two electrons of different spin. The states become filled up to a level by which all electrons are accommodated, called the Fermi energy

$$\varepsilon_F = \left(3\pi^2\right)^{2/3}\frac{\hbar^2}{2m}n^{2/3}, \tag{2.8}$$

where n is the volume density of the electrons. It is assumed that the number of states is sufficiently large so that their spectrum can be approximated as continuous. Given a relationship between $\mathbf{k}$ and ε (the dispersion relation), one can define a surface in the k-space (the momentum or reciprocal space) formed by all the wavevectors corresponding to the Fermi level. Such a surface is called the Fermi surface. In case of an isotropic three dimensional system of non-interacting electrons the Fermi surface is a sphere of the radius $k_F = \sqrt{2m\varepsilon_F/\hbar^2}$.

The states are not evenly spaced as a function of energy, therefore it is useful to calculate the number of energy levels per unit energy or the density of states, which for a three-dimensional system is

$$g\left(\varepsilon\right) = \frac{m}{\pi^2\hbar^2}\sqrt{\frac{2m\varepsilon}{\hbar^2}}. \tag{2.9}$$

At zero temperature every state below the Fermi level is occupied and every state above it is empty, but as temperature is increased electrons in the states close to the Fermi level can become become thermally excited to a state above it, leaving behind an empty state or a hole. The probability of some state with energy ε being occupied is given by the Fermi-Dirac distribution function (Figure 2.3):

$$f\left(\varepsilon\right) = \frac{1}{e^{(\varepsilon-\mu)/k_B T} + 1}, \tag{2.10}$$

where k_B is the Boltzmann constant, T is the temperature and $\mu\left(T\right)$ is the chemical
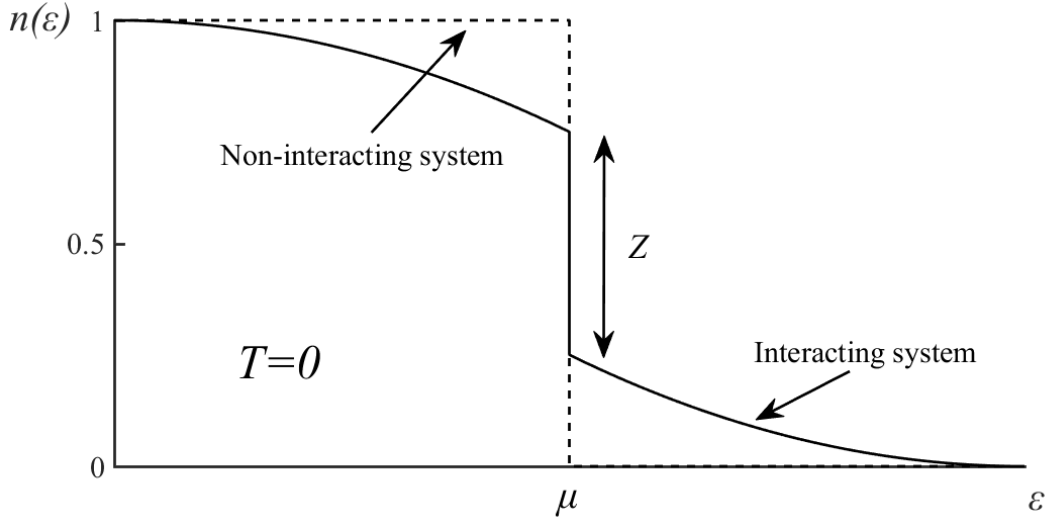
Figure 2.3: Probability of the occupation of states with energy ε at zero temperature for free and interacting electrons. Z is the wavefunction renormalisation constant also corresponding to the size of the discontinuity in the shown distribution at the chemical potential μ.

potential, equal to the Fermi energy at $T = 0$.

Using Equations 2.9 and 2.10 one can write down expressions for the total energy of the system of electrons per unit volume E and for the electron density n:

$$E = \int_0^\infty \varepsilon g\left(\varepsilon\right) f\left(\varepsilon\right) d\varepsilon, \tag{2.11}$$

$$n = \int_0^\infty g\left(\varepsilon\right) f\left(\varepsilon\right) d\varepsilon. \tag{2.12}$$

Using the second integral for finding the expression for $\mu(T)$ the temperature dependence of the energy can expressed as

$$E = E_0 + \frac{\pi^2}{6} k_B^2 T^2 g\left(\varepsilon_F\right), \tag{2.13}$$

where E_0 is a temperature independent part [76]. The expression can be used to calculate the heat capacity of free electrons per unit volume:

$$c_e = \left(\frac{\partial E}{\partial T}\right)_V = \left(\frac{\pi}{3}\right)^{2/3} \frac{m k_B^2 T}{\hbar^2} n^{1/3} = \gamma T, \tag{2.14}$$

with γ called the Sommerfeld coefficient. At the lowest temperature the heat capacity of a metallic system is dominated by the electronic contribution. Phononic heat capacity goes as T^3 and therefore becomes more influential at higher temperatures. The combined heat capacity per unit volume of electrons and phonons is therefore

$$c = \gamma T + \alpha T^3, \tag{2.15}$$

where α is a temperature independent parameter.

In order to quantify the charge transport properties of a free electron system one needs consider the effect of the external electric field $\mathbf{E}$. Electrons accelerate in the field, which can be thought of as a shift of their Fermi surface with time. Occasionally the motion of electrons is disturbed by inhomogeneities such as impurity atoms, defects of the lattice, phonons or other electrons. This leads to a scattering, i. e. a change of electron's momentum. On average the effect can be interpreted as resetting the velocity of the scattered electron to zero after a mean scattering time τ. This results in the time averaged current density, $\mathbf{J}$, in the material given by

$$\mathbf{J} = \frac{ne^2\tau}{m}\mathbf{E},\tag{2.16}$$

where e is the electron charge. This is a representation of the Ohm's law, from which the resistivity is

$$\rho = \frac{m}{ne^2\tau}.\tag{2.17}$$

The mean scattering time can be related to the average distance traveled by electrons between the scattering events. This distance l, called the mean free path, is often used for characterising the quality of crystals and is given by

$$l = v_F\tau = \frac{\hbar k_F\tau}{m}\tag{2.18}$$

where $v_F = \hbar k_F/m$ is the Fermi velocity.

It is relatively easy to modify the free electron model in order to account for interactions of electrons with ions of a crystal lattice. To do that one has to assume that the lattice of ions is fixed in its equilibrium configuration and is not affected by the electrons (this is known as the Bohr-Oppenheimer approximation). The Bloch's theorem states that electrons in a periodic potential produced by the ions have wavefunctions, called the Bloch waves, of the form:

$$\Psi(\mathbf{r}) = \exp(i\mathbf{k}\cdot\mathbf{r})\,u(\mathbf{r}),\tag{2.19}$$

where $u(\mathbf{r})$ is a periodic function of position with the same periodicity as the lattice. Instead of a single continuous density of electronic states the model predicts the emergence of separate energy bands. There are energy intervals between the bands with no states available called the band gaps. For every two valence electrons per atom a band becomes completely occupied. Therefore, according to this model, crystals with odd number of electrons have a partially filled energy band. Since there are unoccupied states located just above the Fermi level, electrons are not localised in their states below it and the crystal is a metal. For an even number of electrons per atom the highest occupied band is full and the lowest empty state is separated from the highest occupied state by a band gap. Electrons therefore remain in their states, resulting in an insulator (or a semiconductor for a small enough band gap). With the lattice potential present, electrons react to external electric fields in a manner, in which free electrons would behave if they had a different mass. Near the band minimum (or maximum) it is possible to approximate the dispersion

relation $\varepsilon(\mathbf{k})$ with a parabola and based on its curvature define the effective band mass of electrons (or holes) $m_i = \hbar^2 / (\partial^2 \varepsilon / \partial k_i^2)$, where index i stands for the direction of electrons motion.

For a good theoretical description of many real systems it is required to consider electron-electron interactions. This task it is non-trivial, as each electron interacts with a large number of other ones. One approximation which deals with this problem is the Fermi liquid theory developed by Landau. The theory is based on the idea of the adiabatic continuity between the corresponding systems of free and interacting electrons. This means that when the interaction between the electrons is gradually switched on, for every quantum state of the non-interacting electrons system there exists a corresponding state of the system of the interacting electrons. These latter states are called the quasiparticle states. The quasiparticles behave similarly to free electrons: they have the same spin and charge as electron, can be characterised by momentum $\mathbf{p} = \hbar\mathbf{k}$ and energy $\varepsilon(\mathbf{k})$ and form a Fermi surface of the same volume in the k-space as a corresponding free electron system.

This model results in many physical quantities, such as heat capacity, showing behaviour similar to that of a free electron system. The difference is manifested as the effective electron mass renormalisation: the quasiparticles behave like electrons with a different mass $m^* = m_0/Z$, where m_0 is the effective band mass of electrons (related to the curvature of $\varepsilon(\mathbf{k})$ at the band minimum) and Z is the wavefunction renormalisation constant ($0 < Z < 1$). The energy distribution of the quasiparticles is modified compared to Equation 2.10. The discontinuity at the chemical potential at zero temperature still exists (and hence the Fermi surface does too), but the height of the jump is reduced to Z (Figure 2.3).

In order to see the implications of this model on the charge transport properties, one can consider the scattering rate of the quasiparticles very close to the Fermi level. Suppose there exists an excitation slightly above the Fermi level with momentum $\mathbf{p}_1$ and energy ε_1. This quasiparticle can scatter due to an interaction with another quasiparticle with $|\mathbf{p}_2| < p_F$, i.e. below the Fermi level. The result of such interaction is two particles above the Fermi level with momenta $\mathbf{p}_3$ and $\mathbf{p}_4$. Conservation of momentum dictates that $\mathbf{p}_1 + \mathbf{p}_2 = \mathbf{p}_3 + \mathbf{p}_4$, and therefore the quantity $(|\mathbf{p}_\alpha| - p_F)$ for $\alpha = 2, 3, 4$ cannot exceed $(|\mathbf{p}_1| - p_F)$. The equivalent relationship holds for the energies. The scattering rate can be estimated with Fermi's "golden rule":

$$\tau^{-1} \sim \int \delta(\varepsilon_1 + \varepsilon_2 - \varepsilon_3 - \varepsilon_4)\, d^3\mathbf{p}_2 d^3\mathbf{p}_3, \tag{2.20}$$

where the integration is over the momenta $\mathbf{p}_2$ and $\mathbf{p}_3$ due to $\mathbf{p}_1$ being fixed and $\mathbf{p}_4$ being constrained by the momentum conservation. The energy extent of the available states for particles 2 and 3 is $(\varepsilon_1 - \varepsilon_F)$ in both cases, making the scattering time roughly proportional to $(\varepsilon_1 - \varepsilon_F)^2$. This implies that quasiparticle excitations become very stable close to the Fermi surface, where $(\varepsilon - \varepsilon_F)$ approaches zero. At a finite temperature the magnitude of this interval is approximately $k_B T$. Combined with Equation 2.17 this leads to

$$\rho \sim (\varepsilon - \varepsilon_F)^2 \sim T^2. \tag{2.21}$$

Keeping in mind that the electron-phonon scattering is insignificant at low temperatures, a lot of metals have the low temperature resistivity of the form

$$\rho\left(T\right) = \rho_0 + AT^2, \tag{2.22}$$

where ρ_0 is the residual resistance, a temperature independent part due to impurity and defect scattering. The A coefficient is a temperature independent parameter, which is often proportional to γ^2 within the same class of compounds (the proportionality constant is often referred to as the Kadowaki-Woods ratio) [77, 78]. The A coefficient can therefore be interpreted as a measure of strength of the electron-electron interactions. Within the Fermi liquid model the residual resistance can be related to the mean free path, l_0, of the quasiparticles due to the scattering from defects and impurities:

$$\frac{1}{\rho_0} = \frac{e^2 S_F l_0}{12\pi^3 \hbar}, \tag{2.23}$$

where S_F is the Fermi surface area [79]. In case of multiple Fermi surfaces the right-hand side becomes a sum over them with each term having different S_F and l_0.

The Fermi liquid state described above is not the only possible state of a metal without a formation of some long range order. One example of that is a non-Fermi liquid behaviour close to a quantum critical point (QCP). Such states are typically observed in the blue region of the phase diagram in Figure 2.2 and are characterised by an unconventional temperature scaling of thermodynamic and transport properties. For example, the electronic heat capacity of non-Fermi liquid systems often exhibits a non-linear temperature dependence, and their electrical resistivity has a temperature exponent different from 2. These deviations are generally explained in terms of an interaction of electrons with collective excitations associated with the nearby order. The value of the temperature exponent therefore depends on the particular order in question. For example, itinerant ferromagnet $ZrZn_2$ has $T^{5/3}$ dependence of resistivity [80], and for antiferromagnetic $CeCu_2Si_2$ it goes as $T^{3/2}$ [81].

2.2.2 Density functional theory

Density functional theory (DFT) is a numerical method of modelling the ground state electronic structure of many-electron systems. This technique is widely used in condensed matter physics for predicting band structures and Fermi surfaces of crystals. The main principles behind DFT and its derivation are outlined below.

The total energy of a many-electron system can be thought of as a sum of kinetic energy of the electrons, potential energy of their interaction with the lattice of ions and potential energy of electron-electron interactions. The problem can therefore be formulated as the Hamiltonian

$$\hat{H} = \sum_{i=1}^{N} \frac{\hat{p}_i^2}{2m} - \sum_{i=1}^{N}\sum_{k=1}^{M} \frac{Ze^2}{4\pi\varepsilon_0 \left|\mathbf{r}_i - \mathbf{R}_k\right|} + \frac{1}{2}\sum_{i\neq j}^{N} \frac{e^2}{4\pi\varepsilon_0 \left|\mathbf{r}_i - \mathbf{r}_j\right|} = \hat{T} + \hat{V}_{Ne} + \hat{V}_{ee}. \tag{2.24}$$

In the expression above N and M are respectively the total numbers of electrons and ions, Z is the ionic charge in units of $|e|$, $\mathbf{r}_i$ and $\mathbf{R}_k$ respectively stand for position vectors of the i-th electron and the k-th ion, $\hat{p}_i$ is the i-th electron total momentum operator and ε_0 is the dielectric permeability of vacuum. On the right-hand side of the expression the three terms of the Hamiltonian are respectively denoted as operators corresponding to the kinetic energy of the electrons ($\hat{T}$), the potential energy of electron-ion interactions ($\hat{V}_{Ne}$) and the potential energy of electron-electron interactions ($\hat{V}_{ee}$). When DFT is used for describing the electronic structure of crystals, the ion-ion interaction energy is often neglected, and the experimentally determined lattice structure is used to define the ionic potential. As a consequence of the Bohr-Oppenheimer approximation, the ion-ion interaction potential energy is totally decoupled from other contributions to the total energy.

In DFT, as the name suggests, the central quantity is the electron (or charge) probability density $n(\mathbf{r})$. Integrating $n(\mathbf{r})$ over all space should result in the total number of electrons N. DFT is founded on two theorems called the Hohenberg-Kohn theorems [82]. The first Hohenberg-Kohn theorem states that for an N-electron system the external potential $\hat{V}_{Ne}(\mathbf{r})$ is a unique functional of the ground state electron density $n(\mathbf{r})$. Given that $\hat{V}_{Ne}(\mathbf{r})$ determines the Hamiltonian, it can be concluded that all the ground state properties of an N-body system are unique functionals of $n(\mathbf{r})$. The total energy E as well as its constituents T (kinetic energy), E_{Ne} (electron-ion interaction potential energy) and E_{ee} (electron-electron interaction potential energy) can therefore be treated as unique functionals of the electron density. Let us write the total energy as

$$
\begin{aligned}
E[n] = T[n] + E_{Ne}[n] + E_{ee}[n] &= \int d^3\mathbf{r}\, n(\mathbf{r})\,\hat{V}_{Ne}(\mathbf{r}) + T[n] + E_{ee}[n] \\
&= \int d^3\mathbf{r}\, n(\mathbf{r})\,\hat{V}_{Ne}(\mathbf{r}) + F_{HK}[n],
\end{aligned}
\tag{2.25}
$$

where another functional $F_{HK}[n]$, equal to the sum of $T[n]$ and $E_{ee}[n]$, has been defined. The second Hohenberg-Kohn theorem states that for a certain system $F_{HK}[n]$ assumes the lowest value if and only if $n(\mathbf{r})$ is the ground state electron density.

The exact form of $F_{HK}[n]$ is unknown, which is the challenge that DFT aims to overcome. To start with, $E_{ee}[n]$ can be written as

$$
E_{ee}[n] = \frac{1}{2} \int \int d^3\mathbf{r}\, d^3\mathbf{r}'\, \frac{e^2}{4\pi\varepsilon_0} \frac{n(\mathbf{r})\,n(\mathbf{r}')}{|\mathbf{r}-\mathbf{r}'|} + E_{NC}[n] = J[n] + E_{NC}[n],
\tag{2.26}
$$

where the functional was separated into the Coulomb interaction energy $J[n]$ and some unknown non-classical contribution $E_{NC}[n]$. A good approach to approximating the kinetic energy is calculating one for a reference system of non-interacting electrons having the same electron density:

$$
T_S = 2 \sum_{i=1}^{N/2} \langle\psi_i| \frac{-\hbar^2}{2m} \overrightarrow{\nabla}^2 |\psi_i\rangle,
\tag{2.27}
$$

where $\psi_i(\mathbf{r})$ are the eigenstates of the non-interacting system such that

$$2 \sum_{i=1}^{N/2} |\psi_i(\mathbf{r})|^2 = n(\mathbf{r}). \tag{2.28}$$

Multiplication by 2 and summation over $N/2$ terms takes care of the spin degeneracy. One can now rewrite $F_{HK}[n]$ as

$$F_{HK}[n] = T_S[n] + J[n] + E_{XC}[n], \tag{2.29}$$

where the term $E_{XC}[n]$, called the exchange-correlation energy functional, is equal to the sum of $(T[n] - T_S[n])$ and $E_{NC}[n]$.

The functional $E_{XC}[n]$ effectively encapsulates all contributions to the total energy which cannot be expressed in closed form. One therefore has to use an approximate form for the exchange-correlation functional, and there exist various established approaches to this. For example, within a class of approximations collectively known as the local density approximation (LDA) the exchange correlation functional is assumed to depend on the electron density at each point in space. The generalised gradient approximation (GGA) is more advanced, since it also incorporates the gradient of $n(\mathbf{r})$ into $E_{XC}[n]$. Reliability of DFT results strongly depends on choosing the right approximation.

Assuming that some approximate form of $E_{XC}[n]$ was chosen, one can employ the calculus of variations in order to find the optimal set of eigenstates $\{\psi_i\}$ which minimise the total energy subject to the orthonormality constraint

$$\int d^3\mathbf{r}\, \psi_i^\dagger \psi_j = \delta_{i,j}, \tag{2.30}$$

where $\delta_{i,j}$ is the Kronecker delta. Implementing such a constraint requires $(N/2)^2$ Lagrange multipliers $\varepsilon_{i,j}$, but given a set of basis states $\{\psi_i\}$ it is possible to find a new set such that the Lagrange multipliers are diagonal in i and j. Therefore, without any loss of generality, the functional which needs to be minimised can be written as

$$L[\{\psi_i\}] = E[\{\psi_i\}] - 2 \sum_{i=1}^{N/2} \varepsilon_i \left(\int d^3\mathbf{r}\, \psi_i^\dagger \psi_i - 1 \right). \tag{2.31}$$

Imposing $\delta L[\{\psi_i\}] = 0$ results in a set of so called Kohn-Sham equations [83]:

$$\left(-\frac{\hbar^2}{2m} \overrightarrow{\nabla}^2 + \frac{\delta E_{Ne}}{\delta n} + \frac{\delta J}{\delta n} + \frac{\delta E_{XC}}{\delta n} \right) \psi_i = \varepsilon_i \psi_i. \tag{2.32}$$

It can be noticed that Kohn-Sham equations have the same form as a single particle Schrödinger equation, but given that $\delta J/\delta n$ and $\delta E_{XC}/\delta n$ both depend on the electron density, these equations have to be solved through self-consistent iterations.

As illustrated above, the main idea of DFT is converting from a many-particle problem into a single particle one. By constraining $\{\psi_i\}$ to be a set of Bloch waves of variable wavenumber k, it is possible to calculate band dispersions and predict Fermi

surfaces of crystals. Even though DFT results are often in good general agreement with experimentally determined band structure (for example, by ARPES), it must be noted, however, that from a theoretical standpoint the eigenvalues of the Kohn-Sham equations do not have a direct physical interpretation. Another important point is that DFT is intended for predicting the ground state properties. Due to these reasons, when calculating quasiparticle energies and band gaps using DFT, one should always expect some systematic error. Using DFT to predict properties of strongly correlated systems is also known to be quite problematic.

2.2.3 Dynamical mean-field theory

The dynamical mean-field theory (DMFT) is another model used for describing electronic structure of crystals [47]. Contrary to DFT, DMFT manages to capture effects of strong electronic correlations. In particular, DMFT can be successfully applied to the Hubbard model (Equation 1.1) in order to describe the Mott metal-insulator transition upon increasing strength of electronic correlations.

Rather than trying to deal with a many-body problem on a lattice (which is in general not solvable), DMFT maps it to a many-body local problem, i.e. for just a single site, which interacts with the surroundings trough a time dependent mean field (this is also known as an impurity model). DMFT is usually used to predict the Green's function for electrons on the lattice (its imaginary part is directly related to the spectral function). A self-consistency condition requires this Green's function to be equal to the impurity's Green's function. The interaction with the mean-field is characterised by a hybridisation function, which dictates how likely the state of the impurity is to change between different configurations (0, 1 or 2 electrons on the site) in a given time interval. The only approximation that DMFT uses is equating lattice and impurity self-energies (this becomes exact in the limit of infinite number of spatial dimensions). Through iterative calculations the Green's function converges to its resultant form.

Explaining DMFT using basic rules of quantum mechanics would be rather involved, as a number of more advanced theoretical formalisms would need to be introduced first. What is of importance in context of this dissertation, is that DMFT, when applied to a bandwidth controlled Mott MIT, reproduces the main results of the Brinkman-Rice model, namely the existence of a large Fermi surface in the metallic phase all the way until the phase boundary, as well as the divergence of the associated effective quasiparticle mass.

2.3 Superconductivity

2.3.1 Ginzburg-Landau theory

One of the alternatives to the Fermi liquid state for metals at low temperatures is a superconducting state, characterised primarily by the complete absence of electrical resistivity. A transition between normal and superconducting states can be treated phenomenologically according to the Landau model described earlier in this chapter. Such description is known as the Ginzburg-Landau (GL) theory of superconductivity

[84]. The superconducting state is a more ordered state in which electrons form a superfluid. The transition has an associated order parameter $\psi(\mathbf{r})$ called the macroscopic wavefunction. It is a complex quantity which can be expressed as $\sqrt{n_s}\exp(i\theta)$, where n_s is the density of superfluid electrons and θ is the complex phase. ψ is therefore equal to zero in the normal state, as required. The minimisation of the free energy functional results in the two GL equations:

$$\frac{1}{2m}\left(-i\hbar\nabla - \frac{q}{c}\mathbf{A}\right)^2\psi + A\psi + 2B\left|\psi\right|^2\psi = 0, \tag{2.33}$$

$$\mathbf{J}_s = \frac{iq\hbar}{2m}(\psi^*\nabla\psi - \psi\nabla\psi^*) - \frac{q^2}{m}\mathbf{A}\psi^*\psi = -\frac{qn_s}{m}(\hbar\nabla\theta + q\mathbf{A}), \tag{2.34}$$

where $\mathbf{A}$ is the magnetic field vector potential, $\mathbf{J}_{\mathrm{s}}$ is the supercurrent density and the asterisk symbol denotes a complex conjugate. q and m are the relevant charge magnitude and mass which were experimentally found to be $2e$ and $2m_e$ respectively.

For $\mathbf{A} = \mathbf{0}$ the first GL equation can be rewritten as

$$\xi^2\nabla^2\psi + \psi - \frac{2B}{|A|}\left|\psi\right|^2\psi = 0, \tag{2.35}$$

where $A = -\left|A\right|$ was assumed. A quantity called the coherence length was defined as

$$\xi = \sqrt{\frac{\hbar^2}{2m\left|A\right|}}. \tag{2.36}$$

The coherence length is a temperature dependent parameter, which diverges at the T_c. There is an energy penalty associated with a spatial variation of $\psi(\mathbf{r})$, and ξ is the lengthscale over which the superfluid density remains roughly constant. The zero temperature limit is strongly material dependent and can range over several orders of magnitude.

Assuming the fixed value of ψ and taking the curl of Equation 2.34 allows one to model the response of a superconductor to an external magnetic field. This results in the London equation and another characteristic lengthscale λ called the London penetration depth:

$$\nabla^2\mathbf{B} = \frac{\mathbf{B}}{\lambda^2}, \tag{2.37}$$

$$\lambda = \sqrt{\frac{m}{\mu_0 n_s q^2}}. \tag{2.38}$$

Physically this means that inside a superconductor the magnetic field gradually decays over a characteristic length λ, which is usually of the order of 100 nm. Deeper inside the bulk the field is effectively zero. This expulsion of magnetic flux is known as the Meissner effect.

Increasing the magnetic field strength can lead to two scenarios. The superconductor can keep expelling the flux until the superconductivity is suddenly destroyed at the critical field B_c. This is known as type I superconductivity, which is common for elemental superconductors. Type II superconductivity is characterised by the formation of vortices
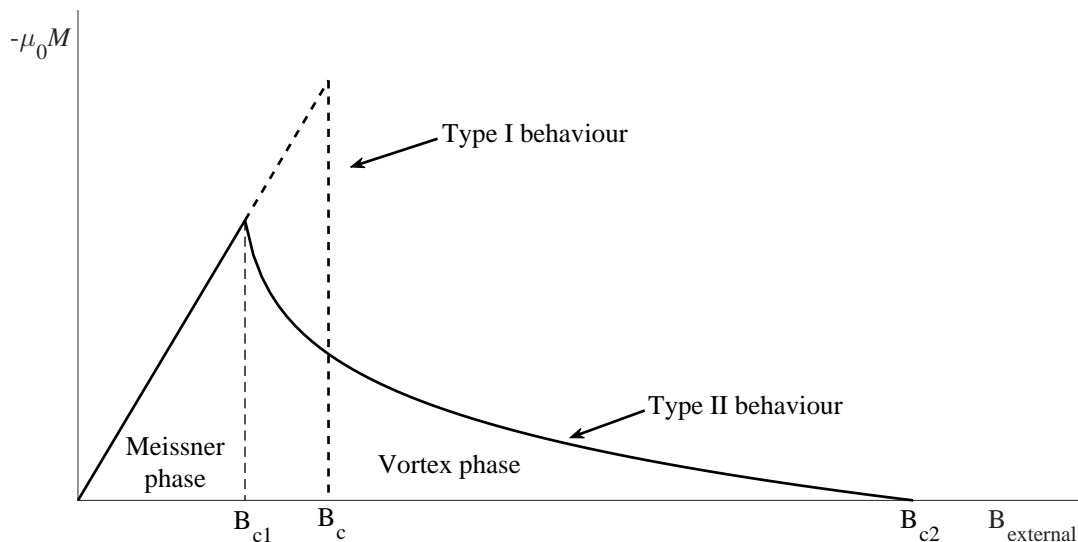
Figure 2.4: Magnetisation of type I and type II superconductors as a function of external magnetic field.

– cylindrical regions of normal phase aligned with the field direction and surrounded by tubular loops of the supercurrent. In an ordered crystal these vortices form a triangular lattice. The magnetic field strength B_{c1} at which this transition occurs is called the lower critical field and is given by

$$B_{c1} = \frac{\phi_0}{4\pi\lambda^2} \ln\left(\frac{\lambda}{\xi}\right),$$ (2.39)

where ϕ_0 is the magnetic flux quantum. Further increase of the magnetic field strength results in expansion of the normal state cores of the vortices until they overlap with each other and the superconducting phase vanishes completely at the upper critical field

$$B_{c2} = \frac{\phi_0}{2\pi\xi^2}.$$ (2.40)

Such mechanism is known as the orbital limiting effect.

In order to describe the temperature dependence of the orbital limited upper critical field the Werthamer-Helfand-Hohenberg (WHH) model is often used [85]. The zero temperature limit of the orbital limited upper critical field B_{c2} can be calculated from the critical temperature and the temperature derivative of the critical field at T_c:

$$B_{c2}(0) = \beta T_c \left|dB_{c2}/dT\right|_{T_c},$$ (2.41)

where β is a numerical factor which depends on the purity of a crystal, which can be quantified by the relative magnitudes of the coherence length, ξ, and the mean free path, l. In the clean limit ($\xi \ll l$) $\beta = 0.73$, while in the dirty limit ($\xi \gg l$) $\beta = 0.69$.

The effect of magnetic field on different types of superconductors is shown in Figure 2.4. A common test for superconductivity is measuring magnetisation at fields low enough for the sample to be in a Meissner phase. A superconductor under such conditions is expected to be a perfect diamagnet and have the magnetic susceptibility of -1.

35

2.3.2 BCS theory

The first microscopic description of superconductivity was provided by the BCS theory (named after its authors: Bardeen, Cooper and Schrieffer [9]). The mechanism responsible for the phenomenon is the formation of electron pairs, also known as the Cooper pairs. The attractive interaction is mediated by phonons, but can nonetheless be illustrated from a classical point of view. As electron moves through a crystal it pulls the neighbouring lattice ions towards it. The ions are much heavier than the electron and move much slower. As a result, the electron leaves a trail of positively charged region due to ions which have not yet relaxed from the disturbance produced by the electron. Another electron is attracted to this positively charged region. The energy extent of states of electrons which can interact in this manner is limited to $\hbar \omega_D$ (ω_D is the Debye frequency) and the attraction is the strongest for pairs of electrons with opposite momenta $\mathbf{k}$ and $-\mathbf{k}$. Particle exchange symmetry of the resultant two electron wavefunction also requires them to have opposite spins.

It can be shown that given a Fermi liquid state such attractive interaction, however weak, will lead to the formation of stable Cooper pairs. The energy change in such process is

$$E = -\hbar \omega_D \exp\left(-1/\lambda\right), \tag{2.42}$$

where $\lambda = g\left(\varepsilon_F\right) V$ with $g\left(\varepsilon_F\right)$ being the Fermi liquid quasiparticle density of states at the Fermi level and V being the magnitude of potential energy of the attraction. The ground state is then formed by these Cooper pairs. Given the quasiparticle energy spectrum ε_k, energy of the excited states is given by:

$$E_k = \sqrt{\left(\varepsilon_k - \mu\right)^2 + |\Delta|^2}, \tag{2.43}$$

where μ is the chemical potential and Δ is a complex function of temperature and momentum direction called the superconducting gap function. The expression above means that there exists an energy gap between the ground state and the band of excited states. Large enough gap prevents spontaneous scattering from the ground state into these excited states. This is manifested as the absence of electrical resistivity. It is often assumed that $|\Delta|$ is much smaller than the Fermi energy, and this assumption is known as the "weak coupling" approximation. Increasing temperature causes the magnitude of the gap function to go down and vanish completely at the critical temperature, T_c, which the theory predicts to be approximately given by

$$T_c k_B = 1.14 \hbar \omega_D \exp\left(-1/\lambda\right). \tag{2.44}$$

Existence of the gap modifies the the form of the electronic heat capacity (Figure 2.5). Below T_c quasiparticle excitations happen with probability roughly given by the Boltzmann factor $\exp\left(-\Delta/k_B T\right)$, which largely determines the shape of the heat capacity curve. The superconducting state is a more ordered state and therefore has lower entropy. There is a discontinuous change in the slope of the entropy at T_c. This results in a jump
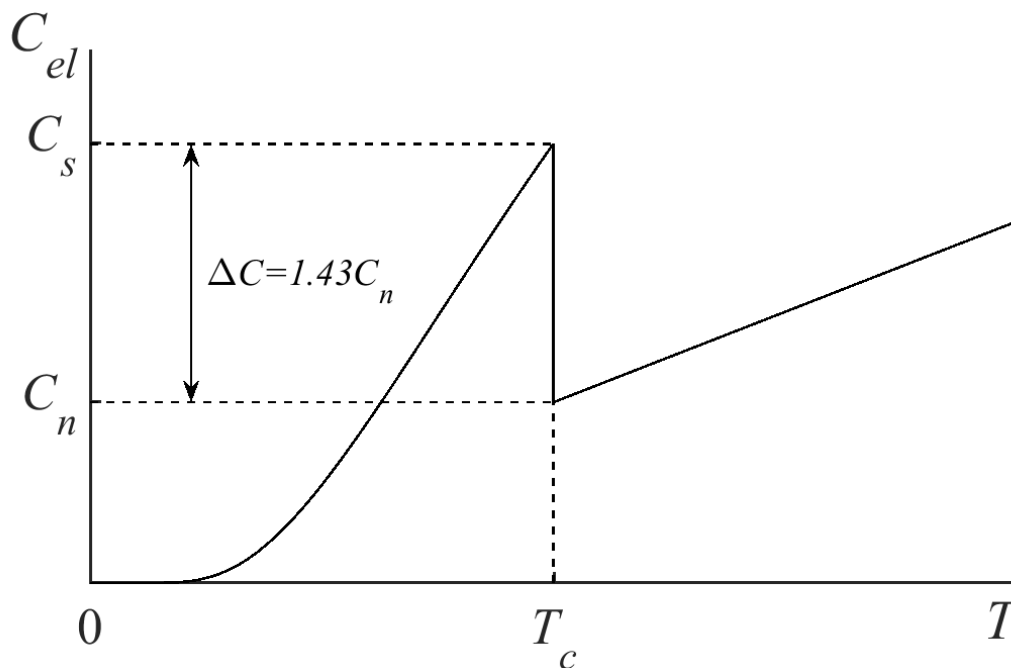
Figure 2.5: Electronic heat capacity of a superconducting metal as a function of temperature. Upon cooling the heat capacity jumps at T_c from the normal state value C_n to a new one in the superconducting state C_s. Size of the jump, ΔC, is universal for the weak coupling limit of BCS theory of superconductivity.

in the heat capacity upon cooling by a factor of 1.43 in the weak coupling limit.

The fact that a Cooper pair contains particles of the opposite spins leads to another mechanism through which magnetic field can destroy superconductivity. In an external magnetic field, H, normal state electrons can become spin polarised, which is an alternative way of reducing the energy of the system. When the energy decrease due to the spin polarisation $\frac{1}{2}\mu_0\chi_P H^2$ (χ_P - Pauli magnetic susceptibility) becomes greater than the energy decrease due to the Cooper pair condensation $\frac{1}{2}g\left(\varepsilon_F\right)|\Delta|^2$ the superconductivity gets suppressed. This is known as the Pauli limiting effect.

2.3.3 Unconventional superconductivity

Superconductors described by the BCS theory (and its extensions) are classified as conventional superconductors. There are also superconducting materials for which this model does not work – unconventional superconductors. A number of families of unconventional superconductors has been identified to date, such as cuprate, iron based and heavy fermion superconductors. While there does not yet exist a complete microscopic model describing any of the non-BCS superconductors, experimental evidence suggests that there are both similarities and differences between the two.

The phenomenon of the Cooper pair formation and condensation is still the underlying mechanism in the unconventional superconductivity, but the attraction between the quasiparticles is widely believed to be caused by magnetic interactions, rather than the electron-phonon coupling [86]. Additionally, in BCS model Cooper pairs have zero orbital angular momentum quantum number ($l = 0$), which leads to the gap

function Δ being isotropic in the *k*-space (the picture known as the s-wave gap), whereas for non-BCS systems $l > 0$ and Δ can vary with $\mathbf{k}$ direction (in both phase and magnitude) and can develop nodes – points or lines at which the gap function is zero. Excitations near these nodes modify some physical properties of the superconducting phase, in particular the temperature dependence of the heat capacity. For example, in the case of line nodes electronic heat capacity goes as T^2 for $T \ll T_c$, while point nodes lead to a T^3 dependence [87].

2.4 Theory of muon spin relaxation spectroscopy

The idea behind the muon spin relaxation spectroscopy, commonly abbreviated as μSR, is to use the intrinsic magnetic moment (spin) of muon (or antimuon) as a probe of local magnetic field inside a crystal. A muon (μ^-) is an elementary particle classified as lepton, the same family of particles which an electron belongs to. A muon has the same charge and spin as an electron, but is about 207 times heavier and has a magnetic moment of $8.891\mu_N$ (μ_N – nuclear magneton). It is an unstable particle with an average lifetime of 2.197 µs. In μSR facilities, antimuons (μ^+) are primarily used, however, it is common to refer to them as muons. Their production typically starts with a beam of fast protons hitting a carbon target. Collisions of protons with nucleons in carbon can produce π^+ mesons (pions) according to the reactions:

$$p^+ + p^+ \rightarrow \pi^+ + p^+ + p^+, \tag{2.45}$$

$$p^+ + n \rightarrow \pi^+ + p^+ + n, \tag{2.46}$$

where p^+ and n denote proton and neutron respectively. Pions are unstable (26 ns lifetime) and decay into antimuons and muon neutrinos:

$$\pi^+ \rightarrow \mu^+ + \nu_\mu. \tag{2.47}$$

As a consequence of the symmetry under parity violation in the weak interaction [88] the spins of produced antimuons almost always point in the direction opposite to their momentum. These spin polarised muons are used for the experiment.

Various configurations of μSR experiments exist, but only the transverse field (TF) μSR, typically used for studying the vortex phase of type II superconductors, is described here. More information about the technique can be found in the book by Yaouanc and de Réotier [89]. In TF μSR an external magnetic field is applied to the sample in direction perpendicular to the spins of incoming antimuons. Suppose the field points in z direction and the antimuons travel in the positive x direction, so that their spins point in the negative x direction. An antiparticle arriving at the sample penetrates into the bulk and settles at an interstitial site of the lattice. The local magnetic field at the antimuon site $\mathbf{B}_{loc}$ causes a precession of its spin. The external field is typically high enough to dominate the local field. Therefore, assuming $\mathbf{B}_{loc}$ points in the z direction, antimuon spins precess in the xy plane with the angular frequency $\gamma_\mu |\mathbf{B}_{loc}|$, where γ_μ is the gyromagnetic ratio

of muon ($2\pi\times135.539\times10^6$ s^{-1} T^{-1}). Eventually the antimuon decays into a positron e^+, an electron neutrino ν_e and a muon antineutrino $\bar{\nu}_\mu$:

$$\mu^+ \rightarrow e^+ + \nu_e + \bar{\nu}_\mu. \tag{2.48}$$

Positrons produced in this decay are emitted predominantly in the direction of muon spin. The angular distribution depends on the positron energy E and is given by

$$p\left(\theta, E\right) = 1 + a\left(E\right)\cos\theta, \tag{2.49}$$

where θ is the angle between the antimuon spin and the positron emission direction and $a\left(E\right)$ is an energy dependent parameter which on average is equal to $1/3$.

The emitted positrons are registered with a set of detectors, typically divided into backwards and forwards detectors located respectively in front of and behind the sample (the front of the sample is hit by the beam). Based on the difference between their instantaneous count rates is possible to infer the average direction of antimuon spin at a certain time t. The number of particles detected in a small time interval as a function of time in, for instance, forward direction goes as

$$N_f\left(t\right) \propto \exp\left(-t/\tau_\mu\right)\left(1 + a_0 P_x\left(t\right)\right), \tag{2.50}$$

where τ_μ is the average muon lifetime. The term $a_0 P_x\left(t\right)$ is called the asymmetry function and consists of the initial asymmetry a_0 – an instrument specific parameter, and the normalised spin polarisation function $P_x\left(t\right)$ (for example, $P_x = 0$ for no net polarisation and $P_x = 1$ for complete polarisation in the positive x direction). For a pair of forward and backward detectors giving corresponding particle counts N_f and N_b, the asymmetry function can be extracted as

$$a_0 P_x\left(t\right) = \frac{N_f - \alpha N_b}{N_f + \alpha N_b}, \tag{2.51}$$

where α is an instrument specific factor accounting for differences between the two detectors.

In the TF configuration the shape of the asymmetry function is primarily determined by two effects. Precession of spins in the magnetic field gives the sinusoidal time dependence. Magnetic vortices and nuclear magnetic moments, however, make the local field spatially inhomogeneous, which causes eventual depolarisation of the antimuon spins. If $p\left(B_z\right)$ is the probability distribution of the z component of the local magnetic field across the sample, then the net polarisation of the antimuon spin as a function of time can be written as

$$P_x\left(t\right) \propto \int p\left(B_z\right)\cos\left(\gamma_\mu B_z t + \varphi\right) dB_z, \tag{2.52}$$

where φ is the initial phase given by the initial polarisation of spins. This means that $P_x\left(t\right)$ and $p\left(B_z\right)$ are related via a Fourier transform. The typical shape of the magnetic field strength distribution in the vortex phase for low external field is displayed in Figure
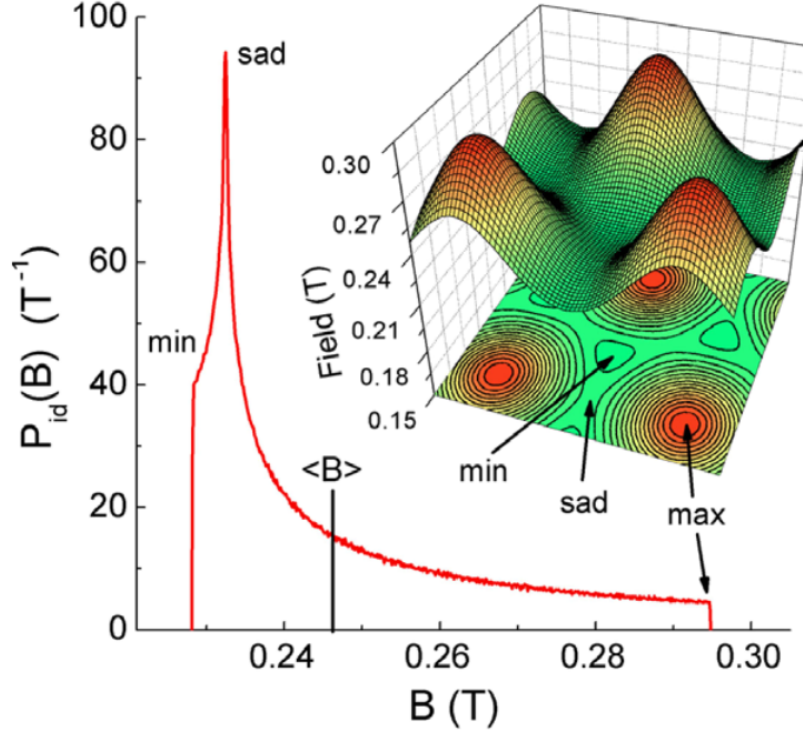
Figure 2.6: Spatial distribution function and contour plot of magnetic field strength in a vortex lattice (from reference [90]).

2.6. In TF μSR experiments the external field is often high enough for $p\left(B_z\right)$ to become similar to a Gaussian distribution. The resultant polarisation function $P_x\left(t\right)$ is then well described by the product of cosine and Gaussian exponent:

$$P_x\left(t\right) \propto \exp\left(-\sigma^2 t^2/2\right) \cos\left(\gamma_\mu \left\langle B_z\right\rangle t + \varphi\right), \tag{2.53}$$

where $\left\langle B_z\right\rangle$ is the average magnetic field strength in z direction at the muon site and σ is the muon spin depolarisation rate. In case it is possible to distinguish different kinds of muon sites, the polarisation function can be fitted with a sum of given functions with different σ and $\left\langle B_z\right\rangle$. In a non-superconducting phase the depolarisation rate, σ_n, is mainly determined by nuclear magnetic moments and at low temperature is effectively constant. In the superconducting phase the vortex lattice adds another contribution, σ_{sc}, which is a function of temperature, T. The overall depolarisation rate is obtained by adding the individual contributions in quadrature:

$$\sigma^2\left(T\right) = \sigma_{sc}^2\left(T\right) + \sigma_n^2. \tag{2.54}$$

Depolarisation rate due to a vortex lattice is related to the variance of the local magnetic field strength, which in turn is related to the London penetration depth λ:

$$\sigma_{sc}^2\left(T\right) = \gamma_\mu^2 \left\langle \Delta B^2 \right\rangle, \tag{2.55}$$

$$\left\langle \Delta B^2 \right\rangle = 0.003710 \Phi_0^2/\lambda^4. \tag{2.56}$$

40

Combining these two expressions together gives a simple formula with λ in nm and σ_{sc} in μs^{-1}:

$$\lambda = 327.5/\sqrt{\sigma_{sc}}. \tag{2.57}$$

The field distribution can in practice be quite far from the Gaussian one, and a different empirical formula is used instead:

$$\lambda = 270/\sqrt{\sigma_{sc}}. \tag{2.58}$$

The penetration depth (and therefore σ_{sc}) depends on the superfluid electron density n_s (Equation 2.38). Obtaining its temperature dependence is usually the aim of TF μSR experiments. $\sigma_{sc}(T)$ can be fitted with different shapes of $n_s(T)$, calculated using various superconducting gap function symmetries. This can help to determine the most likely symmetry and check for the existence of a multi-band superconductivity [91].

2.5 Quantum oscillations

In 1930 in his work "Diamagnetism of metals" [92] Landau stated that at sufficiently low temperatures and high magnetic fields magnetisation of metals is expected to have a strong non-linear and periodic field dependence. At the same time, he said that this effect is unlikely to be observed experimentally due to homogeneous enough magnetic field not being achievable in practice. Even before this was published similar behaviour of magnetoresistance in bismuth single crystals was seen by Shubnikov and de Haas [93]. Later in the same year de Haas and van Alphen, unaware of Landau's predictions, detected field dependent oscillations of magnetisation, also in bismuth [94]. This kind of field dependence of magnetisation (or magnetic susceptibility) and electrical resistivity in metals, periodic in the inverse of magnetic field, became known respectively as the de Haas van Alphen (dHvA) effect and the Shubnikov de Haas (SdH) effect. Such periodicity is also characteristic for many other physical properties, and these phenomena are collectively known as quantum oscillations.

During the next few decades after quantum oscillations were discovered a theory describing them was gradually developed. An important milestone was relating the period of an oscillation to the geometry of the Fermi surface of a material [95]. Advances in methods of an experimental detection of the phenomenon have simultaneously been made, and the oscillations were consequently observed in more metals [96]. Quantum oscillations have since evolved into a very neat and robust experimental technique and are widely used today for probing the electronic structure of metals. A book by Schoenberg [97] comprehensively describes many aspects of the phenomenon. A brief outline of the theory behind quantum oscillations and its main results are presented below.

According to a semi-classical picture, in presence of magnetic field **B** conduction electrons in a metal moving at speed **v** are subjected to the Lorentz force, resulting in a
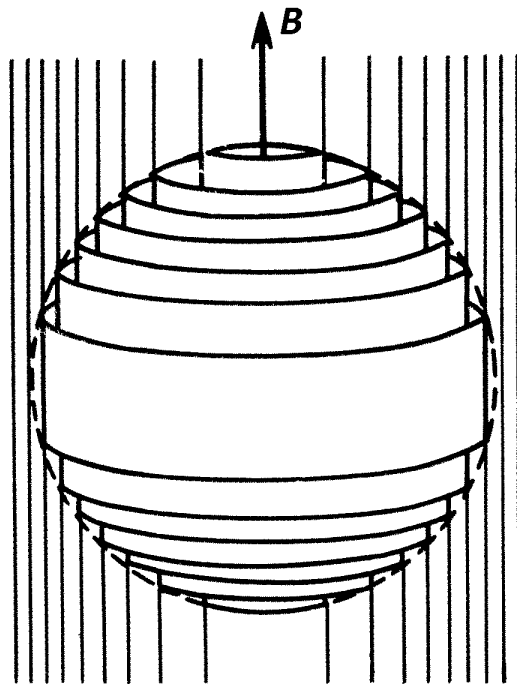
Figure 2.7: Landau tubes indicating the *k*-states within the Fermi surface (dashed line) occupied by electrons in magnetic field *B* (diagram from [97]).

change of their momentum at the rate

$$\hbar\dot{\mathbf{k}} = -e\mathbf{v} \times \mathbf{B}. \tag{2.59}$$

Since $\dot{\mathbf{k}}$ is perpendicular to $\mathbf{B}$, and no work is being done by the Lorentz force, the motion of electron in the *k*-space happens along the orbits formed by the intersection of the constant energy surfaces with the plane perpendicular to $\mathbf{B}$. Solving Schrodinger's equation for free electrons in magnetic field in *z* direction shows that energy ε becomes quantised given a fixed value of the *z* component of the wavenumber k_z:

$$\varepsilon = \frac{e\hbar B}{m_e}\left(r + \frac{1}{2}\right) + \frac{\hbar^2 k_z^2}{2m_e}, \tag{2.60}$$

where *r* is a non-negative integer and m_e is the free electron mass. The quantisation determines the allowed values of the wavevector component perpendicular to the field direction:

$$\frac{\hbar^2}{2m_e}\left(k_x^2 + k_y^2\right) = \frac{e\hbar B}{m_e}\left(r + \frac{1}{2}\right). \tag{2.61}$$

This means that in the *k*-space electronic states are contained within the so called Landau tubes, as illustrated in Figure 2.7.

Increasing the magnetic field strength results in the expansion of the Landau tubes. As the radius of the outermost Landau tube approaches the radius of the extremal cross-section of the Fermi surface perpendicular to $\mathbf{B}$, the density of states at the Fermi level diverges. Upon further increase of the field strength the Landau tube height shrinks to zero and the density of states drops sharply. From Equation 2.61 it can be seen that this

pattern will repeat itself every time the value of $1/B$ changes by

$$\Delta \left(\frac{1}{B} \right) = \frac{1}{F} = \frac{2\pi e}{\hbar A_k}, \tag{2.62}$$

where F is the corresponding frequency and A_k is the extremal area of the Fermi surface cross-section perpendicular to the magnetic field. This variation of the density of states translates to quantum oscillations in many physical properties.

Through a rather involved derivation [97] one can show that the grand thermodynamic potential of electrons in a metal in magnetic field has an oscillatory component $\widetilde{\Omega}$ with the following field dependence:

$$\widetilde{\Omega} \propto B^{5/2} \sum_{p=1}^{\infty} \frac{1}{p^{5/2}} \cos \left(2\pi p \left(\frac{F}{B} - \frac{1}{2} \right) \pm \frac{\pi}{4} \right). \tag{2.63}$$

The result is valid for a perfect crystal at zero temperature and neglects interaction of spins with the magnetic field. The sum appears as a result of the Fourier series decomposition, and p denotes the harmonics. A phase shift of $\pi/4$ is positive or negative depending on whether the extremal area of the Fermi surface is respectively a minimum (neck) or a maximum (belly). Magnetisation along the field direction can be found by differentiating $\widetilde{\Omega}$ with respect to B, and differentiating once again gives the corresponding component of the magnetic susceptibility $\widetilde{\chi}$.

In order to make the theory more applicable, one needs to account for imperfections of the crystal, the finite temperature and the spins of electrons. It turns out that the influences of these effects can be thought of as a superposition of multiple oscillations with phase shifts varying according to some distributions. This "phase smearing" is equivalent to multiplying the amplitude of the oscillations by a reducing factor. For a given effect this factor happens to be related to the Fourier transform of the corresponding phase shift distribution.

Temperature enters the model through the Fermi-Dirac distribution (Equation 2.10). Reduction of the amplitude therefore happens as a result of the smearing of the Fermi surface due to the broadening of the jump in the Fermi-Dirac distribution at a finite temperature. This translates to the broadening of the frequency F, equivalent to the phase smearing. The resultant reduction factor for the p-th harmonic is

$$R_T = \frac{2\pi^2 p k_B T m^* / e\hbar B}{\sinh \left(2\pi^2 p k_B T m^* / e\hbar B \right)}, \tag{2.64}$$

where effective quasiparticle mass m^* is used, extending the theory to systems with interacting electrons.

The effect of crystalline defects and impurities can be quantified by the mean scattering time τ. It follows from the uncertainty principle that due to a finite scattering time there is an uncertainty in the energy levels, equivalent to the broadening of the Fermi energy. This broadening can be characterised by a Lorentzian distribution [98] and the amplitude

of quantum oscillations is therefore scaled by a factor

$$R_D = \exp\left(-\pi p m^*/eB\tau\right) = \exp\left(-2\pi^2 p k_B T_D m^*/e\hbar B\right), \tag{2.65}$$

known as the Dingle factor. In order to make the expression similar the Equation 2.64, a parameter $T_D = \hbar/2\pi k_B\tau$, called the Dingle temperature, was introduced. Assuming a spherical Fermi surface and using the Equations 2.18 and 2.62 the Dingle temperature can be used to provide a measure of the mean free path:

$$l = \frac{\sqrt{2e\hbar^3 F}}{2\pi m^* k_B T_D}. \tag{2.66}$$

In a magnetic field the spin degeneracy of electrons is lifted and each energy level splits into two levels separated by energy

$$\Delta\varepsilon = \frac{1}{2}g\hbar eB/m_e, \tag{2.67}$$

where g is the spin g-factor, often allowed to be taken as 2. Fermi energies of electrons with different spins become separated by $\Delta\varepsilon$, and the oscillations therefore have two components with the phase difference of

$$\Delta\phi = 2\pi\frac{\Delta\varepsilon}{e\hbar B/m^*}, \tag{2.68}$$

where the denominator is the energy difference between a pair of neighbouring Landau tubes. For the p-th harmonic the superposition of the two oscillations is equivalent to multiplying the amplitude by the factor

$$R_s = \cos\left(\frac{1}{2}p\Delta\phi\right) = \cos\left(\frac{1}{2}p\pi g\frac{m^*}{m_e}\right), \tag{2.69}$$

where Equations 2.67 and 2.68 were applied.

When all mentioned corrections are taken into account, the final formula describing quantum oscillations, called the Lifshitz-Kosevich formula (or the LK formula) [99], can be obtained. The most significant contribution to the oscillations in magnetic susceptibility (dHvA effect) along the field direction is given by

$$\widetilde{\chi} = \left(\frac{8\pi e^3}{\hbar^3}\right)^{1/2}\frac{k_B T F^2}{|A_k''|^{1/2}B^{5/2}}\sum_{p=1}^{\infty}\frac{\exp\left(-2\pi^2 p k_B T_D m^*/e\hbar B\right)\cos\left(\frac{1}{2}p\pi g\frac{m^*}{m_e}\right)}{p^{-1/2}\sinh\left(2\pi^2 p k_B T m^*/e\hbar B\right)}$$
$$\times\cos\left(2\pi p\left(\frac{F}{B}-\frac{1}{2}\right)\pm\frac{\pi}{4}\right), \tag{2.70}$$

where A_k'' is the curvature of the Fermi surface along the magnetic field direction at the extremal orbit, i.e. if the extremal cross-section is located at $k_z = \kappa$, then $A_k'' = \left.\frac{\partial A_k}{\partial k_z}\right|_{k_z=\kappa}$. The formula is expected to be valid for $F \gg B$. For crystals with more than one Fermi surface, multiple oscillations add up. The LK formula for electrical resistivity (the SdH

effect) is

$$\rho \propto \left(\frac{8\pi}{e\hbar^7}\right)^{1/2} \frac{m^{*2}k_BT}{\left|A_k''\right|^{1/2}B^{1/2}} \sum_{p=1}^{\infty} \frac{\exp\left(-2\pi^2 p k_B T_D m^*/e\hbar B\right)\cos\left(\frac{1}{2}p\pi g\frac{m^*}{m_e}\right)}{p^{-1/2}\sinh\left(2\pi^2 p k_B T m^*/e\hbar B\right)}$$

$$\times \cos\left(2\pi p\left(\frac{F}{B}-\frac{1}{2}\right)\pm\frac{\pi}{4}\right). \quad (2.71)$$

It is often enough to include only the fundamental component of the oscillations. In that case Equation 2.70 can be rewritten in as

$$\widetilde{\chi} = \left(\frac{8\pi e^3}{\hbar^3}\right)^{1/2} \frac{k_B T F^2}{\left|A_k''\right|^{1/2}B^{5/2}} \frac{\exp\left(-2\pi^2 k_B T_D m^*/e\hbar B\right)\cos\left(\frac{1}{2}\pi g\frac{m^*}{m_e}\right)}{\sinh\left(2\pi^2 k_B T m^*/e\hbar B\right)}$$

$$\times \cos\left(2\pi\left(\frac{F}{B}-\frac{1}{2}\right)\pm\frac{\pi}{4}\right). \quad (2.72)$$

The most obvious use for quantum oscillations is mapping the geometry of a Fermi surface by looking at the frequency of the oscillations. Information about the three-dimensional structure can be obtained from studies with varying angle between the sample orientation and the magnetic field direction. For non-trivial geometries experimental results alone are often insufficient for determining the shape of the Fermi surface. In practice the Fermi surface is typically predicted by theoretical numerical calculations and the expected quantum oscillation frequencies are compared to the experimentally obtained ones. Thanks to the finite temperature correction (Equation 2.64), recording quantum oscillations at different temperatures and analysing the resultant change in the amplitude allows to extract the values of the effective quasiparticle masses. Once the mass is known, the Dingle temperature can be found by analysing the field dependence of the amplitude, and used for calculating the mean free path according to Equation 2.66. All this illustrates why a measurement of quantum oscillations is such a powerful experimental technique.

3 Experimental techniques

3.1 Cooling techniques

3.1.1 Liquid helium refrigeration

Since the invention of the first large scale helium liquefier by Kapitza in 1934 [100], liquid helium refrigeration has always been an essential technique in experimental condensed matter physics. Nowadays there exist two commonly used methods of liquid helium based refrigeration: evaporative cooling and dilution refrigeration. Detailed descriptions of these methods and their implementations can be found in the literature [101, 102]. The basic principles behind these cooling techniques and the operation of the cryostats actively used in this work are described below.

At atmospheric pressure helium-4 gas condenses at the temperature of 4.2 K. Pumping away the vapour above the liquid helium causes the condensate to actively evaporate. Faster atoms are more likely to escape from the liquid, and as they do so, the average energy of the remaining atoms drops. This phenomenon is known as evaporative cooling and can be used in practice to cool down helium-4 to about 1.3 K. With helium-3 even lower temperatures can be reached. First, using helium-4 refrigeration, helium-3 needs to be cooled down to 3.2 K for its condensation. Pumping on liquid helium-3 allows to achieve temperatures as low as 0.2 K. Intermediate temperatures can be maintained by balancing the cooling power with the heat generated using resistive heaters. When all the helium-3 has evaporated the refrigeration stops and the gas needs to be recondensed. Such a mode of operation is known as the one-shot mode. Alternatively, designs of some cryostats allow for uninterrupted cooling with continuous condensation of the evaporated helium-3. These are known as continuous flow cryostats.

The Physical Property Measurement System (PPMS) made by Quantum Design is a popular commercially available helium-4 cryostat, which was routinely used in this work for measuring electrical resistivity and heat capacity. The design of the main part of the PPMS is displayed in Figure 3.1. In its default configuration the device allows cooling samples down nominally to 1.9 K (although in practice it is sometimes possible to go down to 1.7 K). One of the defining features of the system is its interface for loading samples into the cryostat. Samples are mounted on a removable stage called a "puck". It is then inserted into the cryostat and connected to the bottom of the sample space through a 12-pin socket. The pins provide the necessary electrical connections for probing the sample. There exists a variety of add-ons for the PPMS enhancing its performance or enabling more types of measurements. One such add-on, used actively for some of the work described in this thesis, is the helium-3 probe. It is installed via an insertion into the bore of the cryostat and allows cooling samples down to 350 mK temperature with the continuous-flow operation available. The variant of the PPMS used for this work also contains a built-in 9 T superconducting electromagnet providing magnetic field along the axis of the bore.

Dilution refrigeration is a more advanced cooling technique allowing one to reach temperatures of the order of 1 mK. The method uses both helium-3 and helium-4
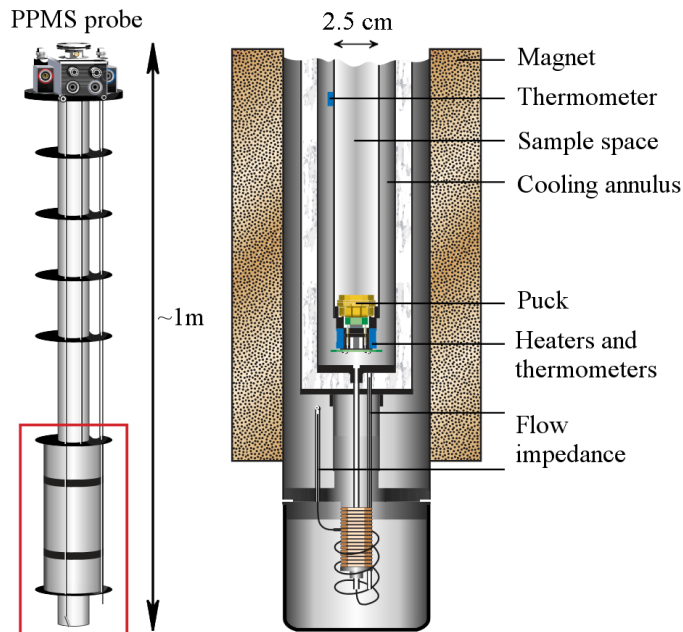
Figure 3.1: Schematic diagram of the PPMS cryostat design. The probe shown in the left sits inside a dewar with liquid nitrogen and liquid helium-4 compartments. The right part of the diagram describes the lowest part of the probe, marked by the red rectangle on the left. The diagram is copied from the PPMS advertising brochure [103].

isotopes. Below approximately 870 mK their mixture spontaneously separates into a ^{3}He-rich phase and a ^{3}He-poor phase. The exact compositions of these phases are temperature dependent. For example, at millikelvin temperatures the ^{3}He-rich phase is nearly pure helium-3, and the ^{3}He-poor phase is approximately a mixture of 7% of helium-3 and 93% of helium-4. The two liquids are located in the mixing chamber of a dilution refrigerator and are separated by a phase boundary. Pumping on the mixture makes helium-3 evaporate more actively than its heavier isotope. As a result, the ^{3}He-poor phase becomes unbalanced and helium-3 flows from the ^{3}He-rich part into the ^{3}He-poor one. Crossing the phase boundary requires energy, which comes from the heat of the mixing chamber walls, which are cooled down as a result. The evaporated helium-3 is recondensed and used to replenish the ^{3}He-rich part. Thus, continuous operation can be achieved. Intermediate temperatures can once again be maintained with the help of heaters, but since the mixture always needs to be below the phase separation temperature to provide the cooling power, dilution refrigerators typically cannot go far above 1 K without stopping the dilution process.

3.1.2 Adiabatic demagnetisation refrigerator

One of the main disadvantages of liquid helium refrigeration is the ever-increasing price of helium. One common way of circumventing this problem is keeping the cryogen in a closed circulation. Nonetheless, there is a stimulus to develop cooling techniques which do not rely on liquid cryogens. Cryostats based on such techniques are known as "dry" cryostats.
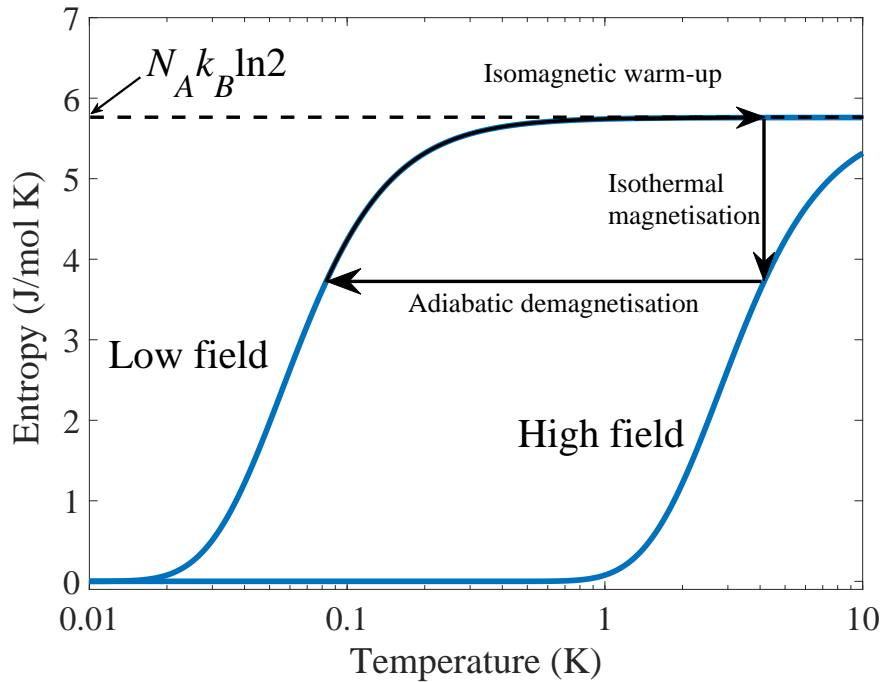
Figure 3.2: Thermodynamic cycle of the ADR process for a spin-1/2 system. N_A – Avogadro constant, k_B – Boltzmann constant.

The DMS-1000, developed by Dryogenic (the company has since gone out of business), is an example of such cryostat. It combines adiabatic demagnetisation refrigeration (ADR) and pulse tube-refrigeration (PTR) techniques in order to achieve approximately 100 mK in temperature.

Pulse-tube refrigeration is a fairly advanced cryogen-free cooling technique. It uses helium gas undergoing periodic compression in order to transport heat against a thermal gradient. Modern pulse-tube refrigerators (also called pulse tube cryocoolers) can provide a continuous cooling from room temperature down to below 2 K [104]. The principles behind the PTR will not be described here, but their explanation can be found in the literature [105, 106].

In the DMS-1000 the pulse tube refrigerator acts as a first stage of the cooling, maintaining the temperature inside the cryostat at about 4 K. From this point the ADR is used for achieving sub-Kelvin temperatures. The ADR is based on the magnetocaloric effect [107]. The cooling element is a cylinder of paramagnetic polycrystalline salt, colloquially called the salt pill. The main property of the salt is a strong dependence of its entropy on magnetic field. At zero field the system has high entropy due to random orientation of its magnetic moments. When the field is increased the entropy drops as the moments become ordered. The thermodynamic cycle describing the cooling sequence is displayed in Figure 3.2. Salts commonly used for ADR include ferric ammonium alum (FAA) and potassium chrome alum (CPA).

Figure 3.3 shows a diagram of the DMS-1000 probe. During the measurement the probe is located inside an evacuated steel can. Two sets of spring-loaded pins in the middle section of the probe provide thermal contact between the two. The can is inserted
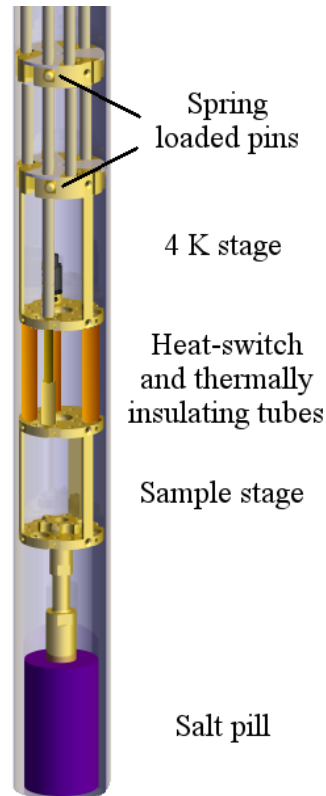
Figure 3.3: Schematic diagram of the low temperature part of the DMS-1000 ADR cryostat. The diagram was made using an image from the cryostat software.

into the bore of the cryostat where the pulse tube cryocooler cools down the section of the probe below the bottom set of pins to about 4 K. Cooling down to this point from room temperature takes about 10 hours. The salt pill is surrounded by a 7 T superconducting magnet. The cooling cycle starts with ramping up the field with the heat switch closed. This heats up the salt pill, but the heat can flow out of it. At the highest field, when the temperature has equilibrated, the heat switch is opened and the field is gradually ramped down over the course of about half an hour. At this point the sample stage is linked to the 4 K stage through a set of tubes made of Kapton, fiberglass or other materials with low thermal conductivity (there is also a bundle of wires going down to the sample stage). This creates adiabatic conditions for the salt pill and the sample stage. The increase of the entropy of the salt pill is matched by the decrease of the entropy of the sample stage and its payload, which are cooled as a result. By the time the magnetic field reaches zero the salt pill cools down to approximately 100 mK. Due to the high heat capacity of the salt pill and the good thermal insulation of the sample stage such level of temperature can be maintained for several hours until the heat leakage eventually brings the temperature up. The sample stage is surrounded by another 7 T superconducting magnet for applying field to the sample.

3.2   Electrical resistivity measurements

The measurement of electrical resistivity is one of the most common techniques used in the experimental condensed matter physics. Applications of this technique include detection of phase transitions, study of electron-phonon interactions and testing purity of samples, to name a few. The standard way of measuring electrical resistivity is the four-point method, in which four wires are connected to a sample at different points. Two wires are used for passing a current through the sample and the other two measure the potential difference developed as a result. Voltage measurement devices typically have very high input impedance, so the current flowing in their leads is negligible. Thus, the resistance of the voltage wires does not contribute to the measured voltage drop and the resistance of the sample can be calculated by simply dividing the potential difference across it by the current flowing through it. The geometry of the sample and locations of the contacts can be used for converting the resistance to the resistivity.

While the basic principle behind the technique is very simple, in practice one often has to look for ways of increasing the signal-to-noise ratio. It is common to conduct resistivity measurements using an AC current and lock-in amplifiers, as this minimises the problem of electrical interference. An AC measurement also permits the use of transformers for signal amplification. The signal-to-noise ratio can also be improved by directly increasing the resistance of the sample via increasing the ratio of its length to its cross-sectional area and placing the positive and negative contacts further away from each other.

Making electrical contacts with the sample is a crucial part of preparing a measurement. The contacts must be ohmic and should have a low resistance and a small contact area. Gold, silver or platinum wires of 25 µm or 10 µm diameter are typically used for making the contacts. For metallic samples the lowest contact resistance is typically achieved with spot welding. In this method the connection is made by pressing a wire against the sample and passing a pulse of current through their point of contact. The electrical resistance at this point is initially of the order of 10 Ω. When a voltage of several volts is suddenly applied across the junction, the dissipation causes the interface to heat up enough to locally melt the metals and fuse the wire and the sample together. When choosing the pulse voltage one should generally go for a value which results in a mechanically robust connection with minimal damage to the sample. The resistance of spot-welded contacts normally does not exceed 0.1 Ω, and their typical contact area is of the order of several square microns. Such contacts are usually strong enough on their own, but for further robustness they can be covered with a small amount of silver loaded epoxy.

The spot welding works well with samples larger than about 0.5 mm in length and thick enough to withstand the force applied for pressing the wire against the sample. The method can, in principle, be used with even smaller samples, but in practice they often prove to be too brittle. An alternative way of making contacts is using a glue loaded with silver particles. The wires are stuck to the sample and once the glue dries the silver provides good electrical conductivity. The glue should be applied in small amounts, as too much of it makes the contact area too large and leads to a risk of inadvertently joining the contacts together. A small diameter wire or an eyelash work well as a brush for

the application process. The 6838 silver loaded epoxy by DuPont provides a very strong connection, but needs to be cured at a high temperature (160 °C–200 °C) for 1.5 to 2 hours. For heat sensitive samples it is advised to use the 4929 variant, which sets at room temperature, but provides poorer adhesion. Yet another option is CircuitWorks CW2400 – a two component silver-loaded epoxy having a rather flexible curing schedule, good mechanical properties and strong adhesion. When preparing samples for resistivity measurements under high pressure, it must be kept in mind that some pressure media, such as methanol-ethanol, can dissolve certain types of glue.

Most types of conductive silver glue used with metallic samples typically produce contact resistance of the order of 1 Ω. However, in the case of YFe_2Ge_2 abnormally high (>100 Ω) contact resistance was observed on several occasions when such a method of making contacts had been used. This could have been caused by the formation of an insulating oxide layer on the surface of the sample. Most of the time the problem can be remedied by pulsing a current through the contacts using a spot welder or a DC current source. Bursts of current gradually improve the electrical connection, reducing the contact resistance down to a couple of ohms.

3.3   Heat capacity measurements

Measurements of heat capacity can be extremely useful for probing electronic properties of crystals. As was explained earlier (Equation 2.14) low temperature heat capacity provides a measure of the effective quasiparticle mass. Heat capacity measurements are especially important when studying superconductors, since the size of the associated anomaly (Figure 2.5) provides information about the superconducting volume fraction and the temperature dependence of the heat capacity in the superconducting state can reveal the symmetry of the gap function.

Measurements of the YFe_2Ge_2 heat capacity have been conducted in the PPMS down to 350 mK temperature. The schematic diagram of the heat capacity puck is displayed in Figure 3.4. A sample, usually of approximately 5 mg mass, is thermally coupled to a platform through Apiezon grease. The amount of grease has to be sufficient for providing a good thermal contact, but not large enough to give a noticeable contribution to the measured quantity. The heat capacity of the platform (the addenda heat capacity) needs to be measured beforehand using a calibration routine. The platform contains a heater for applying thermal power to the sample (and the platform) and a thermometer for monitoring the sample temperature. Thin wires made of a platinum alloy couple the platform to the frame of the puck, which acts as a thermal bath. The PPMS sample chamber is kept at high vacuum during the measurement.

The PPMS uses the relaxation technique for measuring heat capacity. The measurement cycle starts with powering the heater for a brief amount of time and then letting the sample cool down. The time dependence of the platform thermometer reading is then fitted with a formula coming from a simple model describing the flow of heat between the sample, the platform and the bath. The value of the heat capacity is obtained from the fit. A detailed description of the model, as well as all other
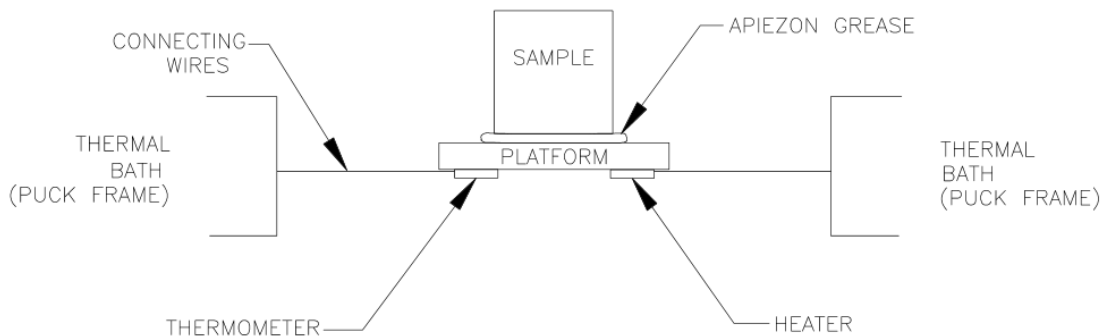
Figure 3.4: Schematic diagram of the PPMS heat capacity puck (from the PPMS user's manual).

information relevant to the method can be found in the PPMS user's manual.

3.4   High pressure techniques

Subjecting a crystal to a hydrostatic pressure, i.e. pressure generated by a fluid at equilibrium, changes the interatomic distances within the lattice. This can often have a strong effect not only on structural, but electronic, magnetic and other kinds of properties. Because of that, a hydrostatic pressure is an excellent tuning parameter for studying phases of solid matter.

High pressure environments are created with pressure cells. These come in different types, optimised for different ranges of pressure. High pressure experiments described in this thesis were conducted using piston-cylinder and moissanite/diamond anvil cells. They are described in the next two subsections. Pressure is applied to the sample through a pressure transmitting medium. It is typically a liquid characterised by its ability to maintain hydrostatic conditions at a high level of compression. Important parameters of pressure transmitting media are their hydrostaticity range and volatility. The most hydrostatic ones are liquid inert gases such as helium and argon. Their disadvantage is a complicated loading procedure, which has to be conducted at cryogenic temperatures. For pressures up to 100 kbar 4:1 methanol-ethanol or 1:1 pentane-isopentane mixtures work well [108], but they evaporate rather quickly at room temperature. Daphne oil 7373 or 7474 and glycerol are much easier to work with, but their hydrostaticity limits are between 20 and 50 kbar.

A limited sample space and the presence of a pressure transmitting medium generally makes conducting measurements under high pressure more complicated than under ambient conditions. For this reason, when studying materials under high pressure a lot of effort is put towards developing measurement techniques. Becoming efficient at setting up high pressure experiments, even using well-established methods, often requires a researcher to spend a fair amount of time practicing. Types of high pressure experiments described below are electrical resistivity measurements and skin depth measurements using a tunnel diode oscillator (TDO).
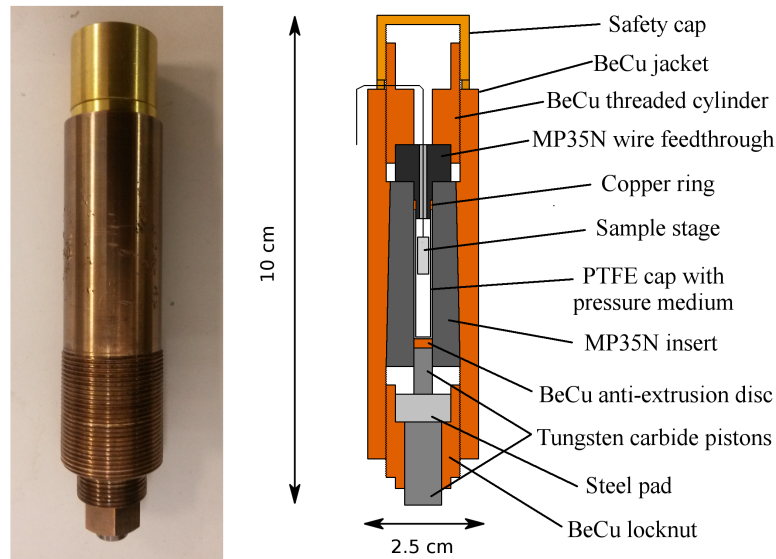
Figure 3.5: The photograph and the schematic diagram of a piston-cylinder cell.

3.4.1 Piston-cylinder cell

Piston-cylinder cells generate pressure as a result of a piston compressing the pressure transmitting medium inside a cylindrical bore of the cell. The variant used for this work is designed for pressures of up to 30 kbar. A schematic diagram of it can be seen in Figure 3.5. The central part of the cell is an approximately 5 cm-long insert made of the non-magnetic cobalt-nickel alloy MP35N. The piece has a 4 mm diameter bore where the sample space is located. The insert has a tapered shape and is pushed into a matching beryllium-copper jacket with the force of about 5000 N. This compresses the insert from the outside and increases the material's yield strength at the walls of the bore [109]. One end of the bore is covered by an MP35N feedthrough, which is used for getting the measurement leads into the sample space. A bundle of about 10 copper twisted pairs runs through a narrow channel along the feedthrough sealed with the Stycast 2850FT epoxy. A copper ring fits tightly between the feedthrough and the bore, sealing all the gaps. The samples are located inside the pressure transmitting medium contained within a 3 cm-long PTFE tube closed at one end. The force is applied to that end of the tube with a tungsten carbide piston through a beryllium-copper disc acting as a seal and preventing the PTFE tube from being extruded past the piston. At the opposite end the feedthrough is firmly secured in place by a threaded cylindrical beryllium-copper piece. A brass cap is used for protection in case the feedthrough blows out. The piston is supported by a steel cylinder which is held by a locknut. A fully assembled cell is about 2.5 cm in diameter and 10 cm in length, so it comfortably fits inside the bore of the PPMS cryostat. Mechanical properties of the cell are improved by heat treating the MP35N parts at 550 °C temperature for 5 hours and beryllium-copper parts at 330 °C for 3 hours. In order to apply the pressure the cell is first secured in a holder with the help of the thread on the outside of the jacket. A hydraulic ram is used to apply the force to a larger tungsten carbide piston pressing on the steel pad and pushing the smaller piston deeper into the cell. As the Teflon tube

is compressed the load is secured by the locknut. Reaching a 30 kbar pressure requires applying the force equivalent to about 4 tonnes. With the maximum compression of the Teflon tube at the highest pressure, the available sample space is 3 mm in diameter and about 1-1.5 cm in length. The number of samples in a single cell is, in principle, limited by the number of wires carried by the feedthrough. In practice, the cell is usually set up with three samples. In addition, a sample of tin is added in order to act as a pressure gauge. Pressure is determined from its superconducting critical temperature, which is calibrated against pressure. In order to make the process of mounting samples more convenient and reliable, the ends of the wires of the twisted pairs are threaded though the regularly spaced holes in a 2 by 8 mm piece of thin cardboard also acting as the sample stage. That way wires are kept at a fixed and comfortable separation for connecting them with the smaller wires contacted to the samples. Pressure transmitting media which can be loaded at room temperature and remain hydrostatic up to 30 kbar work well with such piston-cylinder cells.

3.4.2 Anvil cell

For generating pressures significantly above 30 kbar piston-cylinder cells described above are no longer practical. Instead, a type of cell known as an anvil cell is typically used. These cells come in a variety of designs, but in all of them the same principle is used for creating a high-pressure environment. The main parts of an anvil cell are a pair of anvils and a gasket. The anvils are made of a hard material and have a shape which includes a truncated cone or pyramid (with many edges). Their smaller base is known as the tip of the anvil or a culet. The gasket is a disc made of hard, yet ductile material with a small hole at its center. The hole contains a sample surrounded by a pressure transmitting medium. Pressure is generated by compressing the central part of the gasket between the culets of the two opposed anvils. Deformation of the gasket reduces the volume of the gasket hole and the force pressing the anvils into the gasket prevents the pressure medium from leaking out of the hole. It is important that the gasket deforms in a predictable manner, therefore its dimensions need to be carefully chosen. One important rule is that the diameter of the gasket hole has to be at least two times smaller than the culet diameter. The choice of the gasket material depends on the target pressure as well as the type and the desired sensitivity of the measurement. For example, gaskets made of stainless steel provide some magnetic background, yet are harder than those made of beryllium-copper. Anvil cells set up in the Cavendish Laboratory for the experiments described in this thesis used beryllium-copper as the gasket material. A quantitative analysis of the gasket properties together with a very detailed description of many aspects of high pressure experiments can be found in the PhD thesis of Dr Patricia Alireza [110] as well as in the references [111, 112].

A schematic diagram of the anvil cell design used in the Cavendish Laboratory can be seen in Figure 3.6. All parts of the cell, with the exception of the anvils, are made of heat-treated beryllium-copper alloy. With a small amount of glue the anvils are secured in the pistons, which sit inside the cell body and are held by the backing plates on both
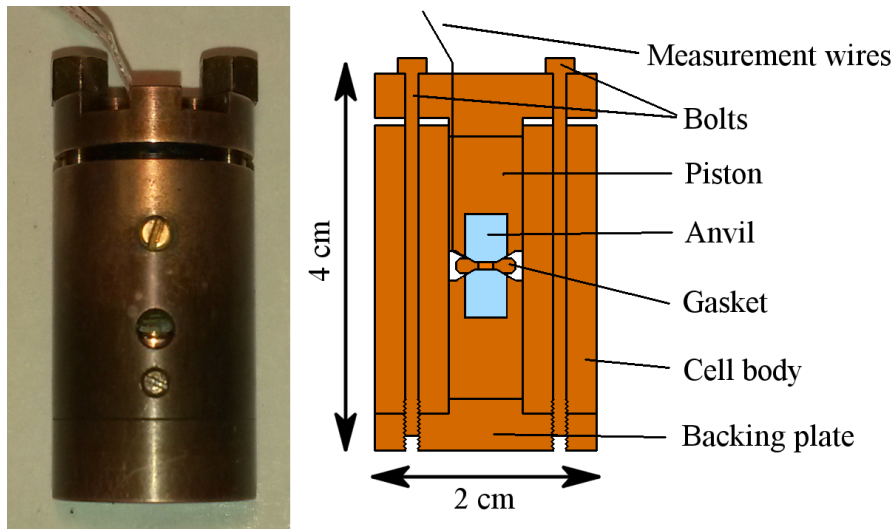
Figure 3.6: Photograph and schematic diagram of an anvil cell design used in the Cavendish Laboratory.

sides. The force is applied with a hydraulic ram and locked in with a pair of bolts. Because of its hardness, diamond is considered to be the best anvil material. There are also cheaper alternatives. Anvil cells prepared in the Cavendish Laboratory for the experiments described in this thesis used anvils made of moissanite, a form of silicon carbide. Moissanite is a rare naturally occurring transparent mineral. It has a hardness of 9.5 on the Mohs scale, as opposed to 10 for a diamond [113]. Artificially synthesised moissanite is used as the anvil material. Cells with anvils made of these minerals are commonly referred to as moissanite/diamond anvil cells (MAC or DAC). The transparency of diamond and moissanite provides the optical access to the sample space along the axis of the cell. For the given anvil cell design the highest pressure that can be achieved depends primarily on the anvil material and the culet diameter. A pair of moissanite anvils with 0.8 mm diameter culets (used for this work) can in principle generate pressures of up to 130 kbar. This corresponds to a loading force of several kN. Smaller culet areas give higher pressures, but at the same time reduce the size of the sample space.

When beginning to set up a moissanite anvil cell it is important to ensure that the two anvils have concentric and parallel culets. This can be done by assembling the cell without the gasket and looking at the interface between the two culets. Relative horizontal alignment is indicated by how well the culet areas overlap. For checking whether the culets are parallel one should look at the interference pattern at the interface. If the culets are slightly convex, they produce a circular pattern, which should be concentric with the the culets. If the culets are flat, the number of the interference fringes should be as low as possible.

The most important part of setting up an anvil cell is preparing a gasket. The procedure differs based on the type of measurement to be conducted. The types discussed here are the four-point electrical resistivity and the TDO skin depth measurements. The corresponding pressure cells will be referred to as resistivity cells and TDO cells. The starting material for the gasket is an 8 mm diameter beryllium-copper

disc of a few hundred micron thickness (beryllium-copper sheets used for producing gaskets for this work had 370 µm or 560 µm thickness). The first task is pre-indenting the central part of the gasket to the right thickness by squeezing it between the two anvils. During the pre-indentation and afterwards the gasket should remain in fixed lateral orientation with respect to the anvils. In order to achieve that, three equally spaced 600 µm holes need to be drilled along the edge of the gasket with the help of a custom made jig. The pistons also have three matching holes on the same side where the anvils sit. The upper piston in Figure 3.6 needs to be inverted and short segments of 500 µm beryllium-copper wire should be secured inside these holes with glue in order to form three vertical pins. The gasket can then be mounted onto these pins using the previously drilled holes. To start the pre-indentation the cell needs to be put together and placed under a hydraulic ram. By applying force in small increments the thickness of the central part of the gasket should be brought down to the desired level: 70-80 µm for resistivity cells and, 130 µm for TDO cells (if the target pressure is close to 10 GPa then the thickness should be about 70-80 µm in both cases). One then has to drill a hole exactly at the centre of the flat pre-indented region. For the 0.8 mm diameter culets the hole diameter must be no more than 0.4 mm. Larger holes tend to radially expand under pressure and eventually fail to contain the pressure medium. To provide the space for the measurement leads to go past the gasket, its edges need to be slightly trimmed (the holes for mounting the gasket should be kept intact). Afterwards, the gasket has to be removed from the anvil and hardened with a 10-15 minute heat treatment at 330 °C (this applies to beryllium-copper gaskets). The gasket then needs to be put back onto the piston with the anvil, and all remaining procedures are to be conducted on the exposed face of the gasket. Figure 3.7 shows how the parts should look like at this stage.

In resistivity cells wires connected to the sample pass between the gasket and the lower anvil in Figure 3.6. In order to avoid a short circuit through the gasket, its surface needs to be insulated. This is done by spreading a mixture of alumina powder and Stycast 1266 epoxy across the surface of the gasket. The part that comes into contact with the anvil should be covered with an approximately 10 µm thick layer of epoxy saturated with alumina. When preparing the mixture the alumina powder should be added to the epoxy until the mixture starts to crumble upon stirring and rather than remaining in a single blob. The area outside the pre-indented space can be covered with a slightly thicker layer of less saturated mixture. Once the insulation is applied the gasket can be put into a 100 °C oven for five minutes in order to slightly harden the epoxy and make the insulation more mouldable. It can then be neatened up, and some dry alumina powder can be spread over the insulation in order to saturate the mixture even more and prevent it from sticking to the anvil. Afterwards the cell is closed under about 1 kN of force and put into an oven for one hour for fully curing the epoxy. The mixture should spread evenly under the force, resulting in a uniform insulating layer. After the curing, the gasket hole needs to be cleaned of the insulating mixture that flowed into it. The sample can then be placed into the hole with the wires extending to the outer part of the gasket as shown in Figure 3.8. The sample wires are connected to the external leads, which need to be securely
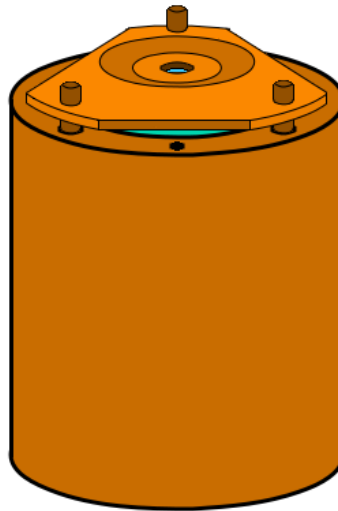
Figure 3.7: Schematic representation of a pre-indented and trimmed anvil cell gasket mounted on a piston with the help of three guiding pins. In Figure 3.6 this piston is the top one.

attached to the gasket (but not electrically connected to it) outside the pre-indented area. A piece of ruby is placed into the sample space for the pressure determination using ruby fluorescence spectroscopy. A droplet of pressure medium is added to fill the sample space. When doing that, there is a risk of the ruby floating away from the hole. To avoid that, a tiny amount of vacuum grease can be used to hold the ruby still.

Afterwards, the cell is ready to be pressurised. In order to seal the sample space one needs to apply enough force to start deforming the gasket. About 1.5 kN should be a safe starting point. As the force is applied, it needs to be secured with the designated bolts. The two bolts should be evenly tightened with a spanner. As they are tightened, at some point the force indicated by the pressure gauge will start to drop, meaning that the loading force is transferred to the bolts. One should not tighten the bolts beyond this point. Once the target force is reached and secured, the cell can be removed from the ram. Pressure inside the sample space can then be determined from the ruby fluorescence wavelength.

Gaskets for TDO cells are generally easier to prepare. First, a coil of cylindrical shape needs to be made. For a 0.4 mm diameter sample space the coil diameter needs to be about 250 µm in order to account for the eventual shrinking of the gasket hole. A 7-8 turn coil made using a 12 µm diameter insulated copper wire should be suitable for the sample space of 130 µm height. Thicker wire allows fewer turns, which lowers sensitivity of the coil. Wire of smaller diameter is much harder to work with because of how easy it is to snap it. The coil can be manually wound around the smooth end of a 250 µm diameter drill bit using a simple coil winder (a rotating axle with a chuck for holding the drill bit). GE varnish can be applied to prevent the coil from unwinding, after which the it needs to
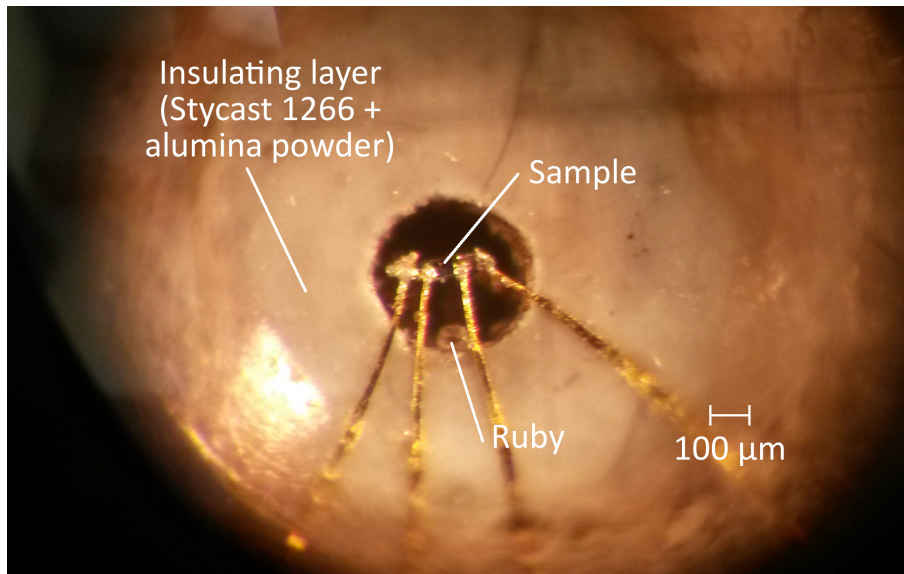
Figure 3.8: The photograph of the central part of a moissanite anvil cell gasket, set up for a resistivity measurement.

be carefully removed from the drill bit. The loose ends of the coil wire should be made at least 4-5 mm long. While multi-layer coils do in principle work as well, at typical TDO frequencies (above 10 MHz) the inner layers tend to shield the sample from the outer ones, resulting in no overall improvement.

The coil wires come out of the compressed section of the gasket via two radial channels. They should be of approximately 50 µm depth and width and close to each other. A scalpel can be used for cutting the channels, which can then be smoothed out with the tip of a sewing needle. At the points where the channels transition into the sample space it is advised to smooth out the sharp edges. The channels should be filled with the previously described insulating mixture of alumina powder and Stycast 1266 epoxy until it is flush with the gasket's surface. The coil then needs to be placed inside the sample space, and its wires must be immersed into the channels with the help of a needle or a similarly pointy object. Throughout the length of the channels the copper wires should not come into contact with the metal of the gasket, since even a slightest deformation of the latter can result in a short circuit or a broken electrical continuity. At the end of this step it is crucial to ensure that the insulating mixture is still flush with the gasket's surface. Heating the epoxy for a few minutes to make it more viscous can help spreading it in a desired manner. The area outside the indented part of the gasket can also be covered with the insulating mixture in order to prevent accidental short circuits and provide an insulating platform for contacting the coil wires. After curing the epoxy the loose ends of the coil wires have to be connected to a section of a coaxial copper cable. The best place to make the connection is on top of the insulated area of the gasket, near a trimmed edge. The coaxial cable should be securely attached to the gasket next to the joint (with some epoxy or glue), while the other end should come out of the cell through a channel in the piston holding the gasket. The coil wires next to the connection should be kept close to each other to reduce the loop area contributing parasitic inductance, which reduces sensitivity

of the measurement. The exposed length of the coaxial cable should be made sufficiently long so that one does not need to extend it later, since additional connections will degrade the signal quality.

Becoming good at setting up anvil cells takes a lot of practice, and even experienced scientists often experience several failures per one successful attempt. Losing electrical continuity across the coil or developing a connection between the coil and the gasket upon pressurisation are rather common failure modes. They can nonetheless be rather frustrating, since the procedure of setting up an anvil cell can take up to several days. While experience is the primary attribute required for success, a good set of tools (microscope, tweezers, etc.) and optimised procedure (preparing several gaskets at a time, for instance) can significantly increase the productivity.

3.5   Muon spin relaxation spectroscopy

The transverse field μSR measurements on YFe$_2$Ge$_2$ took place at the Swiss Muon Source (SμS) facility of the Paul Scherrer Institute in Villigen, Switzerland. The experiment was conducted in the HAL-9500 instrument located on the πE3 beamline with antimuons of 28 MeV/c momentum. The instrument is designed for μSR measurements at very low temperatures and high magnetic fields. It contains a dilution refrigerator capable of reaching temperatures below 100 mK and a 9.5 T superconducting magnet. In order to avoid the deflection of the antimuons by the Lorentz force, in this instrument the magnetic field is applied along the direction of the incoming beam. In order to maintain the transverse field configuration, the spins of the antimuons, initially pointing away from the direction of travel, need to be rotated by 90°. This is achieved with the help of two devices in which the antimuons pass through a region of strong magnetic and electric fields. The magnetic field rotates the spins, while the electric field compensates for the Lorentz force. Each such device rotates the spins by 45°. Inside the sample the spins precess in the plane perpendicular to the beam. The sample stage of the instrument is surrounded by 16 positron detectors in a configuration displayed in Figure 3.9. The asymmetry is therefore measured by comparing particle counts between the pairs of diametrically opposed detectors rather than the forward and backward ones. The time interval between an antimuon entering the instrument and the resultant positron being detected is measured with the help of muon detectors in front of the sample. The flux of particles is such that at any instant there is no more than one antimuon residing in the sample. The veto detector resets the timer if an antimuon misses the sample.

The diameter of the particle beam is approximately 8 mm, therefore the sample needs to be at least that big. The antimuons entering the crystal decelerate over a distance of about 0.2 mm. This defines the minimum sample thickness. The actual YFe$_2$Ge$_2$ samples used for the measurements were 2 mm-thick discs of about 8 mm diameter.

Each run lasted until one of the positron detectors counted 500,000 particles, which took about 90 minutes. The resultant asymmetry was then fitted with the function from Equation 2.53 in order to extract the antimuon depolarisation rate and the average internal
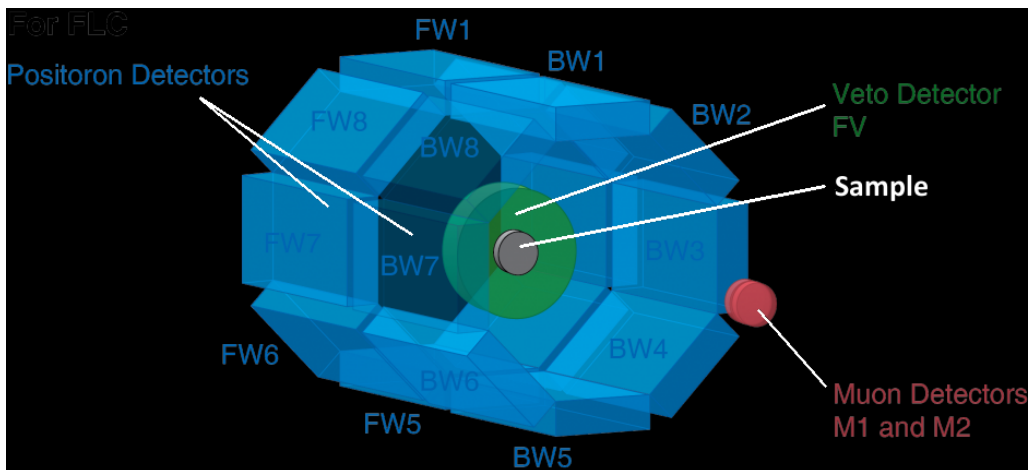
Figure 3.9: The arrangement of the positron detectors in the HAL-9500 instrument. The image was taken from the Paul Scherrer Institute web page [114].

magnetic field strength.

3.6 Tunnel diode oscillator

Despite all the advantages of quantum oscillations as an experimental technique, measuring them is often rather difficult. Even for high quality single crystals a very high precision measurement, such as capacitive torque magnetometry, is often required to resolve the oscillations. An even bigger challenge is detecting them at high pressures, when in addition to being sensitive enough the method needs to work with the constraints put on the sample space and be able to cope with the pressurisation. A technique based on the contactless skin depth measurement using a tunnel diode oscillator (TDO) satisfies these criteria.

On a very basic level, the TDO is a radio frequency LC oscillator circuit in which the oscillations are sustained with the help of a tunnel diode – a semiconductor device discovered in 1957, characterised by the IV curve displayed in the left part of Figure 3.10, with a region of negative differential resistance. The right part of the figure contains a simplified TDO circuit. Given the right parameters of components of the circuit, applying a sufficient bias voltage to the tunnel diode to bring it into the negative differential resistance regime causes a spontaneous build-up of oscillations in the circuit. In the steady state the frequency approaches the natural frequency of a damped harmonic oscillator:

$$\omega = \sqrt{\frac{1}{LC} - \frac{R_L^2}{L^2}}, \tag{3.1}$$

which has been chosen to be several hundreds of MHz in the experiments described in this thesis. Probing the sample is done by placing it inside the inductor coil. The alternating electromagnetic field decays exponentially upon entering the sample. The characteristic decay length δ is called the skin depth. For good conductors it is related to the electrical resistivity, ρ, and the magnetic permeability, μ, of the material as well as the frequency of
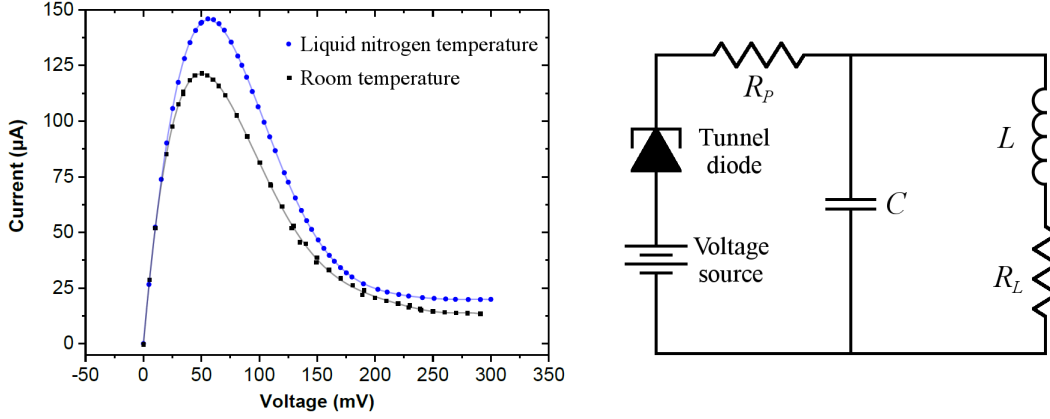
Figure 3.10: Left: an experimentally recorded IV curve of a tunnel diode [3]. At higher voltages the gradient of the curve becomes positive. Right: a basic representation of a TDO circuit. L and C are respectively the tank inductance and capacitance. R_L is the series resistance of the inductor and R_P is the resistance in series with the tunnel diode.

the external field via the expression

$$\delta = \sqrt{\frac{2\rho}{\omega\mu}}. \tag{3.2}$$

Expulsion of the alternating magnetic flux from the coil modifies its self-inductance and hence changes the oscillator's frequency, which can be measured to a very high precision with a modern frequency counter. The intrinsic stability of the TDO frequency can reach 0.001 parts per million [115], allowing one to detect very small changes in the skin depth.

Equation 3.2 implies that the skin depth is equally affected by the relative changes in resistivity and magnetic susceptibility, quantities which both exhibit quantum oscillations. Therefore it is not immediately clear how to interpret the amplitude of the TDO frequency oscillations. The question can be answered by estimating the ratio of the relative changes in these two quantities [3]. Assuming that the relative magnetic permeability of the sample is approximately equal to 1, it follows that $\Delta\mu/\mu \approx \Delta\chi$, i. e. the relative change in μ is approximately equal to the magnitude of the dHvA oscillations. The relative magnitude of the SdH oscillations can be approximated as the ratio between the oscillatory component of the density of states at the Fermi level and its static contribution. For a single spherical Fermi surface it can be shown [97] that $\Delta\rho/\rho \approx \sqrt{B/2F}$, where B is magnetic field strength and F is the frequency of quantum oscillations. Using the Equation 2.72 and assuming that the reduction factors are not much smaller than 1 (which was the case for the measurements described in this thesis):

$$\frac{\Delta\rho/\rho}{\Delta\mu/\mu} \sim \alpha \frac{B^2}{F^{5/2}} \, \mathrm{T}^{1/2}, \tag{3.3}$$

where α is a constant of the order of 1. This means that as long as $F \gg B$, the dHvA effect dominates. Since the relative change in the susceptibility due to quantum oscillations is very small, the resultant deviation of the TDO frequency is approximately linear in $\Delta\chi$. Therefore, the oscillatory component of ω is expected to have the same magnetic field and
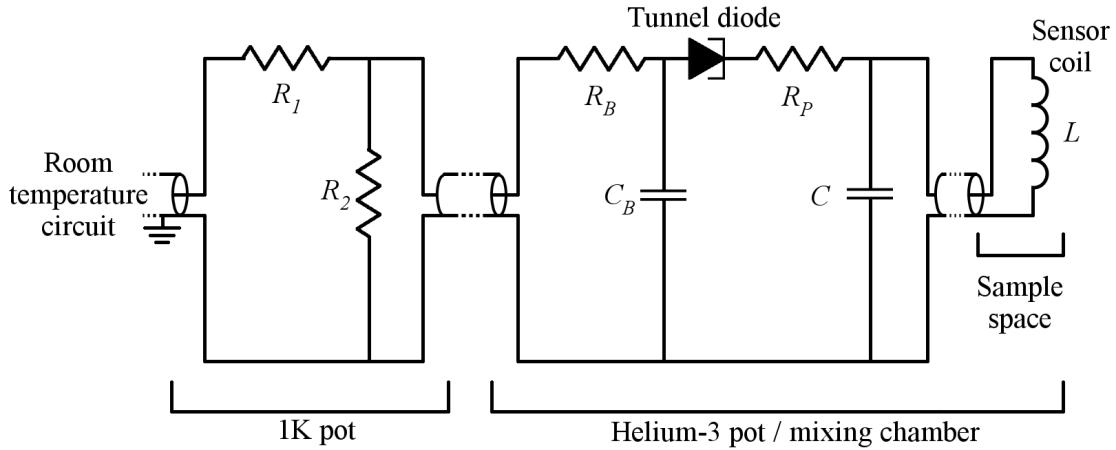
Figure 3.11: The circuit diagram of the low temperature part of the TDO circuit.

temperature dependence as the magnetic susceptibility in Equation 2.70.

Despite the effectiveness of the TDO technique, designing and optimising a working setup are rather involved tasks. A detailed quantitative description of the method is omitted here, but can be found in the PhD thesis of Hui Chang [3]. An implementation of the technique used in the Cavendish Laboratory is described below.

A typical TDO setup can be divided into two parts: the low temperature and the room temperature circuits. The low temperature circuit, presented in Figure 3.11, is mounted to the probe of a cryostat. The sensor coil, acting as the tank inductor, surrounds the sample inside a pressure cell. The inductance of the sensor coil is usually between 1 and several tens of nH. Leads coming from the coil have parasitic inductance contributing to the tank inductance and decreasing the sensitivity of the measurement. To minimise this parasitic component the coil is connected to a cryogenic copper coaxial cable. In anvil cells this connection is made at the gasket, just outside of the pressurised area. The cable needs to be short nonetheless, since it contributes parasitic resistance and capacitance. The former has a detrimental effect on the amplitude of the TDO oscillations, and the latter lowers the frequency. The other end of the cable is connected to a small board containing the tunnel diode and located in the same space as the pressure cell. The board's circuit also includes a pair of resistors R_B and R_P and a pair of capacitors C and C_B. The capacitance C and that of the coaxial cable make up the tank capacitance. The value of C can be adjusted to set the desired TDO frequency and is typically of the order of 10 pF. The resistance R_P damps the parasitic oscillations and is about 100 Ω. The rest of the low temperature circuit is related to the biasing of the tunnel diode. The parasitic inductance of the biasing circuit can negatively affect the stability of the oscillations, and in order to limit the leakage of the AC current into it the capacitance C_B is needed. Making it higher improves the stability of the TDO frequency, but weakens the signal at the detection circuit. C_B can be of the order of 1 nF, but some testing is usually needed in order to find the optimal value. The resistance R_B serves a similar purpose to C_B and is about 50 Ω. The remaining part of the low temperature circuit is a pair of resistors R_1 and R_2 which belong to a network of potential dividers used for biasing the tunnel diode. Because of
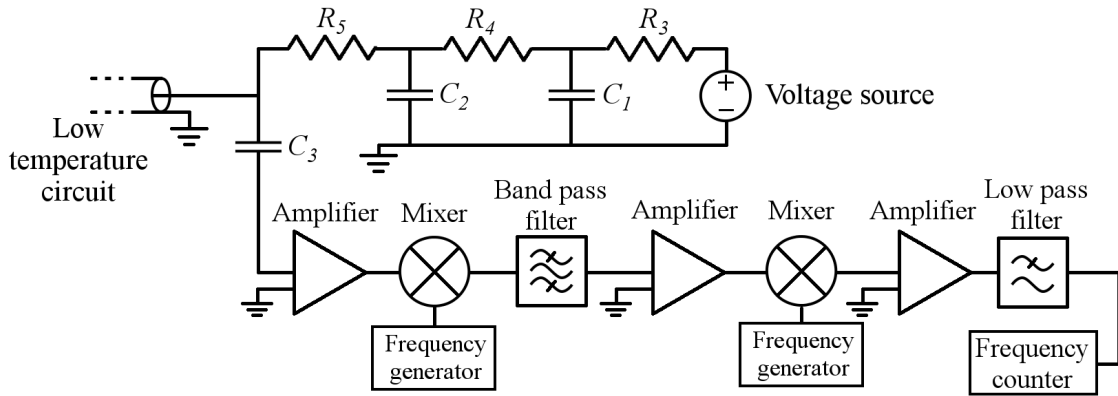
63

Figure 3.12: The circuit diagram of the room temperature part of the TDO. The lower part of the diagram displays the configuration of the detection circuit used for the measurements at the NHMFL, Tallahassee.

significant heat dissipation at these resistors a board with them is placed at the 1K pot level of the probe and is connected to the tunnel diode board with a cryogenic stainless steel coaxial cable. Steel is chosen instead of copper due to a lower thermal conductivity, reducing the heat leak. The signal is carried to the top of the probe through another segment of stainless steel coaxial cable.

The room temperature part of the TDO, shown in Figure 3.12, contains the rest of the biasing circuit and a detection circuit. The voltage source provides the bias voltage and the resistors R_3, R_4 and R_5 are used for dividing the potential. The capacitors C_1 and C_2 act as the low-pass filters for the voltage source. Capacitor C_3 transmits only the AC component to the detection circuit. This circuit serves the purpose of amplifying the signal and filtering the noise out of it. These is a degree of flexibility to how exactly this is accomplished. The variant of the detection setup displayed in Figure 3.12 was used for the measurements at the NHMFL. The amplifiers, filters and mixers have been acquired from Mini-Circuits. The amplification is necessary because the raw signal is typically too weak to trigger the frequency counter. ZFL-1000LN+ or ZFL-500LN+ amplifiers of +24 dB gain have been used for this purpose. Filtering is required to clean up the signal. Band-pass filters generally have narrower bandwidths at lower frequencies, therefore it is useful to reduce the frequency of the signal down to tens of MHz using a mixer and a local oscillator (frequency generator). Additional stages of amplification, mixing and filtering can be added in order to further improve the strength and quality of the signal. In the example illustrated in Figure 3.12 the second mixer reduces the frequency to below 10 MHz and a low pass filter removes the higher frequency components.

For the measurements in the superconducting magnet at the NHMFL the TDO circuit had the following parameters: $R_1 = 60\,\Omega$, $R_2 = 205\,\Omega$, $R_3 = 1\,\mathrm{k\Omega}$, $R_5 = 1.8\,\mathrm{k\Omega}$, $R_B = 51\,\Omega$, $R_P = 102\,\Omega$, $C_1 = 110\,\mathrm{nF}$, $C_2 = 110\,\mathrm{nF}$, $C_3 = 1\,\mathrm{nF}$, $C_B = 1\,\mathrm{nF}$ and $C = 12\,\mathrm{pF}$. The resistance R_4 was between 1 and 10 kΩ and the inductance of the sensor coil was approximately 20 nH. The voltage source was set to output approximately 10 V.

The setup developed in the Cavendish Laboratory uses germanium tunnel diodes supplied by MACOM, such as MDB2057-E28 or MDB4057-E28 . The two variants have different current ratings, of 200 µA and 400 µA respectively. Diodes with lower current rating produce less heat, but generate oscillations for a narrower window of parameters. Higher current rating is therefore preferred for experiments at user facilities, when time for tuning the TDO is limited. Tunnel diodes are not widely used these days and are not produced in large quantities. As a consequence, they are rather expensive, costing tens of pounds per unit. When soldering a diode to a circuit board the heat should be applied in short intervals of no longer than a couple of seconds, since it is possible to damage the component by overheating it. Electrostatic discharge is another source of damage, therefore when the TDO is not in use it is recommended to temporarily short-circuit the tunnel diode board.

Tunnel diodes of the same nominal parameters, even from the same batch, usually have slightly different IV curves. For this reason, when a new TDO circuit is built or the tunnel diode in the existing one is replaced some diagnostics and optimisation are often necessary. In order to ensure that the diode is not faulty it is useful to test the circuit at the room temperature. Once the circuit is assembled and powered up, the tunnel diode needs to be tuned into the right regime by setting the appropriate bias voltage. For the particular setup described above the voltage provided by the power supply should be between 7 and 15 V. The oscillations are more likely to appear at room temperature if the sensor coil is temporarily replaced with a coil of much larger inductance, for instance 1 µH. Once it is established that the tunnel diode works well, its low temperature performance can be tested by immersing the diode and the coil into liquid nitrogen. A change in the IV curve of the diode and a decrease of resistances of the nearby wires associated with the cooling make the oscillations more likely to appear for a given set of TDO components. For this test it is advised not to use the actual sensor coil with the pressure cell, because rapid cooling can lead to its malfunction. A dummy coil of similar parameters can be connected instead. If the signal is too weak even at low temperature the capacitance C_B can be reduced. The frequency is adjusted by changing the capacitance C. The TDO frequency typically has a parabolic dependence on the bias voltage, and the oscillations are usually the most stable at the extremum as a result of the lowest sensitivity of the former to the latter.

The TDO frequency is sensitive to any changes within the circuit. Even the smallest vibrations of wires can result in significant noise. It is therefore important to ensure that every part of the low temperature circuit, including the cables, is securely attached to the cryostat probe. To reduce the influence of the electromagnetic background it may be useful to shield some parts of the room temperature circuit with metallic foil. It is also advised to use coaxial SMA connectors instead of BNC ones for connecting different parts of the detection circuit, as the former design produces tighter connections. The TDO frequency can sometimes repeatedly undergo sudden changes. This could indicate that the circuit switches between several configurations none of which is stable enough. Gently tapping the probe with a hard object can help to relax some parts of the circuit into more

stable states and eliminate the jumps. It is also characteristic for the TDO frequency to drift with time. For a well-working setup the drift is monotonic, and can be removed from the signal with the background subtraction procedure.

When conducting measurements with the TDO at dilution refrigerator temperatures one must keep in mind that the sensor coil heats the sample up both inductively and due to its own resistive heating. It has been estimated [3] that the lower bound of the temperature difference between the sample and the anvils of the pressure cell is about 9 mK. The tunnel diode itself also generates a considerable amount of heat. Below 100 mK powering up the TDO can increase the temperature reading of a mixing chamber thermometer by several tens of mK.

4 Study of YFe$_2$Ge$_2$

4.1 Production of the compound

The study of YFe$_2$Ge$_2$ has been an ongoing project in the Quantum Matter group of the Cavendish Laboratory for several generations of PhD students, starting with the work of Zhuo Feng in 2009. Throughout this time plenty of effort has been put into refining the procedure of the crystal growth in order to improve the quality of samples. Naturally, a lot of knowledge about the YFe$_2$Ge$_2$ growth process has been accumulated over the years, and nowadays there are a lot of nuances associated with it. Almost all of the samples obtained over the past few years have been grown by a current PhD student Jiasheng Chen, and his future thesis is expected to contain the most comprehensive account of the YFe$_2$Ge$_2$ production. This section of the dissertation contains a brief overview of how the YFe$_2$Ge$_2$ growth process evolved in the Quantum Matter group. The approach used for obtaining the highest quality samples to date will also be described.

Early attempts to grow single crystals of YFe$_2$Ge$_2$ using the flux method resulted in only a fraction of samples showing the resistive signature of superconductivity, and none of them displayed the superconducting anomaly in the heat capacity. Polycrystalline material grown in the radio frequency (RF) induction furnace was generally much better, with almost all samples showing a resistive T_c of about 1 K, given residual resistance ratios (RRR) of at least 15. Even to this day polycrystalline YFe$_2$Ge$_2$ consistently shows higher T_c and RRR than its flux grown counterpart, and there is no clear explanation for such an improvement. It is possible that faster cooling of ingots in the RF furnace helps to quench the material in a more homogeneous state than after a slow cooldown during the flux growth. Nevertheless, heat capacity measurements performed on the early generations of samples grown with the induction melting method still showed no anomaly. Its absence raised concerns about whether the observed superconductivity was indeed an intrinsic property of YFe$_2$Ge$_2$ or was instead caused by some alien phase. Annealing the ingots after the growth resulted in the next breakthrough. The T_c went up to 1.8 K and RRR increased by more than an order of magnitude. Samples with RRR greater than 60 consistently showed the signature of superconductivity in the heat capacity. Tuning the composition of the compound revealed that growing YFe$_2$Ge$_2$ with a nominal 5% excess of iron results in the highest quality samples, pushing RRR to above 200. While it is surprising that growing the material in a seemingly more disordered configuration gives better results, this can be explained by the presence of some iron rich alien phases (they will be described in more detail later). These alien phases form even for nominally stoichiometric compositions, and possibly deplete the main phase of iron. Thus, adding extra iron may compensate for this depletion, making the main phase more ordered.

The quality of the starting materials also plays an important role. For instance, one of the improvements came from switching to a higher purity vacuum remelted iron. Properties of the final compound have even been noticed to vary between different batches of yttrium of the same nominal purity, due to some changes in the purification process at the supplier's end. Given such sensitivity to impurities, it goes without saying
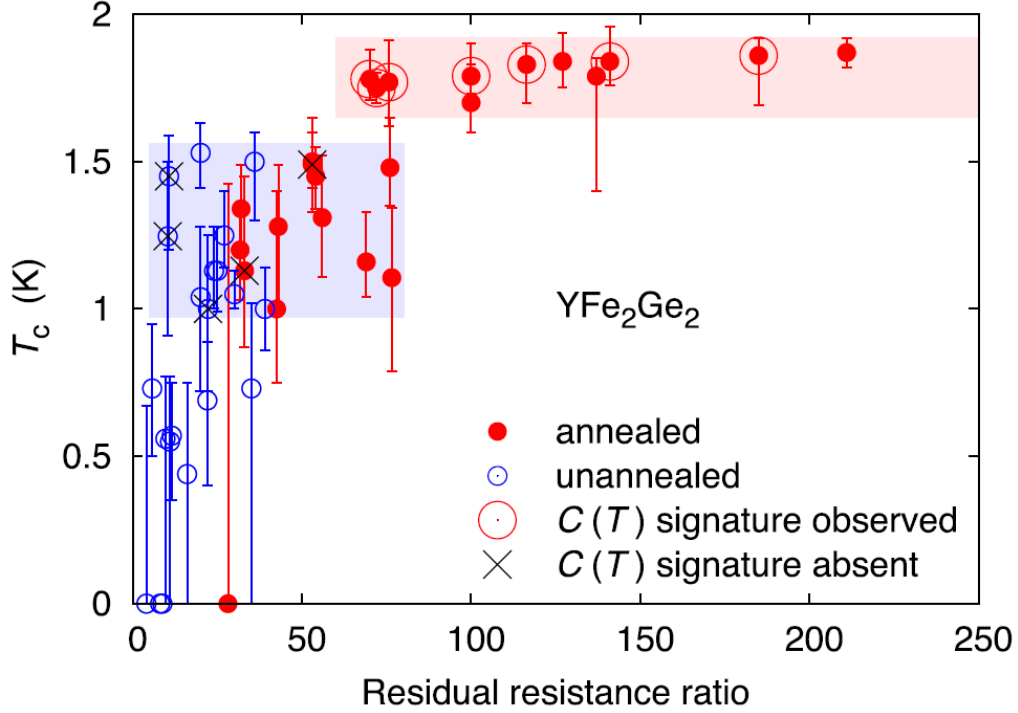
Figure 4.1: Transition temperatures and residual resistivity ratios of various generations of YFe$_2$Ge$_2$ samples [40]. Red circles and black crosses mark the samples, heat capacity of which was measured and the superconducting anomaly respectively was or was not observed.

that all reactants must be handled carefully in order to limit their contamination.

The best YFe$_2$Ge$_2$ samples obtained so far have been grown in the RF induction furnace in an atmosphere of argon. The production cycle started with the raw elements. Yttrium pieces (3N pure, accounting for the rare earth metal impurities only), vacuum remelted iron lumps (4N) and germanium pieces (6N) obtained from Alfa Aesar were used as the starting materials. The total mass of the reactants was usually around 5 grams. In order to prevent the formation of stable iron-germanium phases, the first stage of the growth was a pre-reaction of yttrium and iron in a 1:2 atomic ratio, resulting in a YFe$_2$ ingot. Weight of the ingot was measured and the necessary amounts of germanium and iron in order to achieve the target nominal composition (5% iron rich) were added for the second stage of the growth. The resultant ingot had a melting point of slightly above 1300 °C. The mixture was maintained in the molten state for several minutes until all the ingredients were well mixed. The RF power was then cut off. This quenched the melt, making it solidify in less than a second.

The annealing routine consisted of two parts. First, a freshly produced YFe$_2$Ge$_2$ ingot was kept in the induction furnace at 1250 °C for one hour. Afterwards the ingot was sealed inside an argon filled quartz ampoule and annealed in a box furnace at 800 °C for 7-8 days.

The results of many iterations of YFe$_2$Ge$_2$ growth over the years are summarised in Figure 4.1. Batches produced before the annealing at 800°C was introduced are represented with the blue circles, while the red filled circles stand for the annealed

samples. Error bars indicate 20% and 80% resistivity suppression thresholds. Unannealed samples generally had RRR below 40 and very variable T_c, without always showing a full resistive transition. Heat capacity measurements were performed on some samples but none of them displayed the superconducting anomaly. These samples are marked with the black crosses. Early annealed samples, contained within the area shaded with grey, were generally purer, with RRR between 40 and 80, had more stable T_c of about 1.3 K and showed full resistive transitions. The area shaded with red includes samples from the latest generations of growths. Their RRR started at 60 and extended to above 200. There was an obvious increase in the T_c to about 1.8 K. These latest batches reliably showed the anomaly in the heat capacity (tested samples are marked with the red circles). Overall, there was an obvious correlation between RRR and T_c. Such sensitivity to disorder and impurities is characteristic for unconventional superconductors [116].

The final polycrystalline ingots had an oxide-covered dark grey surface, but when broken revealed a shiny silver-coloured metal. On a scale larger than a millimeter the texture was rather non-uniform. Crushing the ingot into smaller pieces resulted in fairly homogeneous looking grains, which often had flat faces of area sometimes reaching several square millimeters. Pieces with such faces often had a layered structure. Coupling between the layers was quite strong, but using a sharp scalpel it was sometimes possible to cleave the material along the planes parallel to the faces.

The nomenclature for labelling the samples includes the growth method followed by the ingot number, ingot part, and the sample number. For example, RF34B02 stands for the sample number 2 from part B of the ingot number 34 produced in the RF induction furnace.

4.2 Crystallographic characterisation

4.2.1 Powder x-ray diffraction

Powder X-ray diffraction measurements were conducted in the Earth Sciences department of the University of Cambridge with the help of Dr Giulio Lampronti. The data were collected in Bragg-Brentano geometry on a D8 Bruker diffractometer equipped with a primary Ge monochromator for Cu K$_{\alpha 1}$ x-rays and a Sol-X solid state detector to reduce the effects of Fe fluorescence. Figure 4.2 shows a pattern obtained for the RF34B batch of the nominal composition YFe$_{2.1}$Ge$_2$. Collection conditions were: 5–100° in 2θ, 0.03° step size, 10 seconds/step, 0.1 mm divergence slits, 0.2 mm receiving slit, sample spinning. Rietveld refinements were performed with the software Topas 4.1. A spherical harmonic model was applied to correct for preferred orientation of YFe$_2$Ge$_2$ within the powder. No structural parameter was refined when resolving the phase content. A shifted Chebyshev function with six parameters was used to fit the background. Peak shapes of all phases were modelled using Pseudo-Voigt functions. Rietveld refinement of the data obtained from the highest quality samples yielded 98.7% of YFe$_2$Ge$_2$ (lattice parameters $a = 3.963$ Å, $c = 10.457$ Å); 1.2% of Fe$_{0.85}$Ge$_{0.15}$, a bcc iron-germanium alloy ($a = 2.885$ Å); 0.1% of iron ($a = 3.04$ Å) and traces of FeGe$_2$ at less than 0.01%. Crystal structures of all
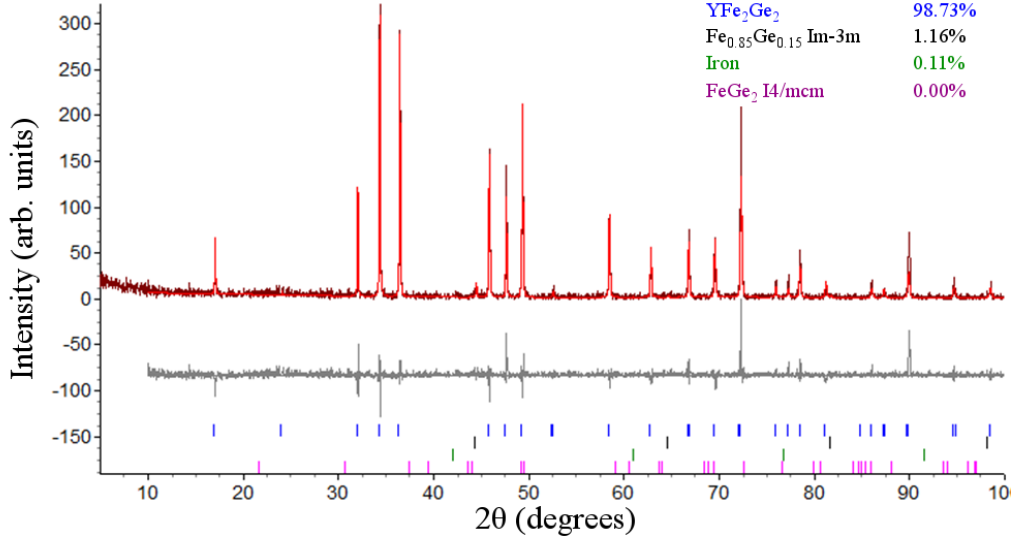
Figure 4.2: Powder X-ray data for the RF34B batch with the nominal composition YFe$_{2.1}$Ge$_2$ [40] (supplementary information).

phases were retrieved from the inorganic crystal structure database: YFe$_2$Ge$_2$ ($I4/mmm$, ICSD reference code: 81745); Fe$_{0.85}$Ge$_{0.15}$ (Im-$3m$, 103493); Fe (Im-$3m$, 64795); FeGe$_2$ ($I4/mcm$; 42519). Matching the observed phase content to the nominal composition used in this growth, YFe$_{2.1}$Ge$_2$, allowed to estimate the sample composition as YFe$_{2+x}$Ge$_2$ with $0 < x < 0.03$, depending on the precise Fe content in the bcc iron-germanium alloy. Overall, across different batches the samples were 97.5%–99.5% phase pure. The dominant impurity phase Fe$_{0.85}$Ge$_{0.15}$ is a ferromagnetic alloy with the Curie temperature of about 700°C [117].

4.2.2 Single crystal Laue x-ray diffraction

Pieces of YFe$_2$Ge$_2$ obtained by crushing an ingot usually had flat faces, sometimes reaching a few square millimeters in area. To test whether these faces were monocrystalline surfaces a backscattering Laue x-ray diffraction measurement has been conducted using a Polaroid film camera. Figure 4.3 shows one of the obtained images. For all successful exposures a four-fold symmetric pattern could be distinguished. The symmetry was consistent with the tetragonal lattice viewed along the *c* axis. This confirms that YFe$_2$Ge$_2$ tends to cleave along the *ab* plane of the lattice.

Figure 4.3: Single crystal Laue diffraction image obtained from the surface of a YFe$_2$Ge$_2$ piece.

4.3 Fermi surface calculations

In-house density functional theory (DFT) calculations were performed in Wien2K software by Pascal Reiss. The predicted Fermi surface structure of YFe$_2$Ge$_2$ is displayed in Figure 4.4 and is consistent with the earlier theoretical predictions [39, 37]. The biggest Fermi surface is a hole pocket that can be can be approximated as an ellipsoid of 2 Å^{-1} diameter and 0.8 Å^{-1} height. Calculations were also performed for different structures of KFe$_2$As$_2$: ambient pressure uncollapsed tetragonal and high pressure collapsed tetragonal. Their results are also shown in the figure. Apart from the region close to the Γ point there is an apparent similarity between the Fermi surface structures of YFe$_2$Ge$_2$ and collapsed tetragonal KFe$_2$As$_2$, which suggests that YFe$_2$Ge$_2$ can be thought of as an ambient pressure equivalent of the high pressure KFe$_2$As$_2$. A remarkable fact, already mentioned in the introduction, is that the structural transition in KFe$_2$As$_2$ almost triples the superconducting T_c [29]. The proximity to the same kind of structural instability could be important for superconductivity in YFe$_2$Ge$_2$, and the compound can potentially act as a clean and easily probeable system for studying this phenomenon.
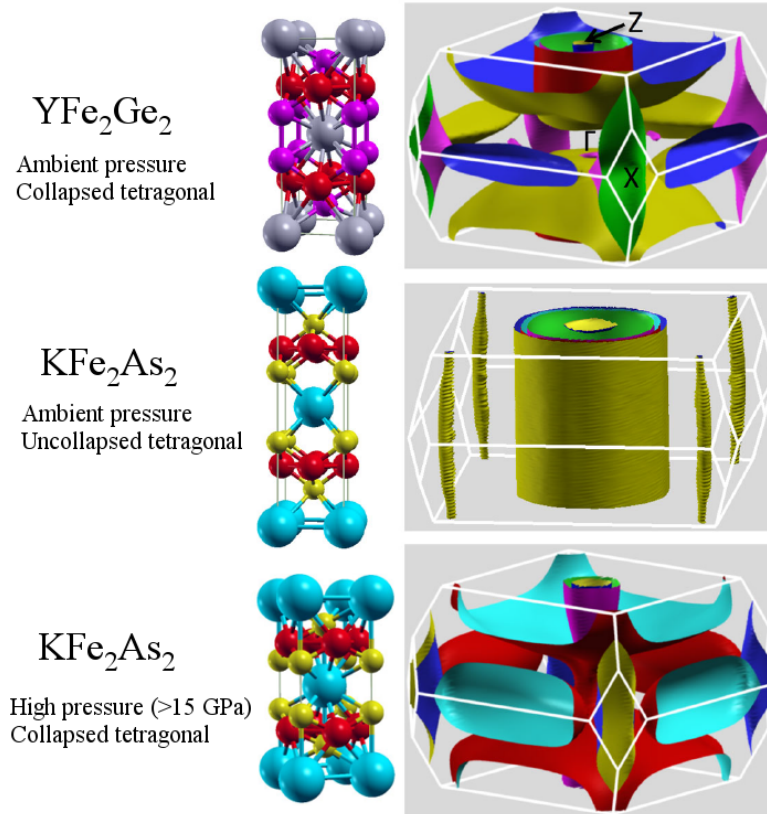
Figure 4.4: Fermi surfaces calculated using DFT for the ambient pressure YFe$_2$Ge$_2$ and KFe$_2$As$_2$ structures as well as the high pressure collapsed tetragonal structure of KFe$_2$As$_2$ [40].

4.4 Electrical resistivity

Electrical resistivity was measured using the standard four terminal AC technique either in the PPMS or in the DMS-1000 cryostats. For making samples polycrystalline ingots were shattered into pieces not exceeding several millimeters in size. The samples which appeared to contain large monocrystalline fractions were chosen for the measurements. Sample shape was typically rather irregular, which made it hard to accurately measure the cross-sectional area and the separation between the voltage leads in order to convert resistance to resistivity. The latter was therefore obtained by setting the resistivity to 190 μΩ cm at 300 K according to the published result [31], and scaling the rest accordingly.

The excitation voltage was chosen to be rather small in order to not affect the T_c significantly by the flow of current. For the larger samples (of the order of 1 mm in length, several hundred microns in width and thickness) 1 mA current was used. The smallest samples, for high pressure measurements inside the anvil cell, required currents as low as 0.1 mA. Averaging time varied between 1 and 3 seconds based on the noise level.

At these currents there was usually a noticeable noise in the data. If the density of recorded points was high enough, the data was smoothed during the analysis by locally fitting a low order polynomial to a moving temperature window. As a result of that, the markers in the graphs do not necessarily correspond to the originally recorded values. The transition temperature was defined as the temperature at which the resistance was
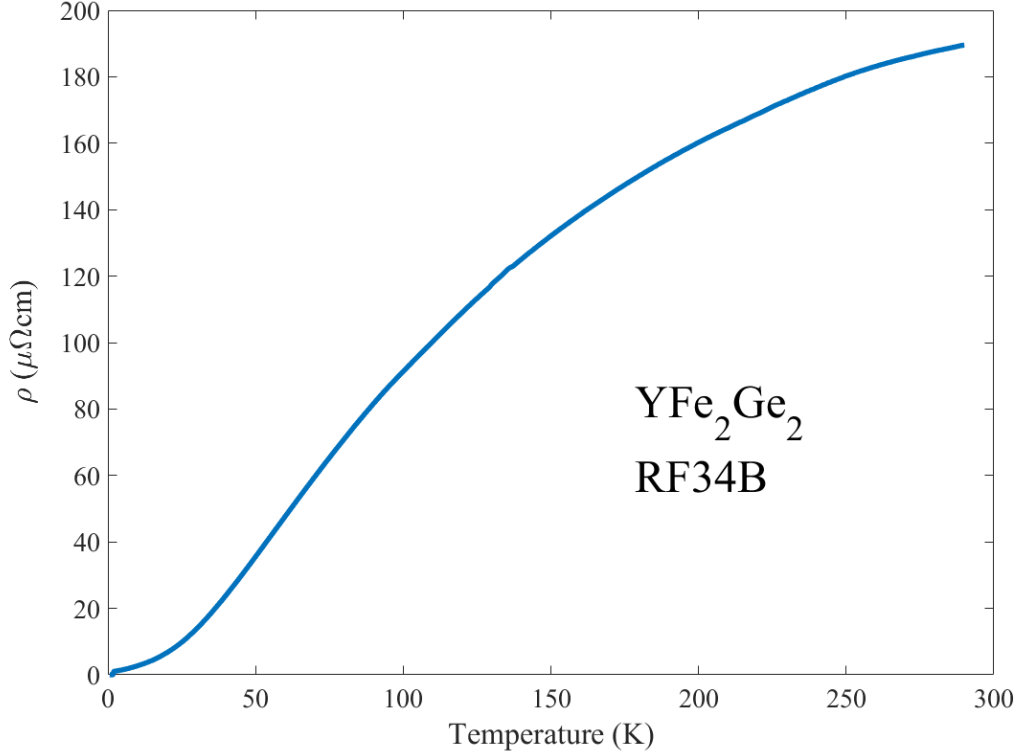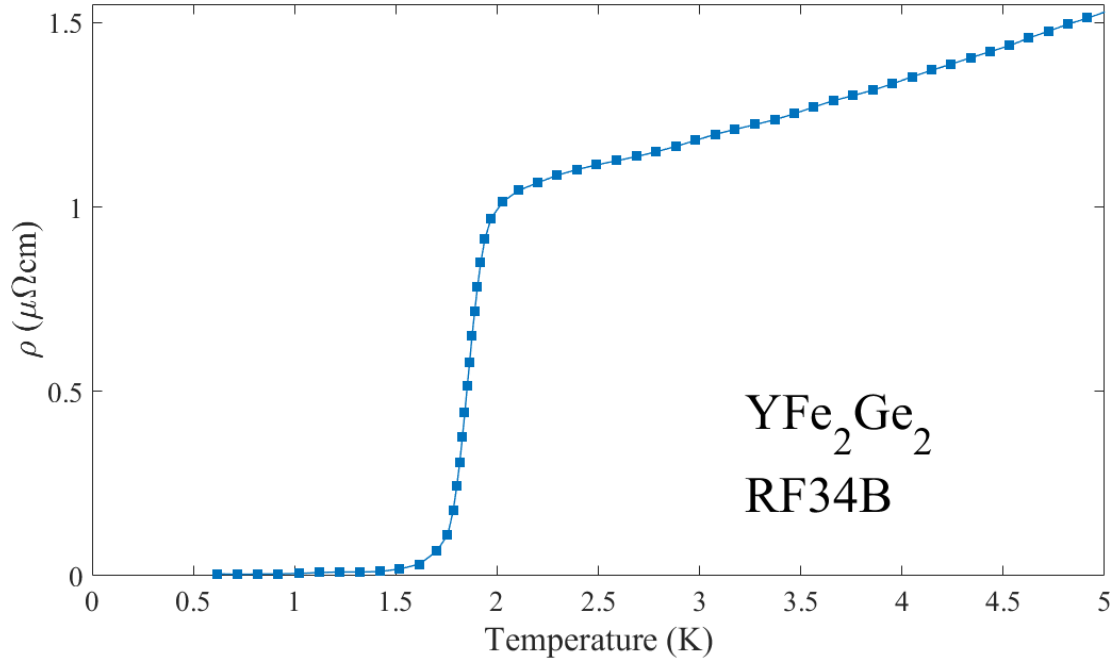
Figure 4.5: Electrical resistivity of YFe$_2$Ge$_2$ as a function of temperature across the full range.

suppressed to half of the extrapolated normal state resistance (extrapolation assumed a power law dependence on temperature). Error bars indicate the transition width using 20% and 80% resistivity suppression thresholds, unless other criteria are specified.

4.4.1 Ambient pressure measurements

Samples from the RF34B batch showed the best performance in terms of T_c and RRR. Plot of resistivity, ρ, against temperature for the RF34B02 sample is displayed in Figure 4.5. The resistivity of YFe$_2$Ge$_2$ shows the typical metallic temperature dependence.

Figure 4.6 shows the low temperature behaviour of the resistivity for the same sample. The superconductivity set in at the critical temperature of 1.87 ± 0.05 K. Stability of the temperature and voltage readings was not good enough for a detailed study of the temperature exponent of resistivity. Fitting a power law dependence of the form $\rho(T){=}\rho_0{+}AT^x$ using the method of least squares to several temperature intervals starting at 2.5 K and ending between 5 K and 10 K gave $x = 1.48 \pm 0.05$, consistent with the previously detected non-Fermi liquid behaviour [35]. Extrapolating the power law to zero temperature resulted in the residual resistivity $\rho_0 = 0.90$ μΩ cm. RRR for this sample was therefore equal to 211. The low temperature mean free path can be estimated using the Equation 2.23. According to the previously mentioned approximation for the dominant hole Fermi pocket, its surface area is about 8.2 Å^{-2}, and the mean free path for the highest quality samples is therefore predicted to be of the order of 2000 Å.

Figure 4.6: Electrical resistivity of YFe$_2$Ge$_2$ at low temperatures.

Batch name	Nominal composition	Highest measured RRR	Highest measured T_c (K), 50% level in resistivity
RF32B	YFe$_{2.2}$Ge$_2$	142	1.83
RF34B	YFe$_{2.1}$Ge$_2$	211	1.87
RF72A	YFe$_2$Ge$_2$	60	1.5
RF73A	YFe$_{2.1}$Ge$_2$	150	1.7

Table 4.1: Table of some basic properties of different batches of YFe$_2$Ge$_2$ mentioned in this thesis.

Most of the measurements described in this chapter were conducted using samples from the RF34B batch, since they had the best quality. Samples from several other growths were also used in the study aside from initial characterisation. Table 4.1 summarises some basic properties all YFe$_2$Ge$_2$ batches mentioned in this chapter.

In order to find a good sample for resistivity measurements inside the moissanite anvil cell about 40 samples from RF32B and RF73A batches were tested at ambient pressure. These had to be small samples, not exceeding 250 µm in length and 50 µm in thickness. It turned out that T_c of these samples was on average lower than of the bigger ones, and that it varied across the range between about 1.2 K and 1.8 K. Some transitions were rather asymmetric or had kinks in them, like in the example shown in Figure 4.7. This could indicate that on a scale of about 100 µm the samples were composed of multiple different regions comparable in size to the sample itself. If the samples were simply inhomogeneous, the transition would appear smeared out. But in the Figure 4.7 the jump in resistivity is not just broadened, but has a kink at 1.65 K, which can be explained by assuming that two distinct regions were probed within the sample, with each region also being somewhat inhomogeneous. One on average had a higher T_c and spanned the majority of
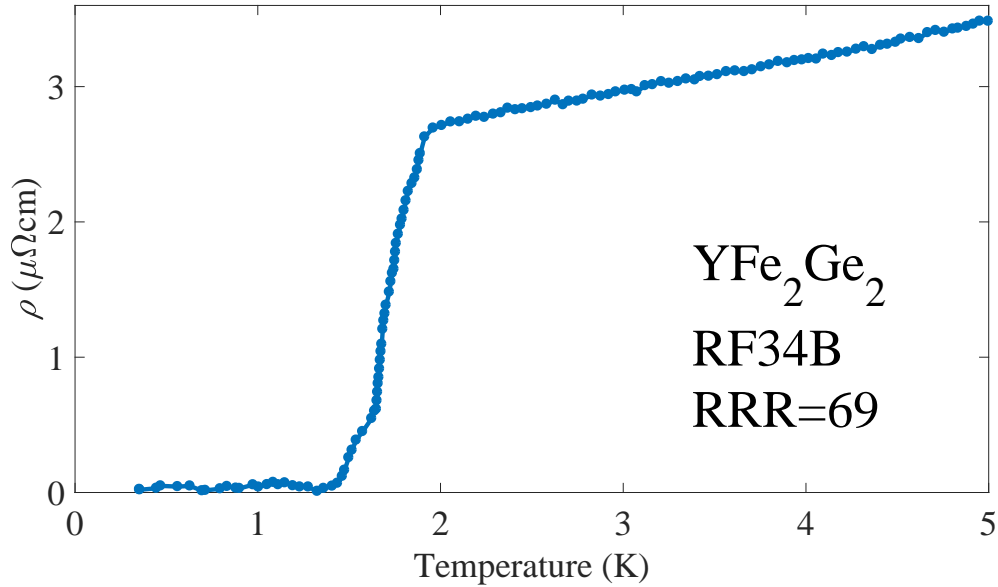
74

Figure 4.7: Superconducting transition of a small YFe$_2$Ge$_2$ sample from the RF34B batch. The transition has a kink, indicating that the sample contains parts with distinctly different properties.
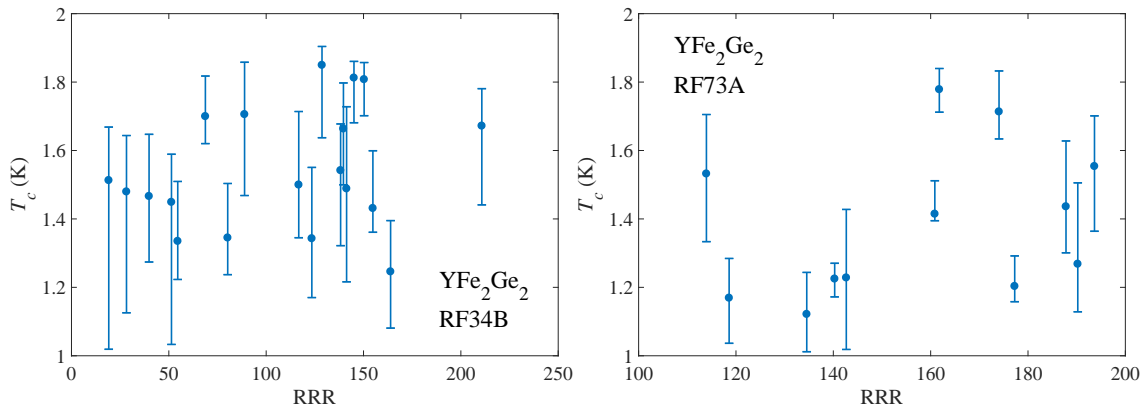

Figure 4.8: RRR and transition temperatures of small YFe$_2$Ge$_2$ samples from RF34B and RF37A batches.

the current path. At 1.65 K that region was fully superconducting, but about 20% of the current path went through another, more inhomogeneous region, properties of which were on average different from those of the first one. Upon further temperature decrease only the changes within the second region affected resistivity until at 1.4 K the entire current path finally became superconducting. During resistivity measurements it is often unclear what fraction of a sample is actually probed, and the reading is predominantly determined by the most conducting parts of the sample. Initial characterisations of freshly produced batches of YFe$_2$Ge$_2$ were typically conducted on fairly big samples and the results most likely represented only relatively small fractions of the samples, but at the same time the ones of the highest quality.

Results of the screenings are displayed in Figure 4.8. RRR and T_c do not appear to be correlated within the same YFe$_2$Ge$_2$ batch.
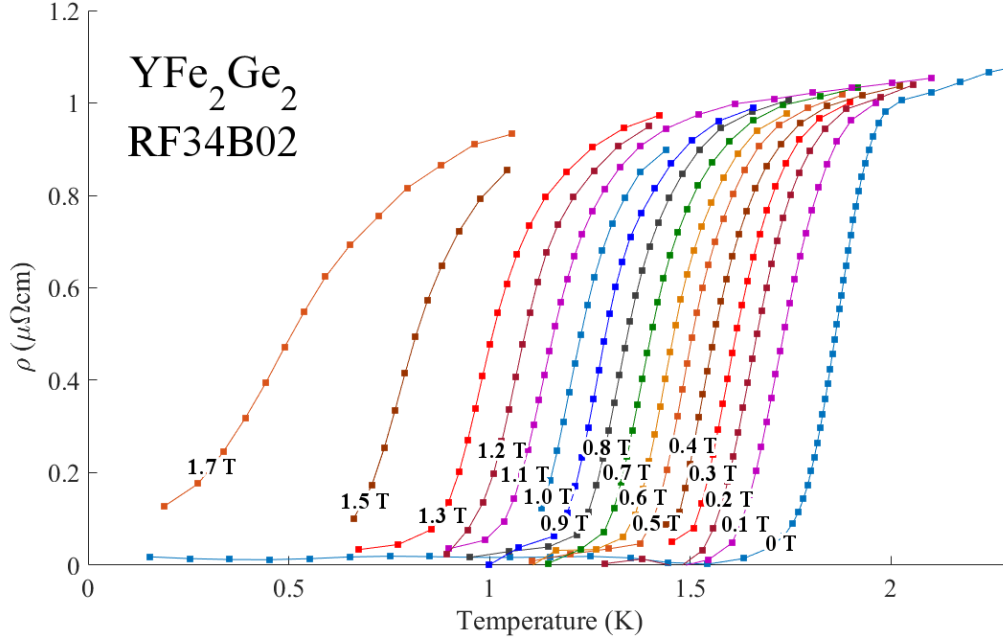
Figure 4.9: Resistivity of YFe$_2$Ge$_2$ against temperature at different magnetic fields.

4.4.2 Resistivity in magnetic field.

The influence of magnetic field on superconductivity in YFe$_2$Ge$_2$ was studied in the DMS-1000 cryostat. Temperature was swept across the transition at different magnetic fields. Just above the transition temperature the compound had a weak positive magnetoresistance of about 2% per Tesla. In Figure 4.9 resistivity of the RF34B02 sample is plotted against temperature for different magnetic fields. T_c was suppressed by the field in the manner characteristic for a type II superconductor . The transition also broadened above 1 T, which could be explained by differently oriented polycrystalline grains within the sample having slightly different reactions to the magnetic field due to the anisotropy of the lattice.

The upper critical field curve is plotted in Figure 4.10. From a visual extrapolation the zero temperature limit of the upper critical field was approximately 2 T. According to the Equation 2.40 this corresponds to a coherence length $\xi_0 \approx 130$ Å. This is significantly smaller than the mean free path estimated above, therefore the clean limit should be rather appropriate for the orbital limited upper critical field calculation. From the Equation 2.41 the orbital limited upper critical field is predicted to be 2.4 T, which clearly exceeds the experimentally predicted value by a small amount. Zero field values of the critical temperature deviated from the linear trend established in the low field region. This could happen due to an alignment of magnetic moments of the ferromagnetic inclusions as the field was applied, which slightly amplified the magnetic field inside the sample . One of the zero field points, the one with the slightly lower T_c, was recorded at the end of the measurement, when the sample probably had a remanent magnetisation.
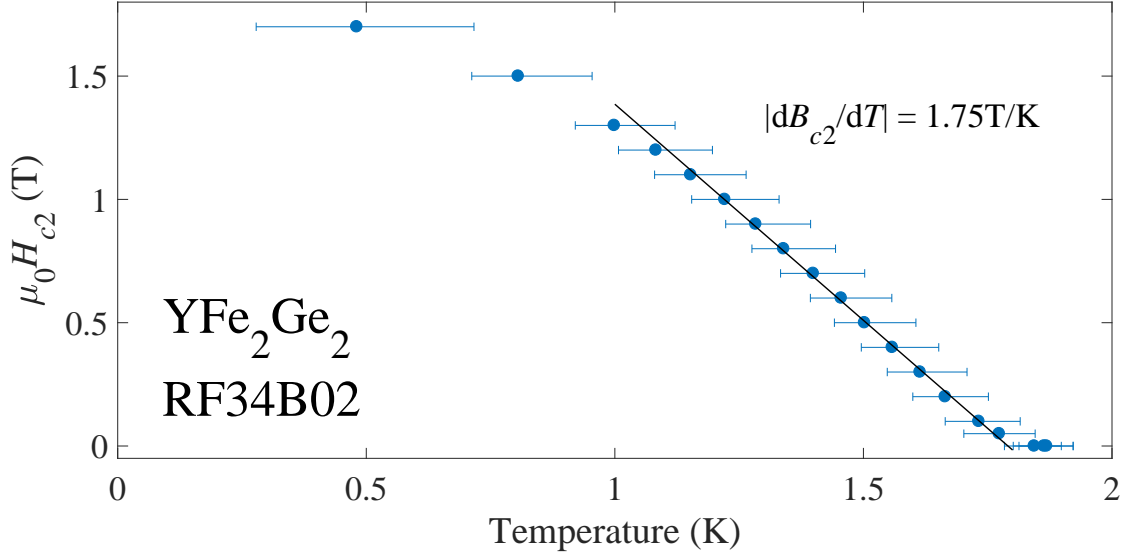
Figure 4.10: Upper critical field of YFe$_2$Ge$_2$as a function of temperature. Black line shows the slope of the curve at low fields.

4.4.3 High pressure measurements

Measurements of electrical resistance under high pressure were first conducted on the RF34B02 sample inside a piston-cylinder cell. Daphne 7373 oil was used as the pressure transmitting medium. It is important to note that at room temperature this oil starts solidifying at about 22 kbar [118], which is well below the maximum pressure achieved with the type of piston-cylinder cell used. If the pressure medium becomes solid while the load is increased there exists a high chance of introducing inhomogeneous stresses in the sample space. In order to avoid that, when working at pressures above about 15 kbar, the pressure cell was warmed to about 60-70°C before and after the application of force. During the measurements the thermal lag was accounted for by using equal sweep rates for cooling down and warming up the cell. The respective temperature readings corresponding to the same sample resistance were averaged. Additionally, below 4 K the rate of change of temperature was kept around 0.02 K/min, which reduced the lag to no more than 20 mK.

Figure 4.11 shows the low temperature resistivity at different pressures. Measurements were performed at five pressures starting with the cell just sealed at 1.3 kbar and going up to 27.2 kbar. Assuming that the bulk modulus of YFe$_2$Ge$_2$ is around 100 GPa (based on the bulk moduli of similar collapsed tetragonal structures [119, 120]), volume reduction alone at 30 kbar should only result in about a 1% change of resistance. Change in the sample geometry was therefore neglected when converting resistance to resistivity. The transition is incomplete at 1.3 kbar, because of hitting the lowest temperature the PPMS cryostat could maintain. The uncertainty in pressure was calculated from the width of the superconducting transition of tin and was found to be around ±1 kbar at most.

As can be seen in Figure 4.13, application of pressure in the piston-cylinder cell barely affected the superconductivity. The midpoint of the transition monotonically increased over the covered pressure range, reaching 2.08 K at 27.2 kbar, compared to 1.87 K at ambient pressure. The most pronounced change happened between the lowest two pressure
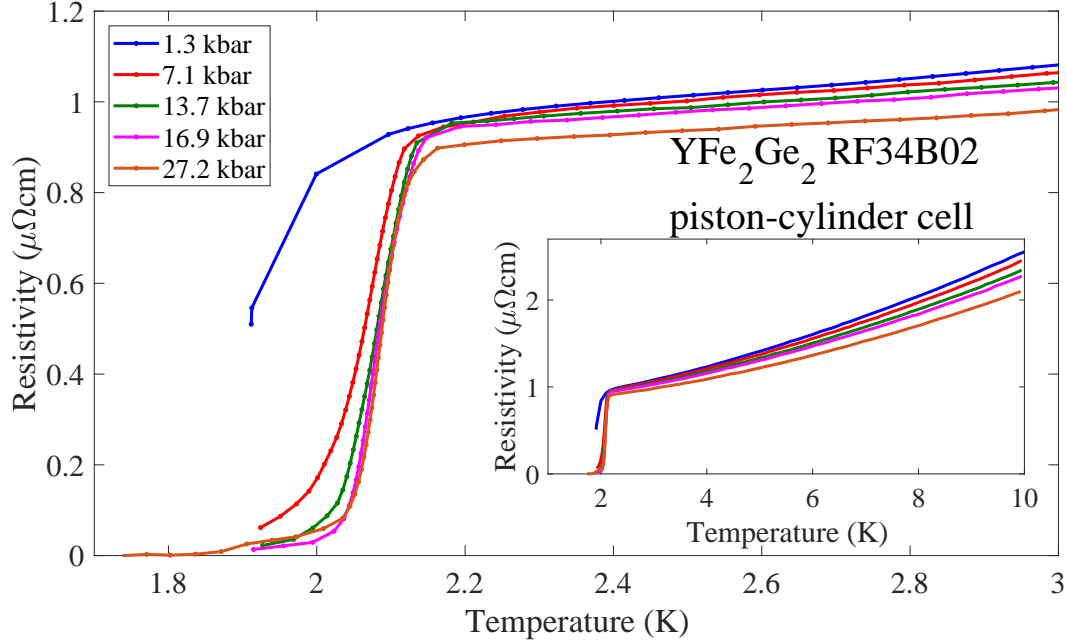
Figure 4.11: Resistivity as a function of temperature for YFe$_2$Ge$_2$ inside a piston-cylinder cell. The inset includes a wider range of temperatures.

points: 1.3 kbar and 7.1 kbar. The interval between these two pressures could benefit from a few intermediate pressure points. While increasing pressure typically results in reduced homogeneity, for the piston-cylinder cell data presented here the width of the transition became narrower at higher pressures. It is possible that heating up the cell in order to increase the solidification pressure of the medium resulted in improved hydrostaticity compared to lower pressures. From the data at 27.2 kbar it can also be seen that at 2 K an almost fully superconducting channel was formed in the sample, but there was still a section of the current path which remained in the normal state down to about 1.9 K.

No signatures of antiferromagnetic ordering were detected, and from the change in T_c alone it is impossible to tell whether pressure drives the system towards a QCP. On the other hand, the A coefficient of the resistivity went down with pressure, decreasing steadily roughly by a factor of 3 across the studied range. This is contrary to what is expected for approaching a QCP, since the effective quasiparticle mass increases close to a QCP, and the resultant increase in the Sommerfeld coefficient γ should also affect the A coefficient through the Kadowaki-Woods ratio (in a qualitative sense, since the Kadowaki-Woods ratio is, strictly speaking, defined only for a T^2 dependence of resistivity). In addition to that, the temperature exponent increases from 1.5 to 1.78 (according to a power law fit between 2 K and 10 K), i. e. came closer to the Fermi liquid value of 2. The latter two arguments implied that hydrostatic pressure actually tuned the system away from the QCP.

In order to extend the phase diagram to higher pressures the same experiment was conducted in a moissanite anvil cell on a different sample from the RF34B batch with RRR of 130. Pentane-isopentane 1:1 mixture was used as the pressure medium. Plots of
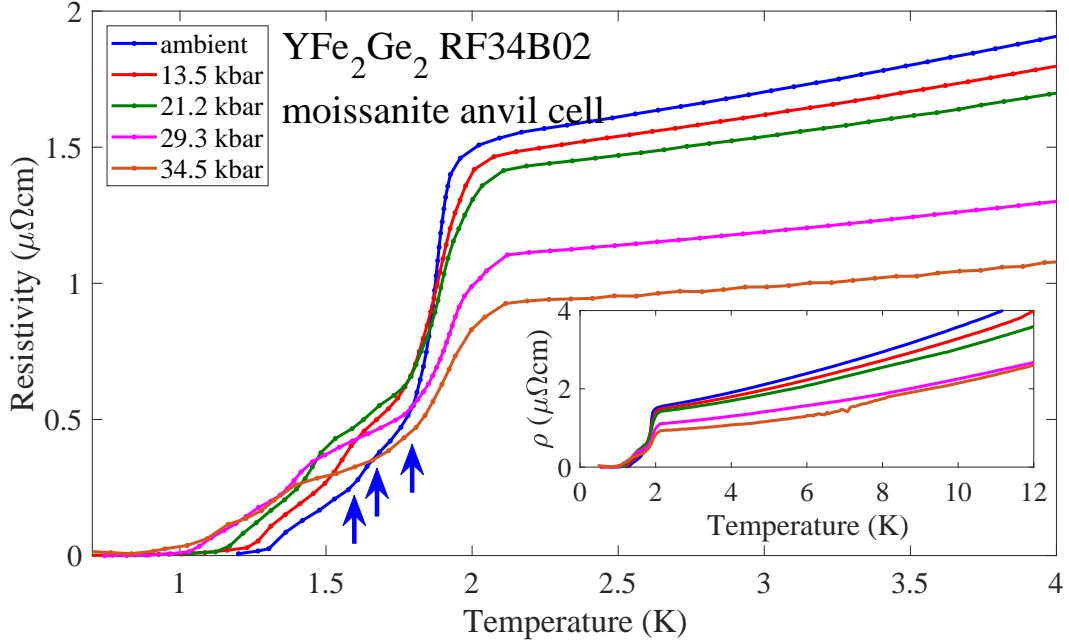
Figure 4.12: Resistivity as a function of temperature for YFe$_2$Ge$_2$ inside a moissanite anvil cell. The arrows indicate certain features observed in the transition at ambient pressure, which are also distinguishable at all other pressures (described in the text). The inset includes a wider range of temperatures. The data at 29.3 kbar and 37.0 kbar have been affected by the sample leads coming into contact with the gasket.

resistivity against temperature and of T_c against pressure are presented respectively in Figures 4.12 and 4.13. As can be seen from the first figure, the gradient of resistivity as a function of temperature undergoes a few rather abrupt changes throughout the transition. This happened, most likely, because the sample consisted of a number of phases of different homogeneity and critical temperature distribution. At all pressures it is possible to distinguish certain features in the resistivity curve. Starting in the normal state and cooling down first leads to a shoulder followed by a rather rapid decrease of resistivity. When it falls to approximately 50% of the normal state level there is a kink of positive curvature, followed by another two of respectively negative and positive curvature. The rest of the transition is relatively steady. The kinks described above are marked by the blue arrows in Figure 4.12 for the ambient pressure sweep. Figure 4.13 shows how the temperatures at which these kinks occur evolve with pressure. Sweeps at 29.3 kbar and 34.5 kbar have been affected by a formation of electrical contact between the gasket and one of the sample leads. Further increase of pressure resulted in a complete loss of signal.

Like with the piston-cylinder cell, data for the moissanite anvil cell generally shows very little variation of T_c with pressure. The midpoint of the transition (50% resistivity drop) only changes by about 0.05 K throughout the studied pressure range. The onset temperature steadily went up with pressure at approximately 0.003 K/kbar rate, but the transition completion temperature moved in the opposite direction with the gradient of
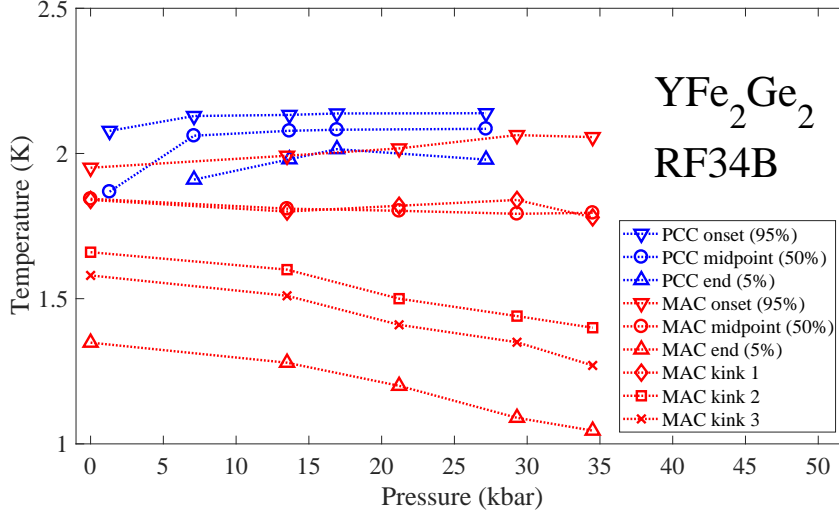
Figure 4.13: Evolution of the transition to the superconducting phase of YFe$_2$Ge$_2$ with pressure. Data from both piston-cylinder cell (PCC) and moissanite anvil cell (MAC). The percentage indicates the ratio between the actual resistivity and the normal state resistivity extrapolated to lower temperatures according to the fitted power law dependence. The kinks correspond to the features mentioned in Figure 4.12 and described in the text.

about 0.009 K/kbar. The first kink remained roughly at the same temperature at all pressures. It appears to mark the point at which the best parts of the sample (which seem to have very weak pressure dependence of T_c) became fully superconducting. The other two kinks displayed the same trend as the transition endpoint, suggesting that the poorer parts of the sample have similar negative pressure derivative of T_c. The A coefficient went down with pressure (reduced by about 30% at 21.2 kbar) but no significant change in the exponent was detected.

Inhomogeneity of the YFe$_2$Ge$_2$ samples certainly affected the observed effect of pressure on superconductivity, but it is hard to imagine only a relatively small change in the quality of the samples causing the pressure derivative of T_c to change sign. Hydrostaticity of the high pressure environment could be another factor explaining the difference between the two experiments. There are known examples of superconductivity in other 1-2-2 iron-based compounds under high pressure strongly depending on the type of pressure medium due to high sensitivity to uniaxial stress [121, 122]. Perhaps hydrostatic pressure and uniaxial stress have opposite effects on superconductivity in YFe$_2$Ge$_2$, but for the given range of pressures the hydrostaticity is expected to be fairly good.

No firm statement can be made regarding in which direction is the material tuned by high pressure relative to the QCP. In both cases the change in the A coefficient suggested tuning away from it, however A depends on more than just the effective mass, therefore cannot always be used as a reliable indicator of the quantum phase transition. Repeating the experiment and extending it to higher pressures with a carefully selected high quality sample is needed to reach a more substantial conclusion.

Finally, a comparison can be made with the results of the earlier high pressure
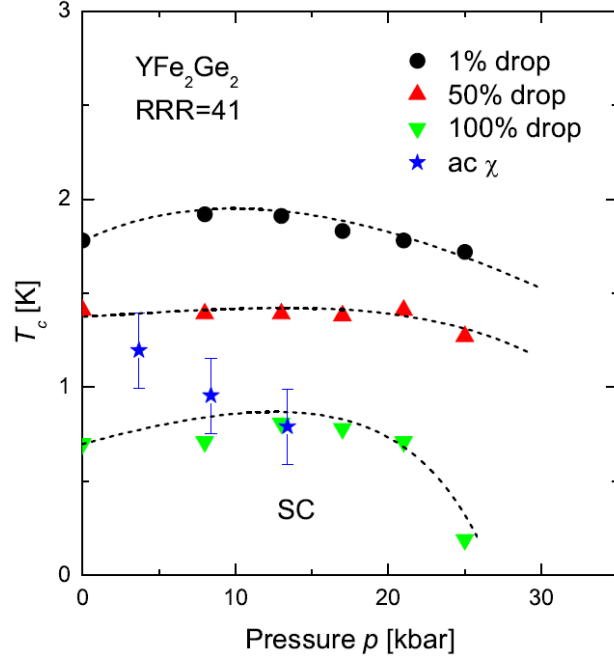
Figure 4.14: Pressure-temperature phase diagram of YFe$_2$Ge$_2$. Results obtained by Yang Zou [2] using a sample from an older generation. 1%, 50% and 100% thresholds of resistivity suppression are shown. Blue stars show the transition temperature according to the AC magnetic susceptibility measurements.

measurements described in the thesis of Yang Zou (Figure 4.14). An older sample with RRR of 41 and T_c of 1.4 K (50% level) at ambient pressure also showed weak pressure dependence below 25 kbar. Between 10 kbar and 15 kbar the T_c appeared to have a maximum, but the transition was too broad to be certain. The suppression of superconductivity at higher pressures was more rapid than in the MAC data in the present study.

4.5 Heat capacity

In order to gain evidence of the bulk superconductivity in YFe$_2$Ge$_2$ heat capacity measurements were conducted in the PPMS on various samples. Figure 4.15 displays the heat capacity data for the RF34B01 sample recorded and analysed by Dr Malte Grosche. Measurement at 2.5 T represented the normal state heat capacity with the superconductivity fully suppressed. The Sommerfeld coefficient, corresponding to the vertical position of the black line was $\gamma = 95$ mJ mol^{-1} K^{-2}. At zero field the superconducting anomaly was clearly present, but was smeared out over a fairly broad temperature range. Zero field data started to deviate from the normal state line at about 1.8 K, the same temperature at which the transition in resistivity typically started in the best samples. The bulk T_c was defined as the point at which C/T had the most negative temperature derivative. This corresponded to about 1 K temperature, which supported the hypothesis that results of the resistivity measurements only represented relatively small fractions of the samples.

Estimates of the superconducting volume fractions were made by extrapolating the
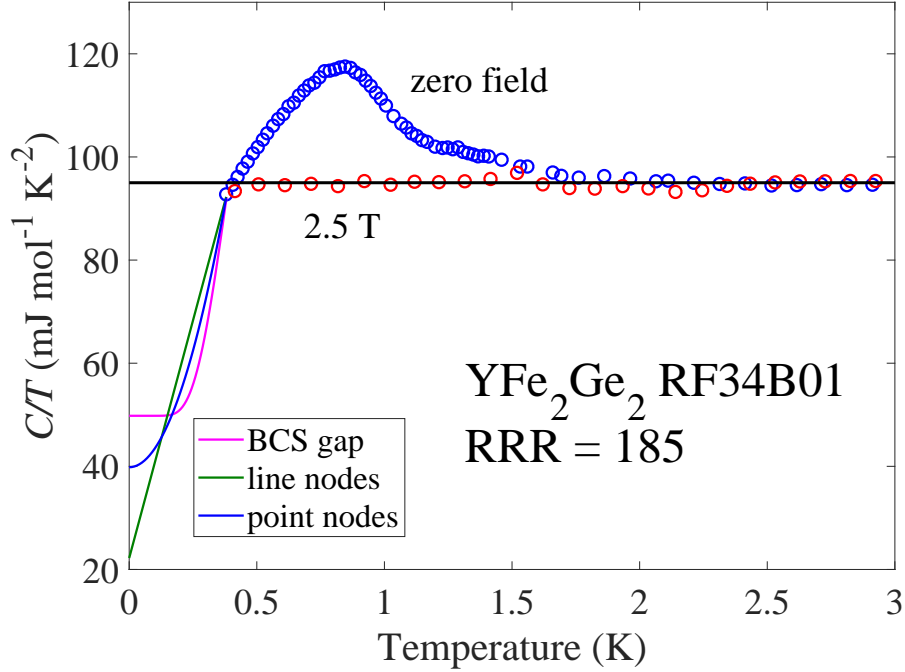
Figure 4.15: Molar heat capacity of YFe$_2$Ge$_2$ divided by temperature as a function of temperature for the RF34B01 sample [40]. Circular markers represent the experimental data without magnetic field and with 2.5 T field applied. The black horizontal line marks the normal state residual value of 95 mJ mol^{-1} K^{-2}. Lines below 0.4 K are entropy conserving extrapolations assuming various nodal structures of the superconducting gap function.

data down to zero temperature according to several models based on different nodal structures of the superconducting gap function. Besides the obvious continuity requirement the extrapolation had to ensure that the entropy S, given by

$$S(T) = \int_0^T \frac{C(T')}{T'} dT', \tag{4.1}$$

had the same value in the normal state for both zero field and 2.5 T data just above T_c. This means that the area between the black line and the zero field data above it should be the same as the corresponding area for the data below the black line. Each model assumed that at $T = 0$ there was a fraction α of the sample still in the normal state, contributing quantity $\alpha\gamma$ to C/T at all temperatures. The remaining fraction $1 - \alpha$ had a temperature dependence corresponding to different types of the gap function: proportional to T for the gap function with nodal lines [87], proportional to T^2 for the one with nodal points and proportional to $\exp(-1.5T_c/T)$ for the isotropic BCS gap [123], with the T_c also fitted. The resultant lines are plotted on the graph and the corresponding values of α were 0.24, 0.42 and 0.53 (in the same order as in the previous sentence). The BCS line has a noticeable discontinuity in the slope at the merging point and also requires $T_c = 0.72$ K, making BCS superconductivity the least fitting scenario, but even if only half of the sample was superconducting, the anomaly of such size must have come from
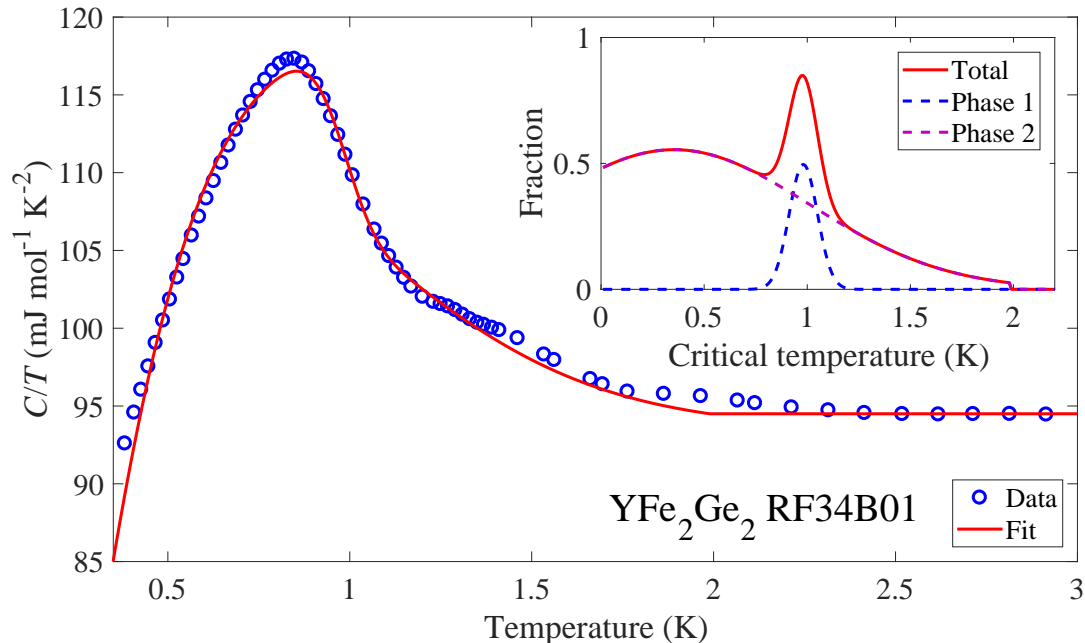
Figure 4.16: Heat capacity of YFe$_2$Ge$_2$ divided by temperature as a function of temperature fitted with a model assuming that the sample contains two distinct phases with normal distributions of T_c. The inset shows the probability distribution of the critical temperature for each phase as well as the entire sample. BCS shape of C/T was assumed for simplicity.

the main phase. For the dominant alien phase to produce such a signature its Sommerfeld coefficient would have to be of the order of 5 J mol^{-1} K^{-2} which is implausible.

Analysis presented in the previous paragraph assumed only one superconducting phase of fixed T_c, but the experimental data shown in Figure 4.15 suggested a broad distribution of T_c across the sample. This situation was roughly modelled by assuming that the sample contained potentially more than one distinct superconducting phase (grains of different stoichiometry, for instance), and each phase had a normal distribution of T_c associated with it (the model was implemented by the PhD student Jiasheng Chen). For simplicity, each small element of the sample of fixed T_c was assumed to have the BCS from of heat capacity. A cut-off critical temperature of 1.99 K was estimated by fitting the data from Figure 4.1 to the Abrikosov-Gor'kov pair breaking function modified for non-magnetic impurities in d-wave superconductors [124, 125]. As can be seen in Figure 4.16, the from of the heat capacity is captured very well by a curve resulting from a sum of two normal distributions with peak critical temperatures of 0.98 K and 0.35 K and with standard deviations of 0.068 K and 0.66 K respectively. This fit also gives 72.4% superconducting volume fraction at zero temperature. Since some of the assumptions that the model is based on are clearly unjustifiable (BCS form of heat capacity, pair breaking function for a d-wave gap), the resultant T_c distributions should not be expected to reflect the actual picture, but this approach illustrates that the proposed scenario of multiple phases, each with its own T_c distribution, is certainly plausible.

Results of heat capacity measurements on the samples from three other batches are
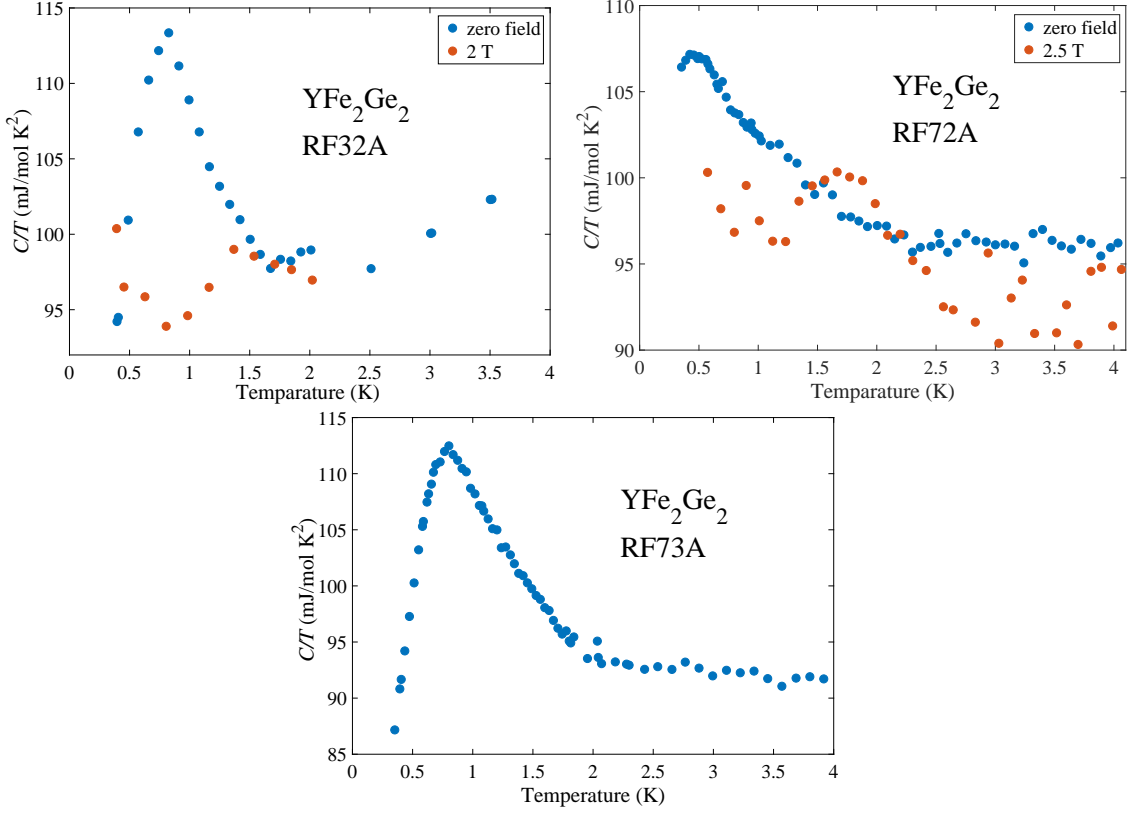
Figure 4.17: Heat capacity of YFe$_2$Ge$_2$ divided by temperature as a function of temperature for samples from batches RF32A (top left), RF72A (top right) and RF73A (bottom). Applied magnetic field fully suppressed the superconductivity in the given temperature range.

displayed in Figure 4.17. Jumps associated with the superconductivity were seen rather clearly for samples from RF32A and RF73A batches (both grown with excess iron). For the nominally stoichiometric RF72A batch the inhomogeneity of the sample appears to be so strong that the superconducting anomaly was smeared out between 0.5 K and 2 K. Readings in magnetic field turned out to be rather unstable, and did not allow to properly compare the two sweeps.

Value of the Sommerfeld coefficient can be used to estimate the effective quasiparticle mass in YFe$_2$Ge$_2$ according to the Equation 2.14. Assuming a spherical Fermi surface of the same volume as the the largest predicted Fermi surface of YFe$_2$Ge$_2$, the Fermi wavevector k_F is 0.74 Å^{-1}. This leads to the effective mass of approximately 50 electron masses.

Overall, the heat capacity measurements confirmed the bulk nature of the superconductivity in YFe$_2$Ge$_2$. Just like with the resistivity measurements, samples produced with an excess of iron show clearer signatures of the transition. It was, however, found that even in the best case the superconducting anomaly was rather broad, once again pointing at the strong inhomogeneity of the material. T_c of 1.8 K observed in the resistivity measurements represented rather small fractions of the samples, whereas only at about 1 K enough of their bulk became superconducting for the heat capacity anomaly to become visible.
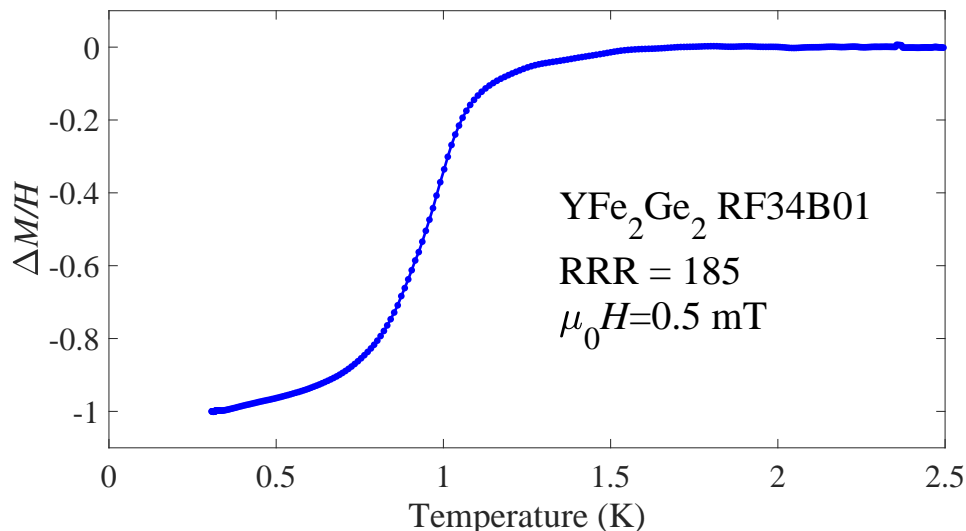
Figure 4.18: Background subtracted magnetisation of YFe$_2$Ge$_2$ divided by the applied field as a function of temperature. The sample was cooled in zero field.

4.6 Magnetisation

The low temperature magnetic susceptibility of YFe$_2$Ge$_2$ was measured and analysed by Philip Brown. A SQUID magnetometer with the helium-3 cooling was used for acquiring the data. The same RF34B01 sample, the heat capacity of which is shown in Figure 4.15, was probed. Cooling was done in zero magnetic field. Background subtracted magnetisation divided by the applied field is plotted against temperature in Figure 4.18. A step with the midpoint at 0.95 K representing a transition to the Meissner phase was seen. This temperature was consistent with the bulk T_c determined from the heat capacity measurements. Demagnetising factor was calculated by approximating the sample as a spheroid [126]. The size of the step corresponded to 95 ± 5 % diamagnetic screening.

4.7 Muon spin rotation spectroscopy

The transverse field μSR study of YFe$_2$Ge$_2$ was conducted at the Paul Scherrer Institute with the help of Dr Alex Amato, Dr Rustem Khasanov and Dr Tatsuo Goko. The purpose of this study was to compare the samples produced in the Cavendish Laboratory to the flux grown single crystals from the Ames Laboratory of the Iowa State University, which did not show clear signatures of bulk superconductivity. Data was analysed with the Musrfit software.

A sample from the RF32B batch was selected for the first run. As soon as the first set of data was obtained it became clear that ferromagnetic impurities in the iron rich sample produced a rather strong inhomogeneous internal magnetic field which very quickly desynchronised precession of antimuon spins. A nominally stoichiometric sample from the RF72A batch performed much better, as can be seen in Figure 4.19. Both sets of data were recorded at 0.2 K temperature and in 10 mT external field. For the RF32B-S1 sample antimuon spins were almost completely desynchronised after 3 µs, while for the
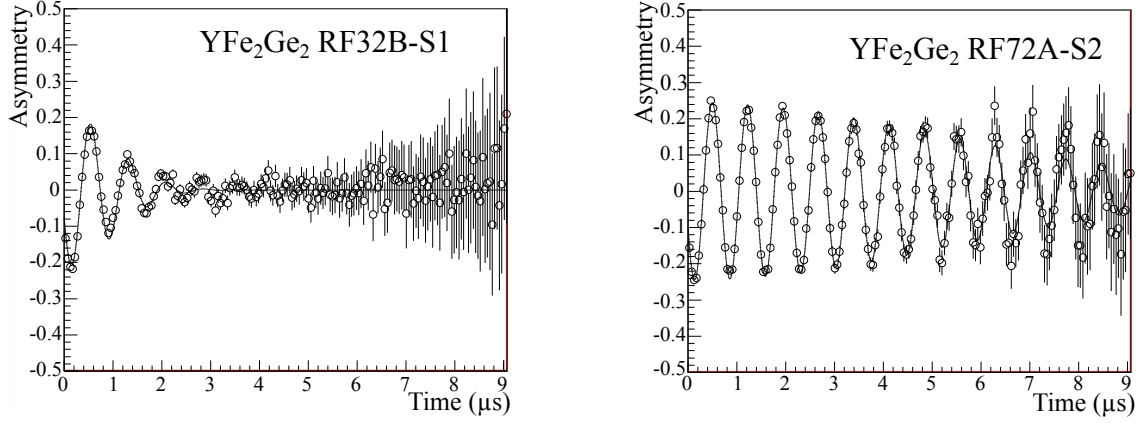
Figure 4.19: µSR asymmetry functions of two YFe$_2$Ge$_2$ samples: nominally iron rich RF32B-S1 (left) and nominally stoichiometric RF72A-S2 (right).
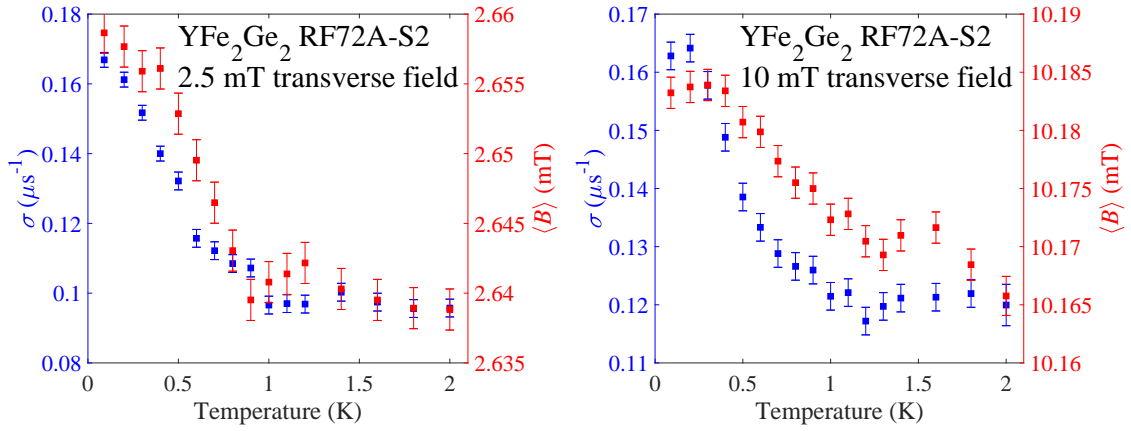

Figure 4.20: Temperature dependences of muon depolarisation rate and average internal magnetic field for YFe$_2$Ge$_2$ at 2.5 mT (left) and 10 mT (right) external transverse magnetic field.

RF72A-S2 one the asymmetry oscillations can be resolved even after 9 µs. Test with a strong permanent magnet, however, indicated that even the nominally stoichiometric sample had a detectable amount of ferromagnetic content.

The rest of the measurements were performed on the latter sample over the 0.09-2 K temperature range. 2.5 mT, 10 mT and 100 mT external magnetic fields were applied, but for the last one the data was much worse than for the first two. For a given field the data was globally fitted with the Equation 2.53. Figure 4.20 shows temperature dependence of antimuon depolarisation rates and average internal magnetic fields for 2.5 mT and 10 mT external field. Between 1 K and 2 K the depolarisation rate σ remained roughly constant. Below 1 K a clear increase in σ could be seen upon cooling. This increase was consistent with the vortex lattice formation and could serve as another piece of evidence of the bulk superconductivity in YFe$_2$Ge$_2$. The fact that the change occurred at 1 K indicated once again that this temperature was the most common bulk T_c. The shape of $\sigma(T)$, however, was rather irregular and did not display a dependence characteristic to some common gap function symmetries [127]. Kinks in the depolarisation rate are sometimes an indication of the multiple gap superconductivity, but in this case it is very likely that

the observed temperature dependence of σ was determined by a broad distribution of the critical temperature within the sample in addition to a change in the superfluid density.

The change in the depolarisation rate was accompanied by an increase in the internal magnetic field. This was unusual, since formation of the vortex lattice normally results in a diamagnetic shift of the internal field [128]. Other than attributing this to an influence of the ferromagnetic inclusions no explanation could be provided for this phenomenon.

Assuming that at the lowest temperature of 0.09 K the sample was fully superconducting, it is possible to estimate the zero temperature limit of the London penetration depth λ of YFe$_2$Ge$_2$. Since the external field was quite low, Equation 2.58 seems appropriate, and gives λ of approximately 800 nm. Using the earlier estimate of the low temperature limit of coherence length $\xi = 13$ nm and the Equation 2.39, the lower critical field for YFe$_2$Ge$_2$ at $T = 0$ was estimated to be 1 mT.

5 Quantum oscillations in pressure metallised NiS$_2$

This chapter of the thesis describes several experiments in which quantum oscillations of NiS$_2$ were measured in its high pressure metallic state. The studies were conducted on the single crystals of NiS$_2$ grown with the Te flux method by Sven Friedemann and Yiqian Xu in the Cavendish Laboratory (samples from the same batch were used in the earlier measurements headed by Hui Chang and Sven Friedemann [3]). The moissanite anvil cells (MAC) used for the described measurements were set up and pressurised by Hui Chang, using 4:1 methanol-ethanol mixture as a pressure medium. The tunnel diode oscillator (TDO) technique was used for detecting the oscillations.

5.1 Analysis of quantum oscillations

The analysis of the recorded data consisted of a number of steps.

1) First, several corrections had to be applied to the data. The magnetic field readings were obtained by converting the readings of the current flowing in the windings of the magnets. In resistive magnets in particular, these readings were noisy enough to cause deviations of the magnetic field values that corresponded to considerable fractions of the period of the high frequency quantum oscillations of NiS$_2$. This problem was eliminated by using a smoothed version of the magnetic field reading as a function of time instead of the originally recorded one. Performing this modification made the oscillations clearer, which suggested that the actual current value varied smoothly, and the noise was produced predominantly by the current measurement device. The next correction is related to the fact that even without any noise the value of the magnetic field reported by an instrument was always a little different from the actual field at the sample at the same instant. This happened for two reasons. Firstly, the position of the sample usually did not perfectly coincide with centre of the magnet. Due to a finite gradient of the field such mispositioning made the sample experience a slightly lower magnetic field than the reported one. As a result, this mismatch effectively introduced a scaling between the measured field and the actual field. Secondly, fetching the field reading from the instrument took a finite time interval. During a sweep, at the instant when the reported field value was recorded on a computer, the actual field inside the magnet was already different. The effect of this time delay depends on the field sweep rate. This causes problems when multiple sets of data recorded at different sweep rates are averaged together, since the oscillations in each set have a different phase shift. Overall, the mismatch between the actual field at the sample B_{true} and the field B_{meas} reported by the instrument at time t could be described by the following model:

$$B_{true} = \alpha \left(B_{meas} + \tau \frac{dB_{meas}}{dt} \right), \tag{5.1}$$

where α and τ are parameters which represent the shifts in the field due to the sample being not at the centre of the magnet and due to a finite response time of the instrument respectively. The TDO technique offers a neat way of determining the values of α and τ, since it happens to be sensitive to the nuclear magnetic resonances (NMR) occurring in some elements present in the circuit or in its close vicinity. The resonances manifest

themselves as sharp peaks in the signal. For a TDO oscillating at the frequency ν, the resonance for a particular element occurs at the field $B_{NMR} = \nu/\gamma$, where γ is the gyromagnetic ratio of that element. During the measurements described here it was common to see the NMR peaks due to ^{1}H from the pressure medium ($\gamma = 42.5775$ MHz T^{-1}) as well as copper isotopes ^{63}Cu and ^{65}Cu from the sensor coil ($\gamma = 11.3122\,(3)$ MHz T^{-1} and $\gamma = 12.1177\,(4)$ MHz T^{-1} respectively, which are the values for a copper metal, different from those of atomic copper; the numbers provided here were calculated by Jordan Baglo using information found in the literature [129, 130, 131, 132]). NMR peaks due to helium and fluorine (from PTFE tape) isotopes were sometimes visible as well, but they were not useful, since the parts they were coming from were quite far away from the sample. Given a number of sweeps with different sweep rates, B_{true} and B_{meas} for each sweep could be found from the TDO frequency and the apparent field at which the resonance occurred respectively. These values were then fitted to the mentioned model, and the fit gave the values of α and τ, which were used for modifying the values of the magnetic field in all sweeps. In his thesis [3] Hui Chang suggested using the absorption-dispersion NMR lineshape [133] as a model for finding B_{meas}. The accuracy of determination of α and τ depends respectively on the number of NMR peaks in a single sweep and the number of different sweep rates at which a certain peak is recorded. Another method of correcting for the time delay is empirically finding the value of τ which results in the absence of relative phase shifts between the recalibrated sweeps. This method was primarily used in this work, as not many different sweep rates were used. It was found that the mispositioning of the sample resulted in at most 2% difference between the actual and measured fields (corresponds to more than 100 T shift in frequency of the fast oscillations). The time delay reached above a second, and for the sweep rate of 1 T min^{-1} this resulted in the error of 0.016 T in magnetic field strength, which was a sizeable fraction of the period of the 6 kT frequency quantum oscillations.

2) Once the corrections had been applied, clean sets of data with visible quantum oscillations were identified for subsequent use in the analysis. If a plot of the TDO frequency against the corrected magnetic field contained a few jumps, but overall had a low noise level, then the jumps were eliminated by offsetting sections of the data so that the frequency varied continuously. In order to reduce the level of random noise in the data, multiple sweeps recorded at the same temperature were averaged together. The averaging process started with identifying a sweep with the highest density of magnetic field points and using the field values of this sweep for defining a grid, onto which the TDO frequency from all other sweeps at the same temperature was interpolated using a cubic Hermite spline interpolation. For each point of the grid the interpolated values coming from different sweeps and the value from the grid defining sweep were averaged together. Obviously, all sweeps used in the averaging had to have the same field domain.

3) Next, a subtraction of the background was required in order to get rid of the non-oscillatory part of the signal. For a smoothly varying background approximating it with a polynomial is usually sufficient (the order is typically between 5 and 20). The order

of the polynomial has to be chosen thoughtfully, as if it is too low, then some of the remaining background can be mistaken for quantum oscillations, but if it is too high, then there is a risk of subtracting part of the signal. Given how easily the TDO couples to the environment, quite often the background varied too unpredictably for it to be accounted for by a polynomial of any reasonable order. In those cases the background was approximated not by a single polynomial fitted to the entire sweep, but using a more complex procedure. A rough background subtraction is performed first (using a low order polynomial), followed by splitting the domain into a set of equally sized windows (possibly overlapping and wide enough to contain a few oscillation periods), finding the average offset for a segment of the oscillations in each window and using these offsets to produce a spline approximating the remaining background.

4) Once the background is got rid of, it is assumed that all that remains is quantum oscillations. Magnetic susceptibility oscillating with particular frequency F (which is assumed to be much higher than the maximum applied magnetic field) can be described with the relevant LK formula (Equation 2.72), expressed as

$$\Delta f_{\text{TDO}} = \frac{AT}{B^{5/2}} \frac{\exp\left(-\beta T_D m_{eff}/B\right)}{\sinh\left(\beta T m_{eff}/B\right)} \cos\left(2\pi F/B + \varphi\right), \tag{5.2}$$

where β is a constant equal to 14.639 T K^{-1}, A is the overall temperature and field independent multiplier, T_D is the Dingle temperature (measured in Kelvin), m_{eff} is the effective mass (measured in units of the free electron mass m_e), and φ is the phase shift. The typical aim of the subsequent analysis is extracting the values of F and m_{eff}. One common way of doing this involves taking a Fourier transform of the signal as a function of the inverse magnetic field. Peaks in the Fourier spectrum indicate the frequencies of the quantum oscillations present in the signal, although occasionally the spectrum can have peaks due to harmonics and mixed frequencies. Since the LK formula can be thought of as a product of cosine and a monotonically decaying (in $1/B$) envelope, its Fourier transform is expected to be a delta function convolved with some lineshape (for a given set of T, T_D and m_{eff} the lineshape is fixed). In addition, finite extent and resolution of the $1/B$ domain will further broaden the peaks. For a fixed value of B the local amplitude of quantum oscillations varies with temperature as $T/\sinh\left(\beta T m_{eff}/B\right)$ (Equation 2.64). When using the Fourier spectrum for analysis, the amplitude of particular component of quantum oscillations is typically defined as either the area under the corresponding peak or its height. However, temperature scaling of these values is only similar to the one of Equation 2.64 if the envelope does not exhibit sizeable variation throughout a sweep. Otherwise a significant discrepancy is expected for the resultant effective masses. Performing a Fourier transform numerically is usually done using the fast Fourier transform (FFT) algorithm which requires the input data to be mapped onto a uniformly spaced grid. Given that sampling is typically periodic in B, remapping the data onto a uniformly spaced grid in $1/B$ requires interpolation which, depending on the choice of the new sampling frequency, can result either in loss of information or biasing of the data.

A more rigorous way to process the data is fitting the full LK formula (potentially for

several frequencies) to the signal. For each different frequency component five parameters need to be fitted: A, T_D, m_{eff}, F and φ. It is sometimes possible to approximate the hyperbolic sine with an exponential, and simplify Equation 5.2. Such approximation was, however, inapplicable in this work. The fitting can be performed using the standard non-linear least squares fitting algorithm. When such approach was applied to individual sweeps of NiS$_2$ data, values of T_D and m_{eff} always came out orders of magnitude different from the expected ones, even despite good convergence of the fit. This was explained by the fact that these two parameters were correlated (had a similar effect on the model). Such correlation is a known weakness of the least squares fitting method. The problem could be alleviated by performing a global fit, i.e. fitting the model to the data not one temperature at a time, but rather simultaneously to all sweeps at different temperatures for a given pressure, while sharing the values of the fitting parameters. This approach worked well, producing results lying within the expected range of magnitudes, with the fit in good agreement with the data. Confidence intervals of 68% (one sigma) returned by the fitting algorithm were used as the uncertainties in the parameters.

In addition to the expected 6 kT frequency quantum oscillations the signal sometimes exhibited variation resembling lower frequency oscillations (of frequency of the order of 100 T). It was, however, impossible to quantitatively analyse these slow oscillations either because it was impossible to properly decouple them from the background, or due to the temperature range not being sufficiently wide to observe the characteristic change in their amplitude. The analysis presented in this dissertation therefore focuses exclusively on the high frequency quantum oscillations.

5.2 33 kbar and 35 kbar

In September of 2016 experiments with NiS$_2$ in a (MAC) at 33 kbar and 35 kbar pressures were conducted at the HFML, Nijmegen. The measurements were performed by Hui Chang and I with the help of the local contacts Dr Alix McCollam and Inge Leermakers. A 30 T resistive magnet and a one-shot helium-3 cryostat with the lowest temperature of 0.3 K were used. Figure 5.1 shows a part of the experimental setup. The lower pressure cell contained the NiS$_2$ sample and was fully immersed into liquid helium-3 during the measurement. The upper pressure cell was added for a backup experiment.

At 33 kbar the data was generally quite noisy, and the high frequency quantum oscillations could only be resolved at four different temperatures. A sample of the signal can be seen in Figure 5.2. The uncertainty in temperature was determined based on the stability of the thermometer reading and the temperature shift between the start and the end of the sweep. The signal had a beating in it which indicated that quantum oscillations at no less than two similar frequencies were needed to describe the data. The LK formula (Equation 5.2) with two components was used. A third frequency component was deemed unnecessary, as it did not result in a substantial improvement of the fit. Because of the low number of sweeps and a rather poor quality of the signal it was decided to constrain the conditions of the fit by making sure that both effective masses and Dingle temperatures were the same. Otherwise, the masses were
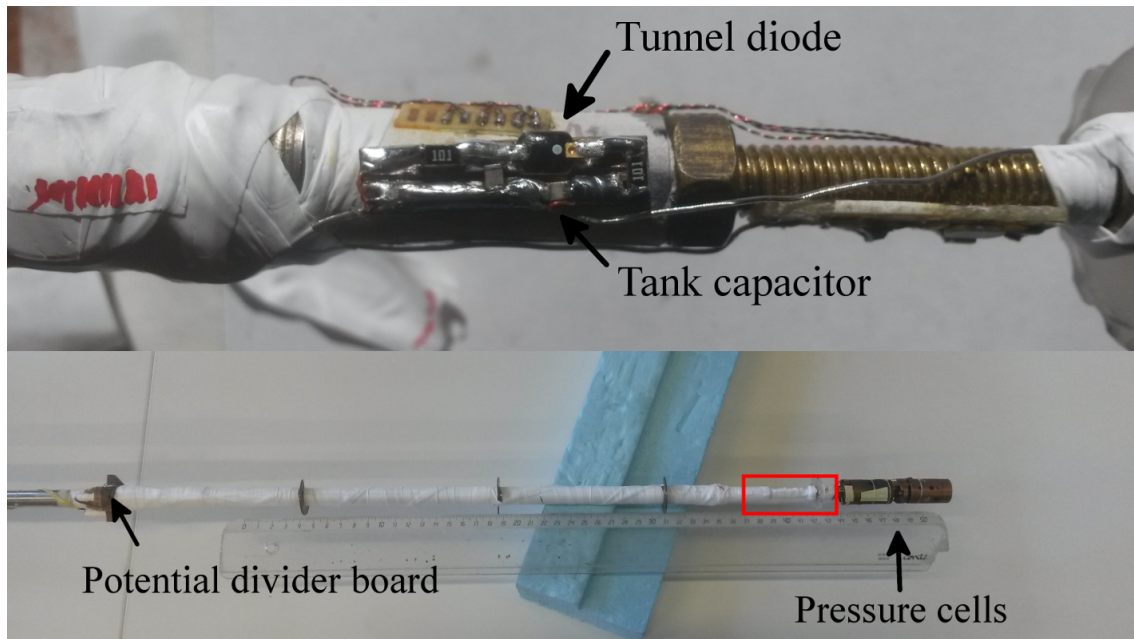
Figure 5.1: Upper image: tunnel diode board mounted on a probe of the helium-3 cryostat in the HFML, Nijmegen. Lower image: lower part of the probe. The potential divider board is located at the 1-K pot level. The red rectangle indicates the location of the tunnel diode board from the upper image.

substantially different, which was unlikely to be the case, since nearly equal frequencies indicated that both oscillations probably came from the same kind of Fermi surface, perhaps split into two versions due to a symmetry breaking.

Figure 5.3 shows the averaged and background subtracted signal at different temperatures and the global fit of the two component LK formula. Disregarding the random noise, the fit describes the amplitude of the oscillations fairly well above 25 T and always remains in phase with them. The resultant frequencies of the quantum oscillations were (5642.0 ± 1.3) T and (5826 ± 2) T. The effective mass was (6.2 ± 0.4) m_e, and the Dingle temperature was (1.64 ± 0.14) K, resulting in a mean free path of (58 ± 6) nm.

Figure 5.4 shows the results of an FFT algorithm applied to the 33 kbar data. The field domain was increased to 10-40 T interval using zero padding in order to enhance the frequency resolution. Before performing the transformation the background was approximated with a 9th order polynomial and subtracted. As can be seen in Figure 5.2, this still leaves a sizeable amount of background, which causes the low frequency end of the spectrum to have large amplitude. By looking at the variation of the spectrum with temperature it is impossible to distinguish any low frequency quantum oscillations. A peak at 5.6 kT is clearly visible, and there appears to be another smaller peak (possibly two peaks) between 5.7 kT and 6.0 kT. Due to the spectrum being rather noisy it is hard to determine the exact location, but there is no inconsistency with the frequencies obtained from the LK formula fitting. The height of the 5.6 kT peak, however, does not monotonically change with temperature. Given that FFT spectrum is technically a histogram, it is not so much the height as the area under the peak that is relevant. The
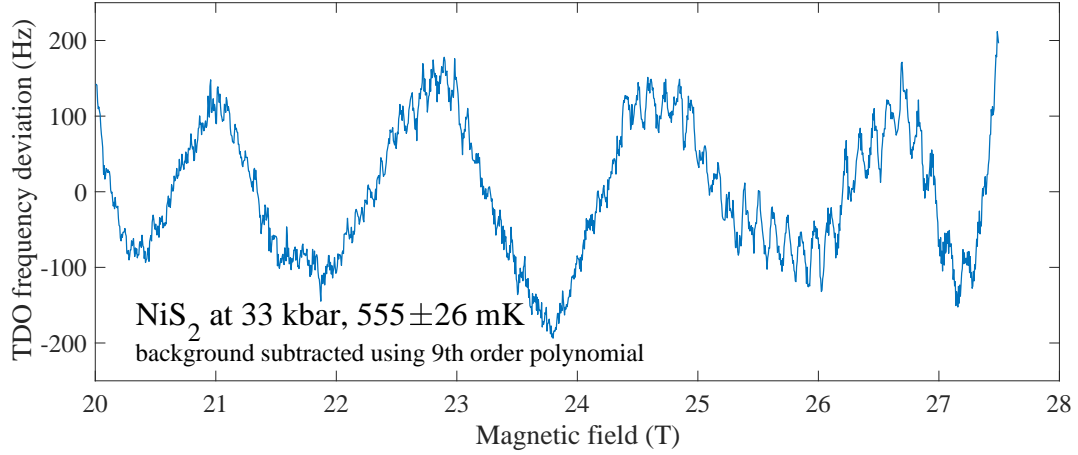
Figure 5.2: TDO signal coming from NiS2 at 33 kbar pressure and 555 mK temperature after rough background subtraction.

sweep at 814 mK has the largest domain before zero padding, therefore the corresponding peak in the spectrum is narrower, which results in increased height. For the rest of this chapter only the LK formula fitting will be used for analysis.

For the next measurement, pressure inside the cell was increased to 35 kbar. Processing the data resulted in the field sweeps with clean enough quantum oscillations at 6 different temperatures and the signal to noise ratio was on average better than before. The beating remained and the two component LK formula was used again, but this time the masses and the Dingle temperatures were not constrained to be the same. The fit is displayed in Figures 5.5 and 5.6. Its quality is slightly better than at the lower pressure, particularly at fields above 23 T. The frequencies ended up being (5704.7 ± 0.3) T and (5905.0 ± 0.6) T. The corresponding effective masses turned out to be similar: $(5.18 \pm 0.13)\ m_e$ and $(4.92 \pm 0.13)\ m_e$. The Dingle temperatures, on the other hand, were quite different: (0.49 ± 0.03) K and (2.83 ± 0.09) K, giving corresponding mean free paths of (230 ± 14) nm and (42.8 ± 1.8) nm.
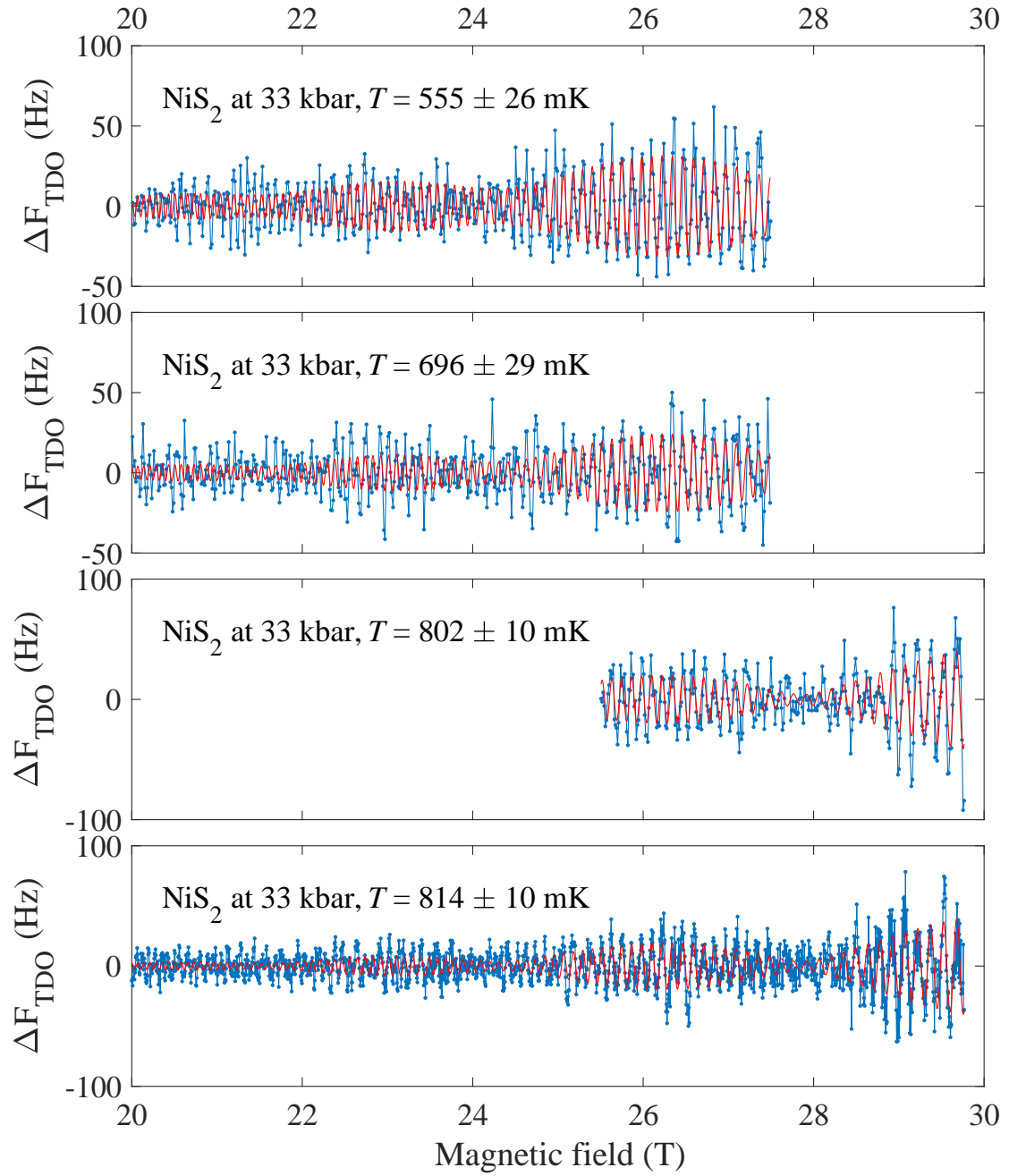
Figure 5.3: Background subtracted TDO frequency against magnetic field for NiS$_2$ at 33 kbar (blue points) and the global two component LK formula fit (red line).
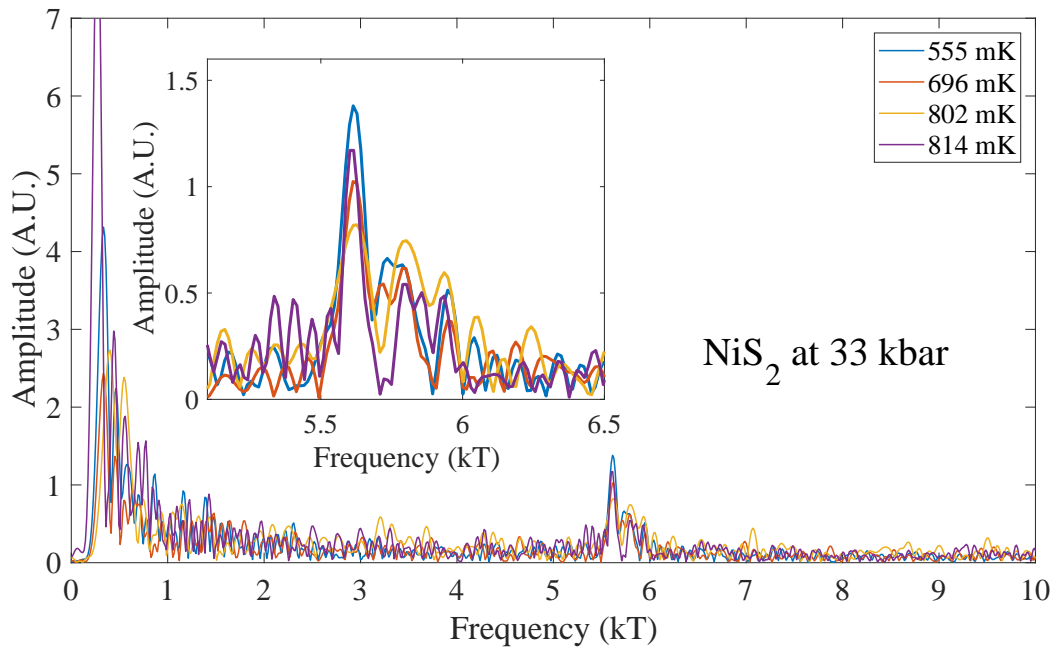
Figure 5.4: Frequency spectrum of the data for NiS2 at 33 kbar. FFT was performed after 9th order polynomial background subtraction. The inset focuses on the peaks corresponding to the high frequency quantum oscillations.
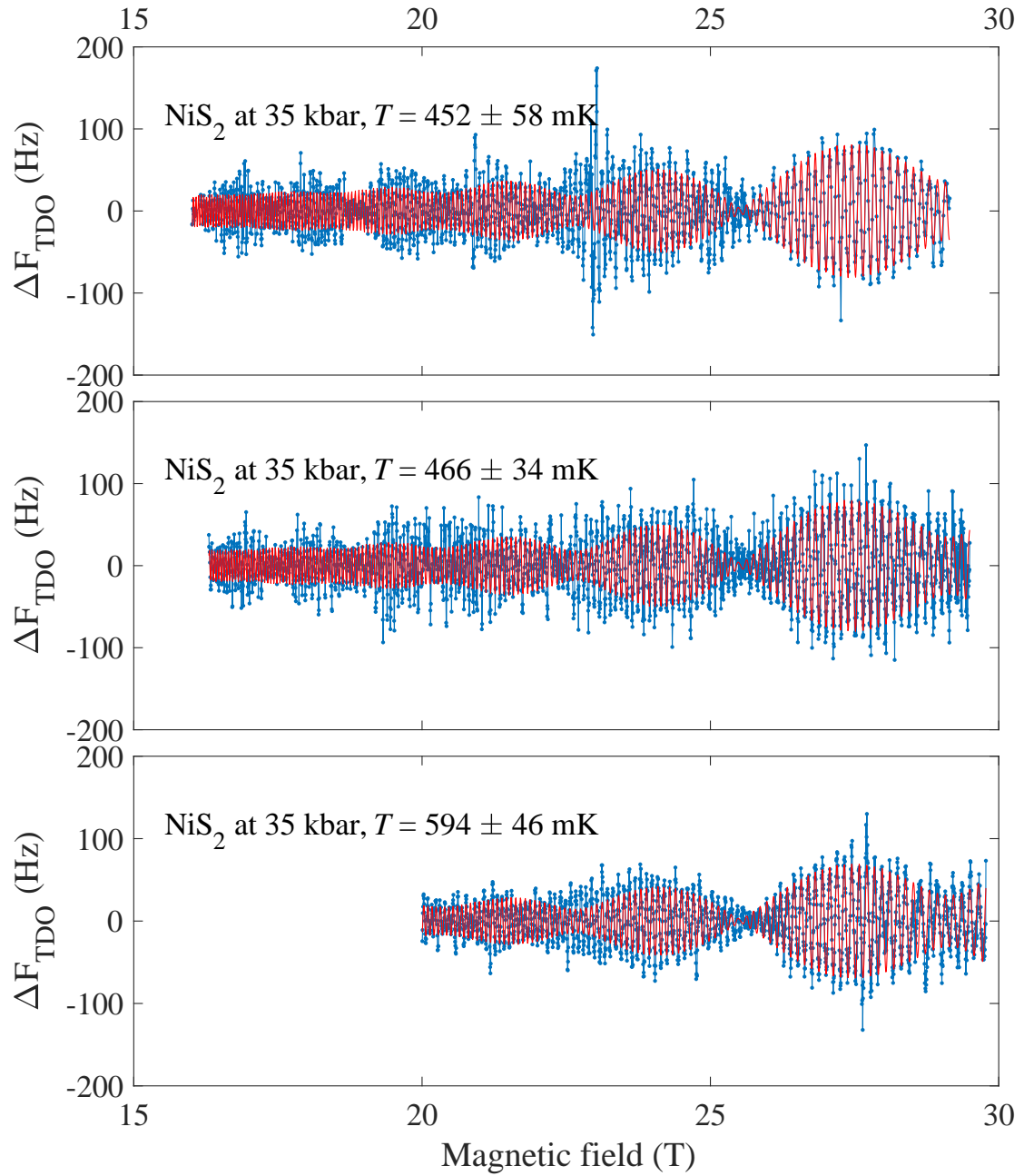
Figure 5.5: Background subtracted TDO frequency against magnetic field for NiS$_2$ at 35 kbar (blue points) and the global two component LK formula fit (red line). Figure 5.6 contains the higher temperature data for the same pressure.
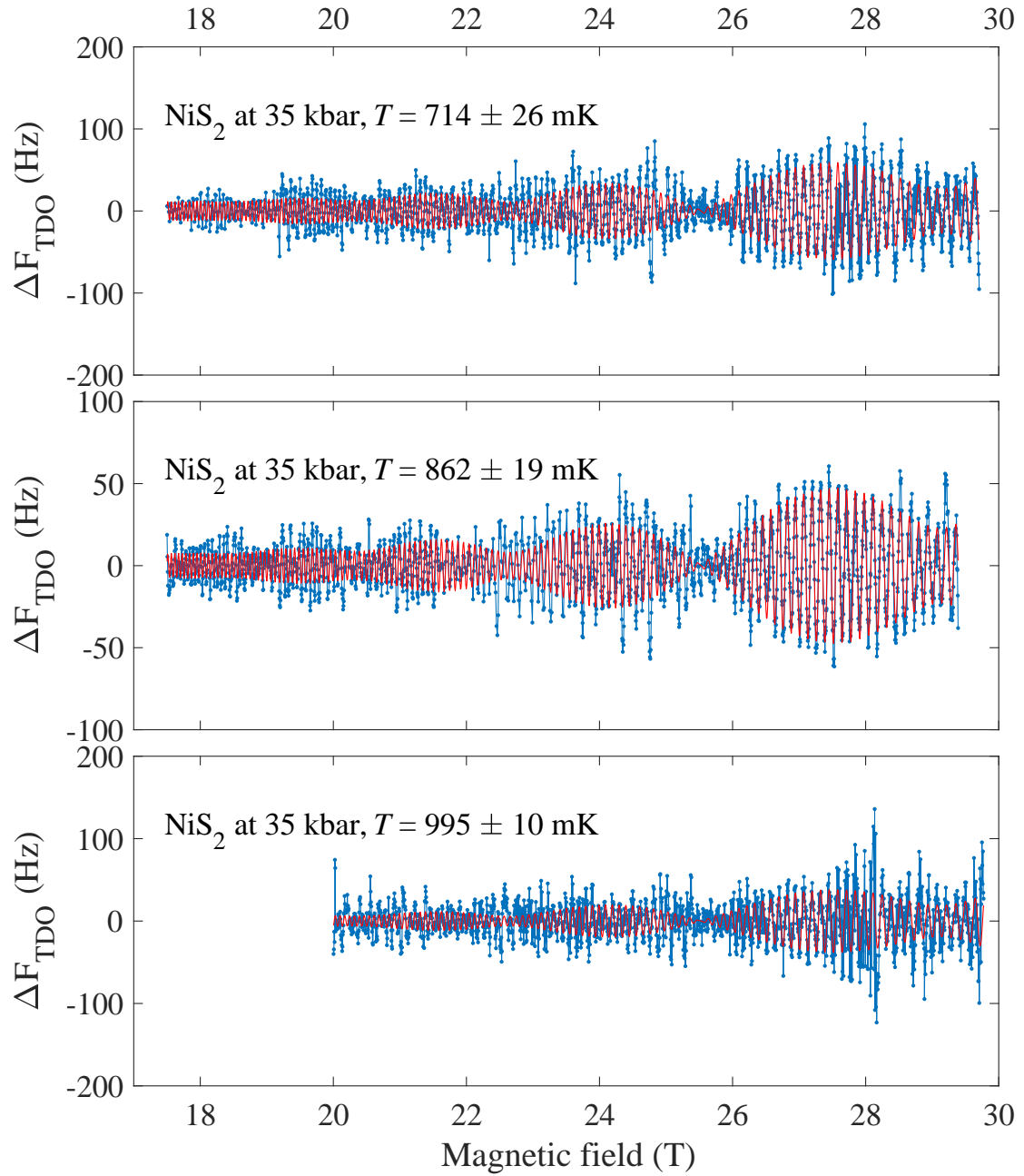
Figure 5.6: Background subtracted TDO frequency against magnetic field for NiS$_2$ at 35 kbar (blue points) and the global two component LK formula fit (red line). Figure 5.5 contains the lower temperature data for the same pressure.

5.3 50.5 kbar

In February and March of 2017 Dr Jordan Baglo and I conducted a set of experiments at the NHMFL, Tallahassee in collaboration with Dr Audrey Grockowiak, Dr William Coniglio, Dr Ju-Hyun Park and Dr Stan Tozer. For the first set of measurements a NiS$_2$ sample in a MAC pressurised to 50.5 kbar was probed in a dilution refrigerator with an 18 T superconducting magnet.

A dilution refrigerator was chosen for the experiment because the lower temperatures it provided made it more likely to observe quantum oscillations coming from the heavy electron Fermi sheets predicted by the DFT calculations (Table 1.1, [3]) yet not detected so far. The low-temperature configuration of the experiment is displayed in Figure 5.7.

The initial measurements resulted in no traces of the new Fermi surfaces, but the previously detected large cubic Fermi surface produced very clear quantum oscillations. During earlier studies at a similar pressure a three-fold splitting of the 6 kT frequency was observed, together with a fairly broad spread of the effective masses around approximately $4\,m_e$, which was unexpectedly high (Figure 1.17). This result was questioned and the measurement at 50.5 kbar provided a good opportunity to verify it. The highest temperature the dilution refrigerator could maintain was about 1 K. The lowest temperature that could be reached with the TDO powered up was 54 mK, which was about 30 mK more than without the TDO working. The inductive heating of the sample was not expected to be negligible at this temperature, but there was no way of testing exactly how strong the temperature gradient between the sample and the cell body was. For the effective mass of a few electron masses and the field of about 15 T the R_T term of the LK formula changes only by several percent between 0 and 200 mK (Equation 2.64), therefore the determination of temperature in that range should not have a significant impact on the results. With the previously mentioned prediction of at least a 9 mK temperature difference between the sample and the anvil in mind, (30 ± 20) mK value was added to the lowest temperature.

The data are shown in Figures 5.8 and 5.9. The single component fit described the data very well and no need for adding more terms to the LK formula was found. The resultant frequency of (6148.48 ± 0.03) T was consistent with the values obtained earlier, but the effective mass was merely $(1.98 \pm 0.01)\,m_e$. This value was actually more realistic than the old ones, since it followed the trend of decreasing effective mass upon the increase of pressure. The Dingle temperature was (3.72 ± 0.02) K, and the mean free path was

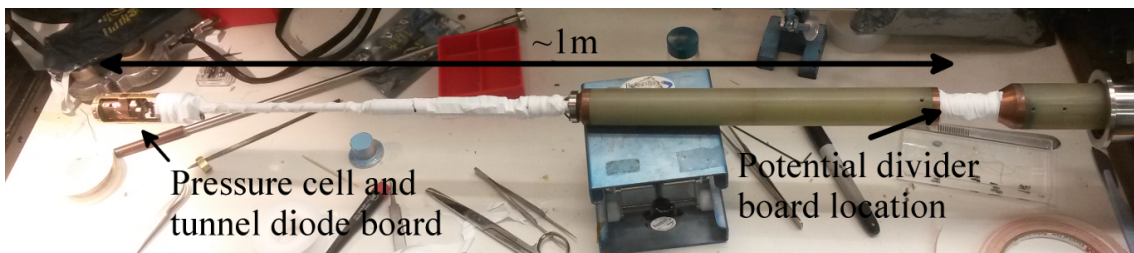Figure 5.7: Lower part of the dilution refrigerator probe used in the NHMFL, Tallahassee with the TDO circuit and the pressure cell mounted.

(82.3 ± 0.5) nm.

Figure 5.8: Background subtracted TDO frequency against magnetic field for NiS$_2$ at 50.5 kbar (blue points) and the global single component LK formula fit (red line). Figure 5.9 contains the higher temperature data for the same pressure.
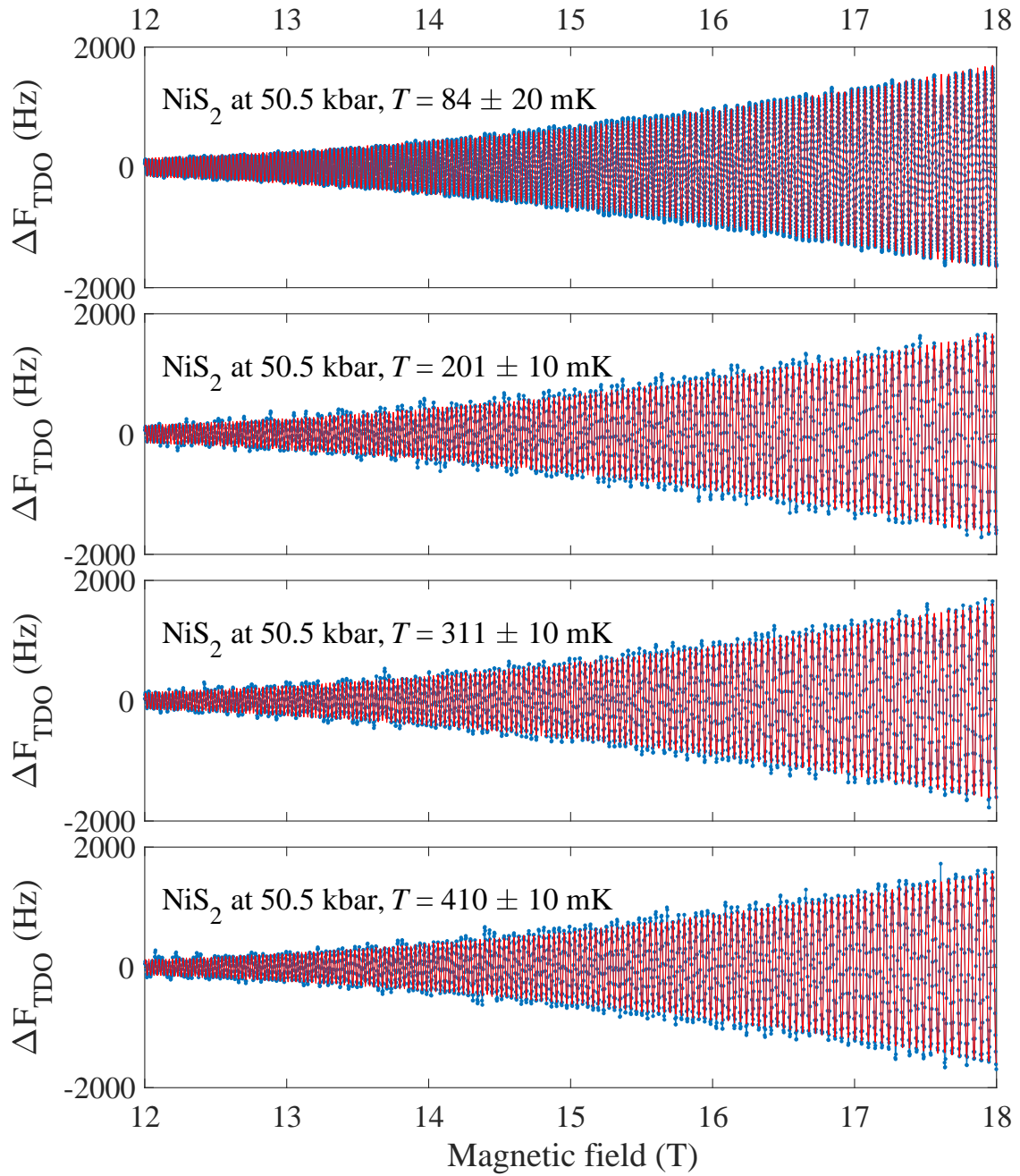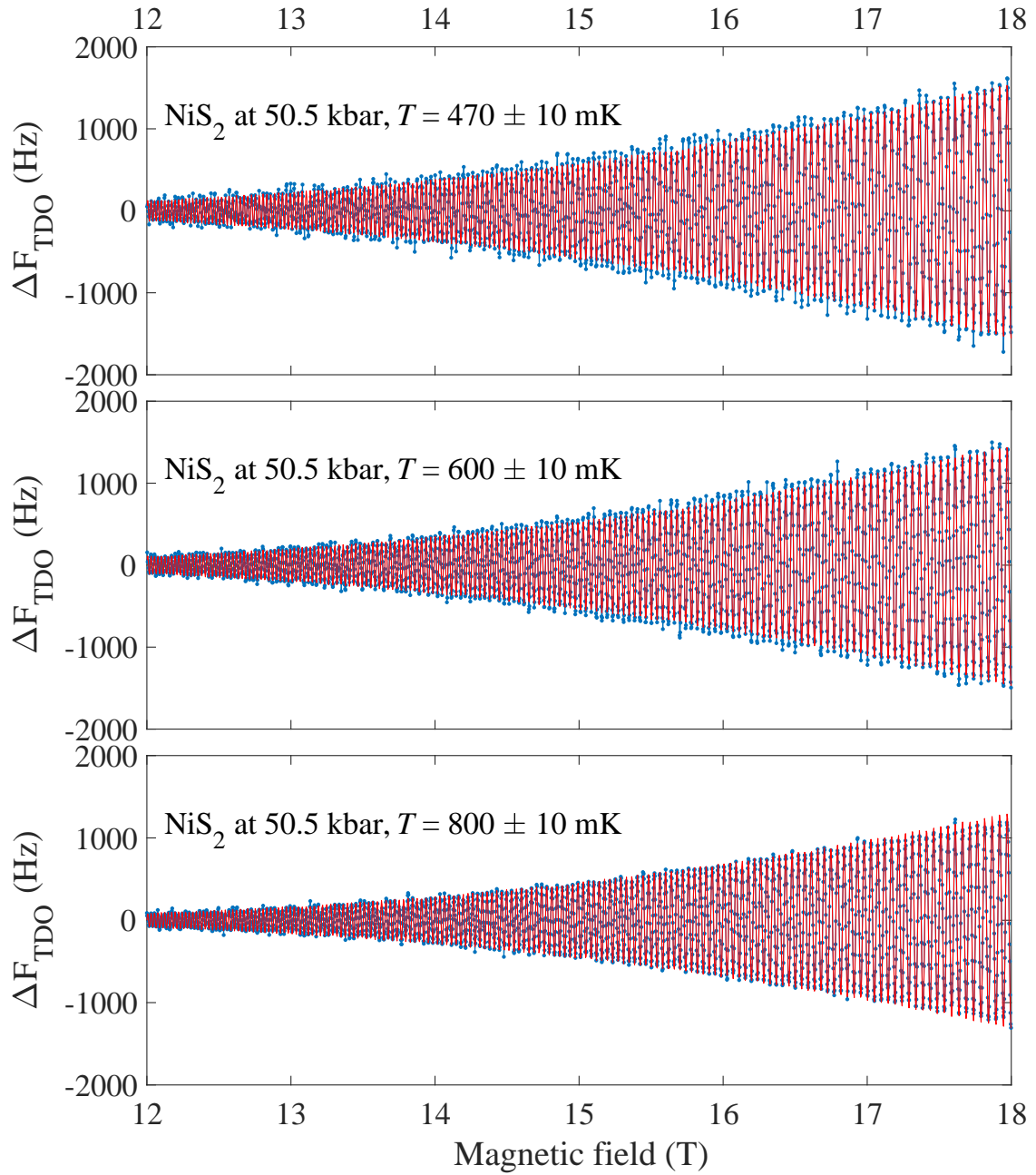
Figure 5.9: Background subtracted TDO frequency against magnetic field for NiS$_2$ at 50.5 kbar (blue points) and the global single component LK formula fit (red line). Figure 5.8 contains the lower temperature data for the same pressure.

5.4   76 kbar and 97 kbar

The rest of the experiments at the NHMFL were conducted with NiS$_2$ at 76 kbar and 97 kbar pressures, which were achieved with a diamond anvil cell set up by Dr Audrey Grockowiak. A portable dilution refrigerator and a 35 T resistive magnet were used. Quantum oscillations in NiS$_2$ have not been previously observed at such high pressures. In this region the material was supposedly close to the antiferromagnetic critical point (Figure 1.12). However, it turned out that the cubic hole Fermi surface did not undergo any significant changes in its geometry at these pressures. The 6 kT frequency quantum oscillations were present and are shown in Figures 5.10 and 5.11.

At 76 kbar the oscillations were very clear. Their amplitude changed very little across the temperature range provided by the cryostat, indicating an even lower effective mass than before (the lowest temperature reported by the mixing chamber thermometer was (35 ± 5) mK and the same estimate as before was made in order to compensate for the inductive heating). The data was well described by a single, (6276.7 ± 0.2) T frequency. The effective mass was went down to (1.33 ± 0.09) m_e. (4.2 ± 0.3) K and (111 ± 11) nm were the values obtained for the Dingle temperature and the mean free path.

The oscillations were observed at 97 kbar as well, but the signal was noisier, particularly at higher temperatures, and the amplitude of the oscillations was reduced compared to the measurements at 76 kbar, possibly due to hydrostaticity of the pressure medium becoming worse at a pressure this high. Limited time allowed us to record the oscillations only at three different temperatures. Nonetheless, the fit gave reasonable results: (6307.4 ± 0.9) T frequency, (1.9 ± 0.3) m_e effective mass, (5.4 ± 0.8) K Dingle temperature and (59 ± 11) nm mean free path.

Figure 5.10: Background subtracted TDO frequency against magnetic field for NiS$_2$ at 76 kbar (blue points) and the global single component LK formula fit (red line).
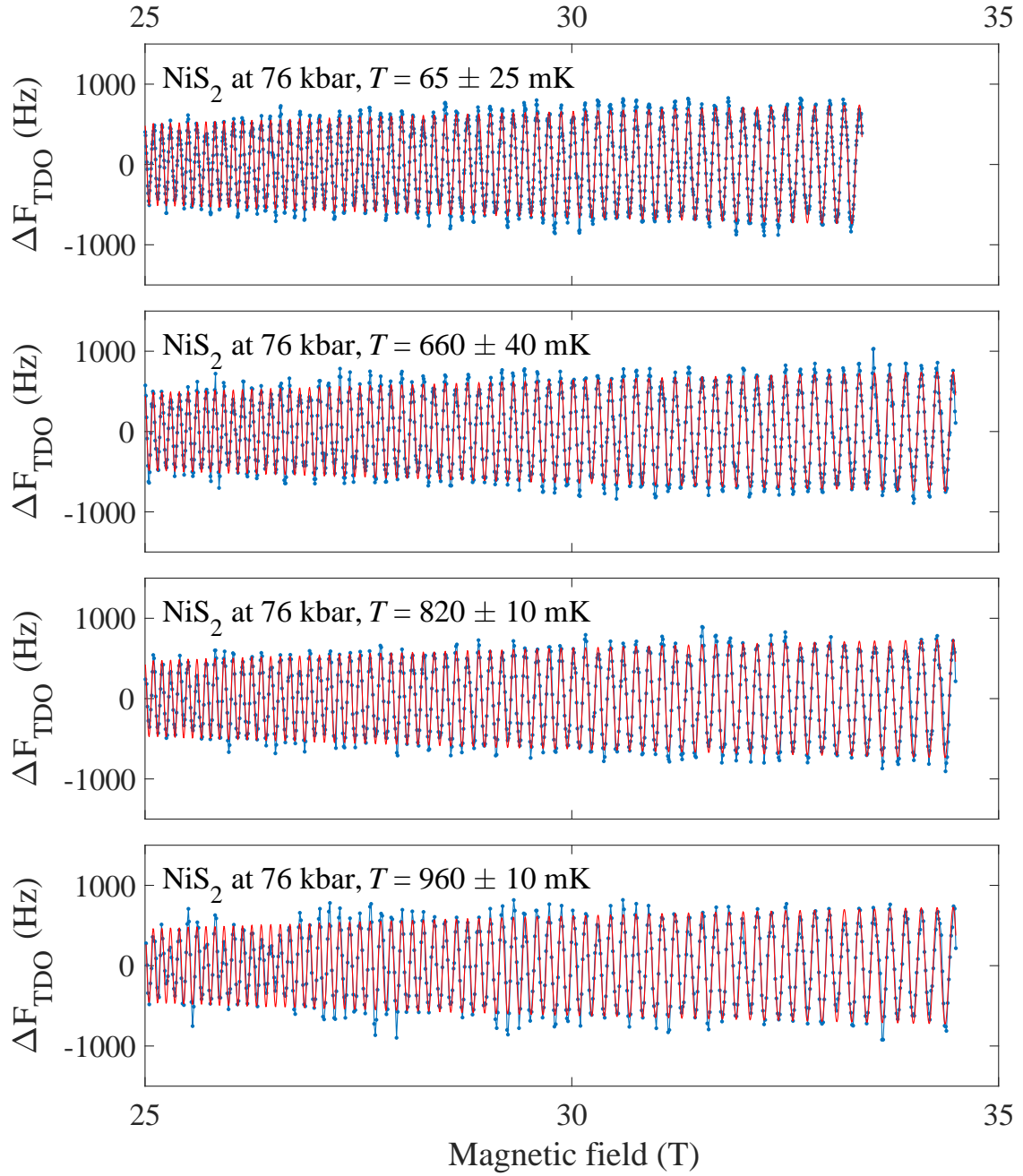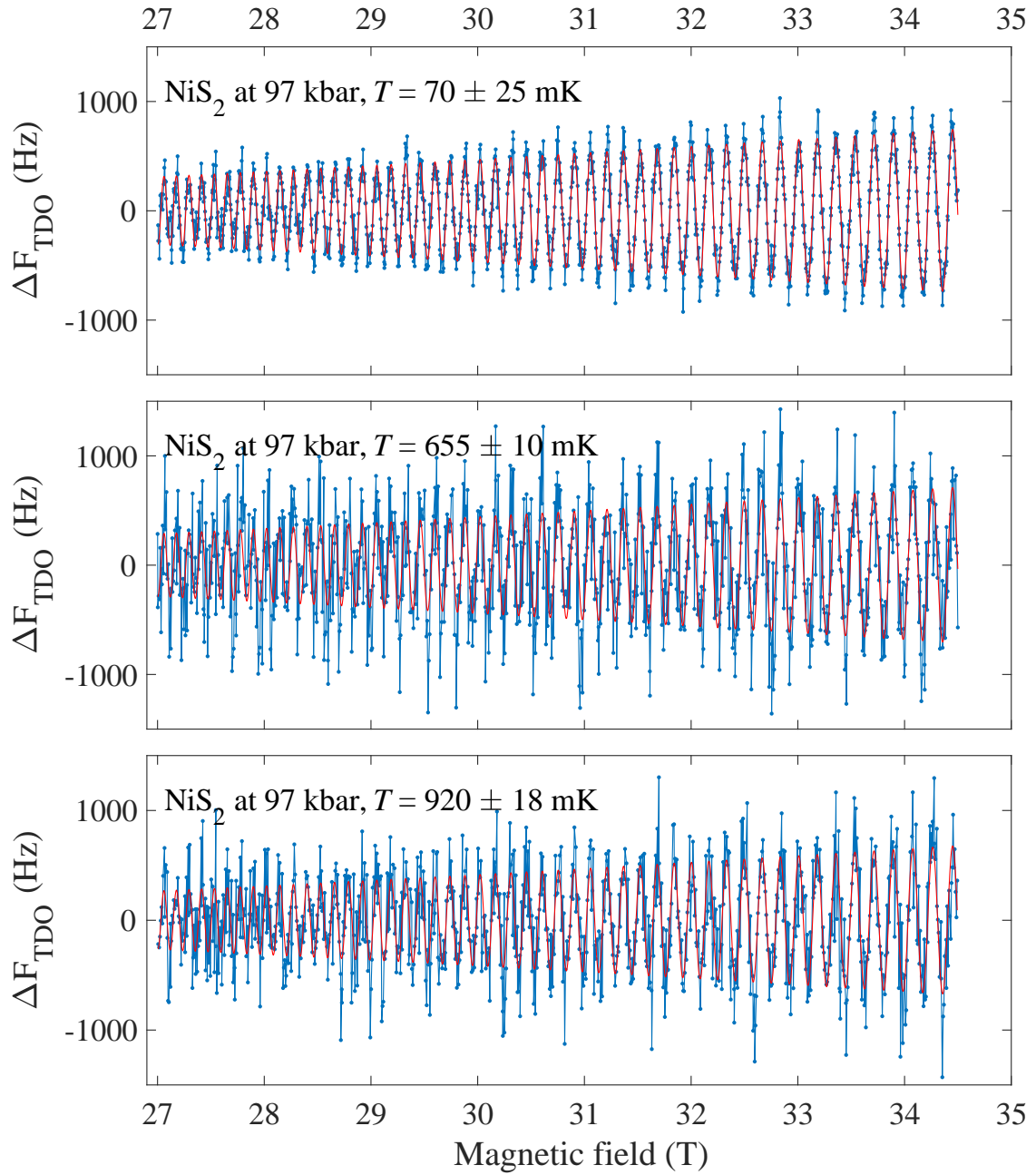
Figure 5.11: Background subtracted TDO frequency against magnetic field for NiS$_2$ at 97 kbar (blue points) and the global single component LK formula fit (red line).

5.5   Summary

The new results made it possible to track the evolution of the properties of the large Fermi surface of NiS$_2$ over a much wider pressure range than before. Figure 5.12 shows how the frequency of the quantum oscillations, and therefore the cross-sectional area of the cubic Fermi sheet, varied as a function of pressure. The dashed line indicating the trend has a slope of 5.1 T/kbar. Compression of the sample resulted in the reduction of its volume, which should have caused an increase in the carrier density and consequently the size of the Fermi surface. It was calculated [3], that the increase in the frequency due to this effect should be less than 3.9 T/kbar. Therefore, compression of the Bravais lattice alone cannot account for the change of the frequency with pressure. If the lowest two pressures are taken into consideration then the increase of the frequency with pressure becomes more pronounced. Poor quality of data for 33 kbar and 35 kbar pressures was unlikely to significantly impact the extracted frequency values, since the oscillations were visible over a fairly wide field interval. The discrepancy could have been caused by an incorrect magnetic field readout, but even if it was the case, the corrections made using the NMR peaks should have taken care of the problem. If the downturn at the lowest pressures is genuine, then it suggests that a small change in the carrier density takes place upon approaching the Mott metal-insulator transition (MIT). This is qualitatively consistent with the reduction of the net spectral weight observed in ARPES studies of selenium doped NiS$_2$ [54]. At the same time, it must be kept in mind that the relative change in frequency over the entire pressure range is merely around 10%, so the Fermi surface definitely remains large.

The analysis presented earlier in the chapter clearly indicates that at the lowest two pressures the signal contains quantum oscillations at at least two nearby frequencies. Earlier data up to a pressure of 50 kbar appeared to contain even three frequency components. This observation can be explained, at least partially, by recalling that the ground state of NiS$_2$ at the given pressures orders antiferromagnetically. As illustrated in Figure 5.13, antiferromagnetism with Q-vector (100) makes one of the principal axes of the cubic lattice inequivalent to the other two. Such symmetry breaking can also translate into the electronic structure, resulting in magnetic domains with different extremal cross sections of the Fermi surface for different directions (assuming the antiferromagnetism persists until the highest applied field). At higher pressures, the magnetic transition happens at a lower temperature, which could result in more uniform magnetic structure and the absence of splitting. This picture, however, only explains two but not three high frequency peaks. The effect of the non-colinear spin arrangement has not yet been investigated, but it is possible that it results in further splitting. A potential way to test this hypothesis would be cooling the sample down across the Néel temperature in applied magnetic field, in order to break the symmetry and cause all of the sample to have the same Q-vector. Observing no splitting would support the hypothesis.

The effective mass of the quasiparticles from the cubic Fermi surface evolved with pressure according to the plot displayed in Figure 5.14. The mass enhancement upon

getting closer to the MIT is very clear, particularly if the points for the 49.5 kbar pressure (shown in grey colour) are discarded. Assuming that $(p - p_c)/p_c$ is the tuning parameter (p is pressure and p_c is the MIT pressure), b is the associated critical exponent and a is the effective band mass (without correlations and measured in units of the free electron mass m_e), the data can be fitted with a semi-empirical model displayed on the graph. The critical pressure predicted as a result is slightly below 26 kbar, the lowest MIT pressure suggested by the high-pressure resistivity study of NiS$_2$ (Figure 1.12, [63]). In the limit of $p \gg p_c$ the effective mass tends to the value of 1.3 m_e, compared to 0.8 m_e predicted by the DFT calculations (Table 1.1). The data clearly illustrate that the effective mass enhancement is present and is undoubtedly the dominant driving force behind the Mott MIT, which is in agreement with the Brinkman-Rice model. The phase boundary between the antiferromagnetic and the paramagnetic state should have been crossed before the highest pressure was reached, but no indication of any Fermi surface reconstruction is present. There is also no sign of the potential associated quantum critical point, suggesting that the magnetic transition may be first order, especially given that 76 kbar is exactly the transition pressure predicted by the study of the resistivity power law [68].

Finally, the mean free path as a function of pressure is presented in Figure 5.15. The data appear rather disordered, primarily because of the two points corresponding to the mean free paths longer than 200 nm. Most of the other points are roughly contained within the 50-160 nm range (shaded in the figure), but no clear trend can be identified. Lack of strong suppression of the mean free path close to the MIT contradicts the reported increase in the residual resistance in that pressure region [63, 68, 134]. This suggests, that
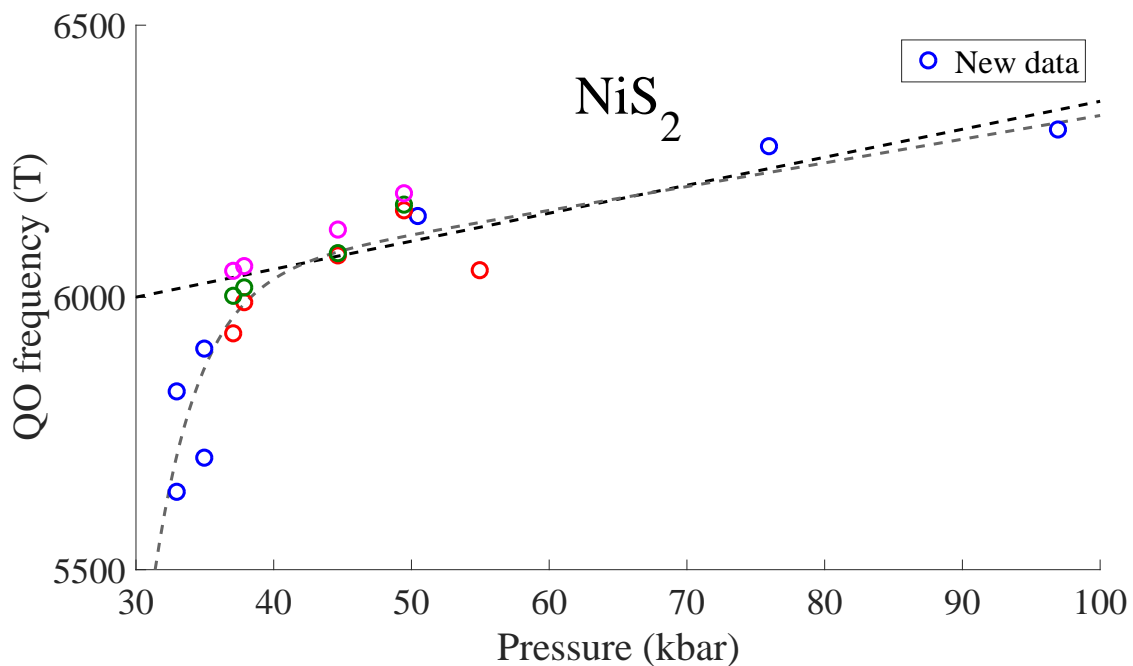

Figure 5.12: Frequency of the quantum oscillations in NiS$_2$ as a function of pressure. Blue markers correspond to the new data presented in this thesis. Dashed black line is a linear lit with the lowest two pressures excluded. Dashed grey line approximates the trend with all pressure points taken into account.
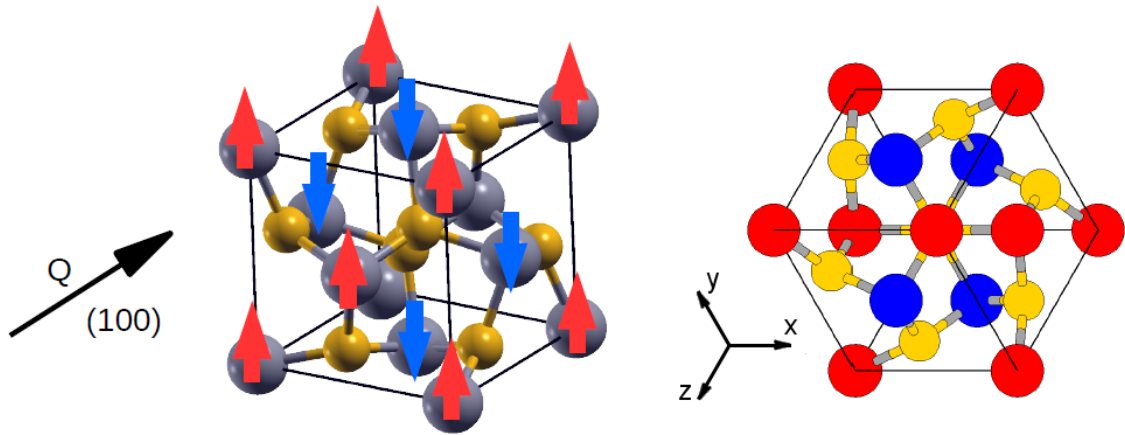
Figure 5.13: Left: arrangement of spins in the antiferromagnetic state of NiS$_2$. Right: antiferromagnetism breaking the three-fold symmetry of a cube.
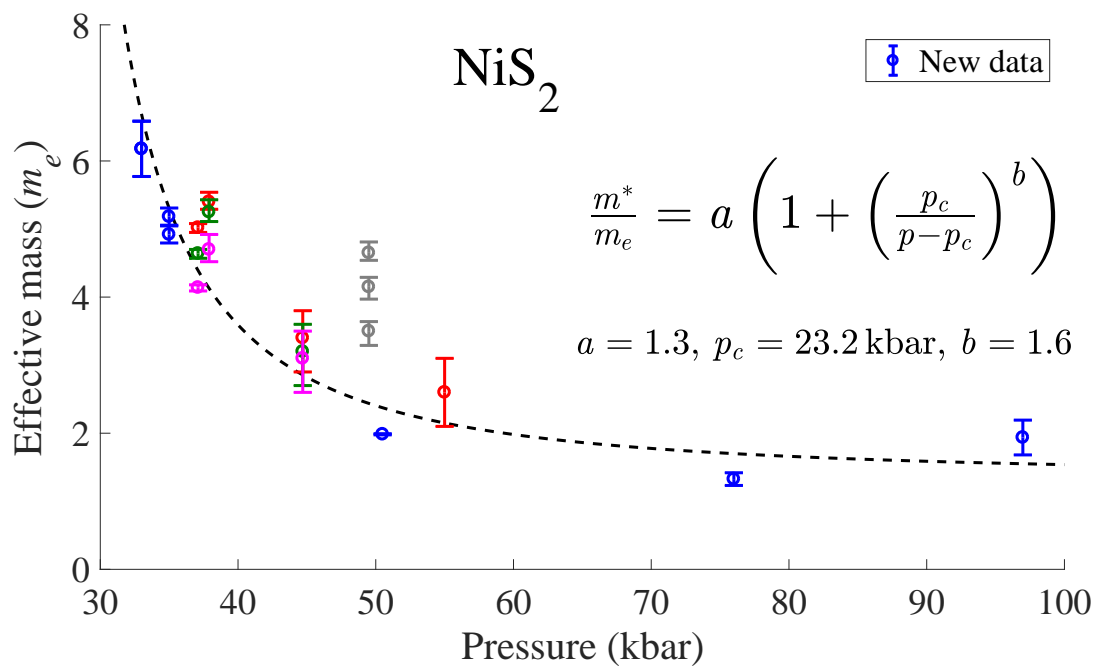
Figure 5.14: Effective mass of the hole Fermi surface of NiS$_2$ as a function of pressure. Blue markers correspond to the new data presented in this thesis. Dashed line is a fit of the displayed semi-empirical formula (the notations are explained in the text). Grey markers stand for the questionable 49.5 kbar values, which have been excluded from the fit.

Figure 5.15: Mean free path of the charge carriers of the hole Fermi surface of NiS$_2$ as a function of pressure. Blue markers correspond to the new data presented in this thesis

the latter effect is not an intrinsic property of the metallic phase of NiS$_2$, but is rather caused by the MIT occurring gradually across the sample, resulting in a gradual increase of resistivity with decreasing pressure.
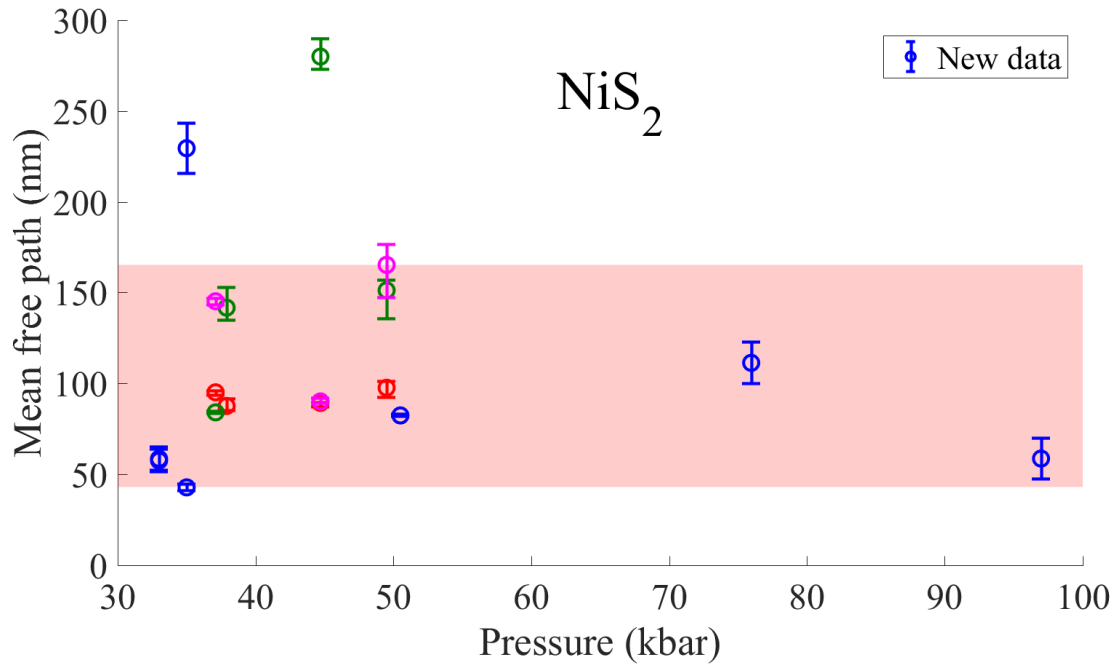
6   Conclusions

The study of YFe_2Ge_2 has benefited immensely from the advances in the material synthesis. New high quality samples demonstrated signatures of superconductivity in resistivity, heat capacity and magnetic susceptibility measurements and were more than 98% phase pure. These results allowed us to confidently classify YFe_2Ge_2 as the first non-pnictide and non-chalcogenide iron based bulk superconductor [40]. Moreover, strong correlation of the critical temperature of superconductivity with the residual resistivity ratio (RRR) as well as the extrapolation of the heat capacity data to the lowest temperatures strongly suggest that the superconductivity in YFe_2Ge_2 is unconventional, but it cannot be said at this point which gap function symmetry is favoured.

Some experiments, however, resulted in no firm conclusion. It was found that even the highest quality samples were rather inhomogeneous and high RRR of about 200 and resistive T_c of 1.8 K probably reflected the properties of a fairly small portion of the material, while most of the bulk remained in the normal state down to 1 K. The broad distribution of T_c within a single sample limited the amount of information that could be extracted from the μSR measurements. The inhomogeneity possibly also played a role in the high-pressure resistivity measurements, which did not provide a reliable indication regarding whether the material was tuned towards the quantum critical point or away from it. A measurement with more densely spaced pressure points and a more carefully selected sample could be more informative.

Now that many of the basic properties of YFe_2Ge_2 have been established, it is, perhaps, time to attempt to obtain a more detailed information about the physics of it. Besides the obvious concern about the nature of and the mechanism behind the superconductivity in the compound, there also exist questions regarding the origin of the enhanced Sommerfeld coefficient or the character of the magnetic fluctuations. It would also be interesting to find out exactly why the superconductivity is enhanced for the nominally iron rich samples and how is the excess of iron is distributed in the material. Coming close to answering some of these questions is going to require conducting more advanced experiments such as measurements of neutron diffraction or Shubnikov-de Haas oscillations, and for such techniques to work even better samples will be needed.

The work on finding ways of growing even higher quality YFe_2Ge_2 is ongoing. Techniques such as Czochralski growth, zone refinement or growth in a mirror furnace are being explored with the aim of producing larger single crystals. However, many useful measurements can still be conducted with the current generation of samples. Measuring heat capacity down to lower temperatures than before is an obvious continuation of the project. Another direction explored at the moment is the fabrication of samples for transport measurements using a focused ion beam. Over the past decade this technique of material ablation and deposition has become a very useful tool in the field of experimental condensed matter physics [135, 136]. Samples can be, for instance, machined to a shape which increases their electrical resistance by several orders of magnitude, resulting in a much stronger signal-to-noise ratio. For YFe_2Ge_2 this would

allow conducting a detailed study of the resistivity power law and possibly even measuring quantum oscillations.

The study of quantum oscillations in NiS_2 has reached a point when an important conclusion can be made. The Brinkman-Rice model of the bandwidth controlled Mott metal-insulator transition predicted that the decrease of the electrical conductivity upon approaching the phase boundary is driven not by the decrease in the charge carrier concentration, but rather by the divergence of their effective mass. The results of the measurements presented in this thesis, together with the earlier data show a rather clear mass enhancement, and it can be argued that this observation was the first time the Brinkman-Rice model was experimentally verified for a clean (i.e. not doped) system. One must admit that some parts of the presented data do not look very reliable due to the noisy data or scarcity of the temperature points at certain pressures. There is also an inconsistency with the earlier data regarding the number of frequencies that are needed to describe the observed oscillations. Analysing the whole set of available data using a single rigorous approach is already planned, but it is quite safe to say that the outcome will not be radically different, and the trends displayed by the frequency and the effective mass will remain roughly the same as they are in this thesis.

The relatively small change of the hole Fermi surface size with pressure unaccounted by the expansion of the reciprocal lattice needs to be put into consideration, as it indicates that there is, after all, a small change in the carrier density for the given Fermi surface when the MIT is approached. It would be useful to conduct additional measurements in the low pressure region in order to verify the pronounced downturn of the frequency at 33 kbar and 35 kbar pressures. At higher pressures the data is currently quite sparse and it seems a little surprising that the antiferromagnetic critical point did not have any influence on the Fermi surface. If the increase in the effective mass at 97 kbar compared to 76 kbar is genuine then it may be a sign of another, previously undetected phase transition, so doing more measurements in the 70–100 kbar range as well as even higher pressures is also a possibility for future experiments. Absence of clear signatures of the other Fermi surfaces, particularly the heavier electron sheets, is very interesting, since they have a significant contribution to the electronic properties of NiS_2. If the band masses predicted for these surfaces by the DFT calculations are enhanced similarly to the mass of the hole sheet, then their values can reach about 20 electron masses. This, possibly in combination with shorter mean free paths would result in a strong suppression of the amplitude of the oscillations, and could be the reason for their unobservability. Also, the hole Fermi surface has very small curvature, $\partial^2 A / \partial k_z^2 \approx 0$, giving a large boost to the amplitude of the quantum oscillations. The signatures of the lighter and smaller Fermi surfaces could already be present in the signal, but they were not strong enough to be clearly distinguished from the fluctuations of the TDO frequency due to coupling to the environment.

The results of the NiS_2 project are also remarkable from the methodology point of view. The probing of skin depth using the TDO was demonstrated to be a very viable approach for detecting quantum oscillations. Despite the technique being known for a long

time, the present NiS_2 study is one of the first major experimental investigations which actively and successfully uses the technique for probing the electronic structure of a crystal at pressures of the order of 10 GPa. TDO based detection is being actively adopted and optimised at various high magnetic field user facilities, and it is quite possible that the results of this project partially influenced that decision. With a massive region of phase space now accessible for study, hopefully, in the coming years there will be more similar experiments leading to great discoveries.

References

[1] B. Odom, D. Hanneke, B. D'Urso, and G. Gabrielse. New Measurement of the Electron Magnetic Moment Using a One-Electron Quantum Cyclotron. *Physical Review Letters*, **97**(3), 2006.

[2] Yang Zou. *Quantum Critical Phenomena in Intermetallic Compounds*. PhD thesis, University of Cambridge, 2014.

[3] Hui Chang. *High Pressure Quantum Oscillation Study of the Mott Insulator NiS_2*. PhD thesis, University of Cambridge, 2016.

[4] B.S. Chandrasekhar and J.K. Hulm. The electrical resistivity and super-conductivity of some uranium alloys and compounds. *Journal of Physics and Chemistry of Solids*, **7**(2-3), 259–267, 1958.

[5] B.T. Matthias, V.B. Compton, and E. Corenzwit. Some new superconducting compounds. *Journal of Physics and Chemistry of Solids*, **19**(1-2), 130–133, 1961.

[6] Hans F. Braun. Superconductivity of rare earth-iron silicides. *Physics Letters A*, **75**(5), 386–388, 1980.

[7] G. R. Stewart. Superconductivity in iron compounds. *Reviews of Modern Physics*, **83**(4), 1589–1652, 2011.

[8] J. G. Bednorz and K. A. Müller. Possible high T_c superconductivity in the Ba-La-Cu-O system. *Zeitschrift für Physik B Condensed Matter*, **64**(2), 189–193, 1986.

[9] J. Bardeen, L. N. Cooper, and J. R. Schrieffer. Theory of Superconductivity. *Physical Review*, **108**(5), 1175–1204, 1957.

[10] N. F. Berk and J. R. Schrieffer. Effect of Ferromagnetic Spin Correlations on Superconductivity. *Physical Review Letters*, **17**(8), 433–435, 1966.

[11] Yoichi Kamihara, Hidenori Hiramatsu, Masahiro Hirano, Ryuto Kawamura, Hiroshi Yanagi, Toshio Kamiya, and Hideo Hosono. Iron-Based Layered Superconductor LaOFeP. *Journal of the American Chemical Society*, **128**(31), 10012–10013, 2006.

[12] Yoichi Kamihara, Takumi Watanabe, Masahiro Hirano, and Hideo Hosono. Iron-Based Layered Superconductor La[$O_{1-x}F_x$]FeAs (x = 0.05 - 0.12) with T_c = 26 K. *Journal of the American Chemical Society*, **130**(11), 3296–3297, 2008.

[13] G Wu, Y L Xie, H Chen, M Zhong, R H Liu, B C Shi, Q J Li, X F Wang, T Wu, Y J Yan, and et al. Superconductivity at 56 K in samarium-doped SrFeAsF. *Journal of Physics: Condensed Matter*, **21**(14), 142203, 2009.

[14] Marianne Rotter, Marcus Tegel, and Dirk Johrendt. Superconductivity at 38 K in the Iron Arsenide ($Ba_{1-x}K_x$)Fe_2As_2. *Physical Review Letters*, **101**(10), 2008.

[15] Ilaria Pallecchi, Michael Eisterer, Andrea Malagoli, and Marina Putti. Application potential of Fe-based superconductors. *Superconductor Science and Technology*, **28**(11), 114005, 2015.

[16] Johnpierre Paglione and Richard L. Greene. High-temperature superconductivity in iron-based materials. *Nature Physics*, **6**(9), 645–658, 2010.

[17] Hiraku Ogino, Yutaka Matsumura, Yukari Katsura, Koichi Ushiyama, Shigeru Horii, Kohji Kishio, and Jun-ichi Shimoyama. Superconductivity at 17 K in $Fe_2P_2S_4Sc_2O_6$: a new superconducting layered pnictide oxide with a thick perovskite oxide layer. *Superconductor Science and Technology*, **22**(7), 075008, 2009.

[18] Catrin Löhnert, Tobias StÃŒrzer, Marcus Tegel, Rainer Frankovsky, Gina Friederichs, and Dirk Johrendt. Superconductivity up to 35 K in the Iron Platinum Arsenides $(CaFe_{1-x}Pt_xAs)_{10}Pt_{4-y}As_8$ with Layered Structures. *Angewandte Chemie International Edition*, **50**(39), 9195–9199, 2011.

[19] Parasharam M. Shirage, Kunihiro Kihou, Chul-Ho Lee, Hijiri Kito, Hiroshi Eisaki, and Akira Iyo. Emergence of Superconductivity in "32522" Structure of $(Ca_3Al_2O_{5-y})(Fe_2Pn_2)$ (Pn = As and P). *Journal of the American Chemical Society*, **133**(25), 9630–9633, 2011.

[20] Kazuhiko Kuroki, Seiichiro Onari, Ryotaro Arita, Hidetomo Usui, Yukio Tanaka, Hiroshi Kontani, and Hideo Aoki. Unconventional Pairing Originating from the Disconnected Fermi Surfaces of Superconducting $LaFeAsO_{1-x}F_x$. *Physical Review Letters*, **101**(8), 2008.

[21] Seiichiro Onari and Hiroshi Kontani. Violation of Anderson's Theorem for the Sign-Reversing s-Wave State of Iron-Pnictide Superconductors. *Physical Review Letters*, **103**(17), 2009.

[22] I.I. Mazin and J. Schmalian. Pairing symmetry and pairing state in ferropnictides: Theoretical overview. *Physica C: Superconductivity*, **469**(9-12), 614–627, 2009.

[23] Ronny Thomale, Christian Platt, Werner Hanke, Jiangping Hu, and B. Andrei Bernevig. Exotic d-Wave Superconducting State of Strongly Hole-Doped $K_xBa_{1-x}Fe_2As_2$. *Physical Review Letters*, **107**(11), 2011.

[24] L. Omejec and Z. Ban. Magnetic Susceptibilities of ThM_2X_2 Compounds (M = Cr, Mn, Fe, Co, Ni and Cu; X = Si and Ge). *Zeitschrift für anorganische und allgemeine Chemie*, **380**(1), 111–117, 1971.

[25] I. Felner, I. Mayer, A. Grill, and M. Schieber. Magnetic ordering in rare earth iron silicides and germanides of the RFe_2X_2 type. *Solid State Communications*, **16**(8), 1005–1009, 1975.

[26] Shoji Ishida, Setsuro Asano, and Junji Ishida. Electronic Structures of YMn_2Ge_2, $LaMn_2Ge_2$ and $LaCo_2Ge_2$. *Journal of the Physical Society of Japan*, **55**(3), 936–945, 1986.

References

[27] G. Venturini and B. Malaman. X-ray single crystal refinements on some RT_2Ge_2 compounds (R = Ca, Y, La, Nd, U; T = Mn - Cu, Ru - Pd): evolution of the chemical bonds. *Journal of Alloys and Compounds*, **235**(2), 201–209, 1996.

[28] Sandor Rozsa and Hans-Uwe Schuster. Zur Struktur von KFe_2As_2, KCo_2As_2, KRh_2As_2 / Crystal Structure of KFe_2As_2, KCo_2As_2, KRh_2As_2 and KRh_2P_2. *Zeitschrift für Naturforschung B*, **36**(12), 1981.

[29] Jian-Jun Ying, Ling-Yun Tang, Viktor V. Struzhkin, Ho-Kwang Mao, Alexander G. Gavriliuk, Ai-Feng Wang, Xian-Hui Chen, and Xiao-Jia Chen. Tripling the critical temperature of KFe_2As_2 by carrier switch. ArXiv:1501.00330, 2015.

[30] Yasuyuki Nakajima, Renxiong Wang, Tristin Metz, Xiangfeng Wang, Limin Wang, Hyunchae Cynn, Samuel T. Weir, Jason R. Jeffries, and Johnpierre Paglione. High-temperature superconductivity stabilized by electron-hole interband coupling in collapsed tetragonal phase of KFe_2As_2 under high pressure. *Physical Review B*, **91**(6), 2015.

[31] M.A. Avila, S.L. Bud'ko, and P.C. Canfield. Anisotropic magnetization, specific heat and resistivity of RFe_2Ge_2 single crystals. *Journal of Magnetism and Magnetic Materials*, **270**(1-2), 51–76, 2004.

[32] Tetsuya Fujiwara, Naofumi Aso, Hideaki Yamamoto, Masato Hedo, Yuta Saiga, Masakazu Nishi, Yoshiya Uwatoko, and Kazuma Hirota. Pressure Effect on Magnetic Short Range Ordering of $LuFe_2Ge_2$. *Journal of the Physical Society of Japan*, **76**(Suppl.A), 60–61, 2007.

[33] J. C. Slater. Atomic Radii in Crystals. *The Journal of Chemical Physics*, **41**(10), 3199, 1964.

[34] Sheng Ran, Sergey L. Bud'ko, and Paul C. Canfield. Effects of substitution on low-temperature physical properties of $LuFe_2Ge_2$. *Philosophical Magazine*, **91**(34), 4388–4400, 2011.

[35] Y. Zou, Z. Feng, P. W. Logg, J. Chen, G. Lampronti, and F. M. Grosche. Fermi liquid breakdown and evidence for superconductivity in YFe_2Ge_2. *physica status solidi (RRL) - Rapid Research Letters*, **8**(11), 928–930, 2014.

[36] H. Kim, S. Ran, E.D. Mun, H. Hodovanets, M.A. Tanatar, R. Prozorov, S.L. Bud'ko, and P.C. Canfield. Crystal growth and annealing study of fragile, non-bulk superconductivity in YFe_2Ge_2. *Philosophical Magazine*, **95**(7), 804–818, 2015.

[37] Alaska Subedi. Unconventional sign-changing superconductivity near quantum criticality in YFe_2Ge_2. *Physical Review B*, **89**(2), 2014.

[38] I. I. Mazin, D. J. Singh, M. D. Johannes, and M. H. Du. Unconventional Superconductivity with a Sign Reversal in the Order Parameter of $LaFeAsO_{1-x}F_x$. *Physical Review Letters*, **101**(5), 2008.

[39] David J. Singh. Superconductivity and magnetism in YFe_2Ge_2. *Physical Review B*, **89**(2), 2014.

[40] Jiasheng Chen, Konstantin Semeniuk, Zhuo Feng, Pascal Reiss, Philip Brown, Yang Zou, Peter W. Logg, Giulio I. Lampronti, and F. Malte Grosche. Unconventional Superconductivity in the Layered Iron Germanide YFe_2Ge_2. *Physical Review Letters*, **116**(12), 2016.

[41] J H de Boer and E J W Verwey. Semi-conductors with partially and with completely filled 3d-lattice bands. *Proceedings of the Physical Society*, **49**(4S), 59–71, 1937.

[42] N F Mott and R Peierls. Discussion of the paper by de Boer and Verwey. *Proceedings of the Physical Society*, **49**(4S), 72–73, 1937.

[43] N. F. Mott. The transition to the metallic state. *Philosophical Magazine*, **6**(62), 287–309, 1961.

[44] J. Hubbard. Electron Correlations in Narrow Energy Bands. *Proceedings of the Royal Society A: Mathematical, Physical and Engineering Sciences*, **276**(1365), 238–257, 1963.

[45] W. F. Brinkman and T. M. Rice. Application of Gutzwiller's Variational Method to the Metal-Insulator Transition. *Physical Review B*, **2**(10), 4302–4304, 1970.

[46] Martin C. Gutzwiller. Correlation of Electrons in a Narrow *s* Band. *Physical Review*, **137**(6A), A1726–A1735, 1965.

[47] Antoine Georges, Gabriel Kotliar, Werner Krauth, and Marcelo J. Rozenberg. Dynamical mean-field theory of strongly correlated fermion systems and the limit of infinite dimensions. *Reviews of Modern Physics*, **68**(1), 13–125, 1996.

[48] Gabriel Kotliar and Dieter Vollhardt. Strongly Correlated Materials: Insights From Dynamical Mean-Field Theory. *Physics Today*, **57**(3), 53–59, 2004.

[49] J. Zaanen, G. A. Sawatzky, and J. W. Allen. Band gaps and electronic structure of transition-metal compounds. *Physical Review Letters*, **55**(4), 418–421, 1985.

[50] A. Y. Matsuura, H. Watanabe, C. Kim, S. Doniach, Z.-X. Shen, T. Thio, and J. W. Bennett. Metal-insulator transition in $NiS_{2-x}Se_x$ and the local impurity self-consistent approximation model. *Physical Review B*, **58**(7), 3690–3696, 1998.

[51] Chang-Youn Moon, Hanhim Kang, Bo Gyu Jang, and Ji Hoon Shim. Composition and temperature dependent electronic structures of $NiS_{2-x}Se_x$ alloys: First-principles dynamical mean-field theory approach. *Physical Review B*, **92**(23), 2015.

[52] H. Watanabe and S. Doniach. Metal-insulator transition of the two-band Hubbard model in infinite dimension and its relevance to a strongly correlated electron system: $NiS_{2-x}Se_x$. *Physical Review B*, **57**(7), 3829–3837, 1998.

[53] Masatoshi Imada, Atsushi Fujimori, and Yoshinori Tokura. Metal-insulator transitions. *Reviews of Modern Physics*, **70**(4), 1039–1263, 1998.

[54] H. C. Xu, Y. Zhang, M. Xu, R. Peng, X. P. Shen, V. N. Strocov, M. Shi, M. Kobayashi, T. Schmitt, B. P. Xie, and et al. Direct Observation of the Bandwidth Control Mott Transition in the $NiS_{2-x}Se_x$ Multiband System. *Physical Review Letters*, **112**(8), 2014.

[55] I. H. Inoue, I. Hase, Y. Aiura, A. Fujimori, Y. Haruyama, T. Maruyama, and Y. Nishihara. Systematic Development of the Spectral Function in the $3d^1$ Mott-Hubbard System $Ca_{1-x}Sr_xVO_3$. *Physical Review Letters*, **74**(13), 2539–2542, 1995.

[56] J Caulfield, W Lubczynski, F L Pratt, J Singleton, D Y K Ko, W Hayes, M Kurmoo, and P Day. Magnetotransport studies of the organic superconductor κ-(BEDT-TTF)$_2$Cu(NCS)$_2$ under pressure: the relationship between carrier effective mass and critical temperature. *Journal of Physics: Condensed Matter*, **6**(15), 2911–2924, 1994.

[57] E. S. Choi, D. Graf, J. S. Brooks, J. Yamada, H. Akutsu, K. Kikuchi, and M. Tokumoto. Pressure-dependent ground states and fermiology in β-(BDA-TTP)$_2$MCl$_4$ (M=Fe,Ga). *Physical Review B*, **70**(2), 2004.

[58] Alexander G. Gavriliuk, Ivan A. Trojan, and Viktor V. Struzhkin. Insulator-Metal Transition in Highly Compressed NiO. *Physical Review Letters*, **109**(8), 2012.

[59] Xiaoqiang Yao and Jurgen M. Honig. Growth of nickel dichalcogenides crystals with pyrite structure from tellurium melts [NiS_2, $NiS_{2-x}Se_x$ (x≤0.7)]. *Materials Research Bulletin*, **29**(7), 709–716, 1994.

[60] Yejun Feng, R. Jaramillo, A. Banerjee, J. M. Honig, and T. F. Rosenbaum. Magnetism, structure, and charge correlation at a pressure-induced Mott-Hubbard insulator-metal transition. *Physical Review B*, **83**(3), 2011.

[61] N. Mori and T. Watanabe. Pressure effects on the magnetic transition temperatures of NiS_2. *Solid State Communications*, **27**(5), 567–569, 1978.

[62] N. Takeshita, S. Takashima, C. Terakura, H. Nishikubo, S. Miyasaka, M. Nohara, Y. Tokura, and H. Takagi. Quantum criticality and disorder in the antiferromagnetic critical point of NiS_2 pyrite. ArXiv:0704.0591, 2007.

[63] S. Friedemann, H. Chang, M. B. Gamža, P. Reiss, X. Chen, P. Alireza, W. A. Coniglio, D. Graf, S. Tozer, and F. M. Grosche. Large Fermi Surface of Heavy Electrons at the Border of Mott Insulating State in NiS_2. *Scientific Reports*, **6**(1), 2016.

[64] Akio Yoshimori and Hisao Fukuda. A Possible Model for the Weak Ferromagnetism of NiS_2. *Journal of the Physical Society of Japan*, **46**(5), 1663–1664, 1979.

[65] Katsuya Kikuchi, Tomonao Miyadai, Tsunaomi Fukui, Hiroki Itô, and Kôichi Takizawa. Spin Structure and Magnetic Properties of NiS_2. *Journal of the Physical Society of Japan*, **44**(2), 410–415, 1978.

[66] T. Miyadai, K. Takizawa, H. Nagata, H. Ito, S. Miyahara, and K. Hirakawa. Neutron Diffraction Study of NiS_2 with Pyrite Structure. *Journal of the Physical Society of Japan*, **38**, 115–121, 1975.

[67] S. Sudo. Metal-insulator transition and magnetic properties in the $NiS_{2-x}Se_x$ system. *Journal of Magnetism and Magnetic Materials*, **114**(1-2), 57–69, 1992.

[68] P. G. Niklowitz, P. L. Alireza, M. J. Steiner, G. G. Lonzarich, D. Braithwaite, G. Knebel, J. Flouquet, and J. A. Wilson. Unconventional resistivity at the border of metallic antiferromagnetism in NiS_2. *Physical Review B*, **77**(11), 2008.

[69] A. Y. Matsuura, Z. X. Shen, D. S. Dessau, C. H. Park, T. Thio, J. W. Bennett, and O. Jepsen. Electronic structure and the metal-insulator transition in $NiS_{2-x}Se_x$. *Physical Review B*, **53**(12), R7584–R7587, 1996.

[70] Cosima Schuster, Matteo Gatti, and Angel Rubio. Electronic and magnetic properties of NiS_2, $NiSSe$ and $NiSe_2$ by a combination of theoretical methods. *The European Physical Journal B*, **85**(9), 2012.

[71] J. Kuneš, L. Baldassarre, B. Schächner, K. Rabia, C. A. Kuntscher, Dm. M. Korotin, V. I. Anisimov, J. A. McLeod, E. Z. Kurmaev, and A. Moewes. Metal-insulator transition in $NiS_{2-x}Se_x$. *Physical Review B*, **81**(3), 2010.

[72] John P. Perdew, Kieron Burke, and Matthias Ernzerhof. Generalized Gradient Approximation Made Simple. *Physical Review Letters*, **77**(18), 3865–3868, 1996.

[73] D. I. Khomskii. *Basic Aspects of the Quantum Theory of Solids: Order and Elementary Excitations.* Cambridge University Press, 2010.

[74] Hilbert v. Löhneysen, Achim Rosch, Matthias Vojta, and Peter Wölfle. Fermi-liquid instabilities at magnetic quantum phase transitions. *Reviews of Modern Physics*, **79**(3), 1015–1075, 2007.

[75] P. Coleman, C. Pepin, Qimiao Si, and R. Ramazashvili. How do Fermi liquids get heavy and die? *Journal of Physics: Condensed Matter*, **13**(35), R723–R738, 2001.

[76] L.D. Landau and E.M. Lifshitz. *Statistical Physics.* Number v. 5. Elsevier Science, 2013.

[77] K. Kadowaki and S.B. Woods. Universal relationship of the resistivity and specific heat in heavy-Fermion compounds. *Solid State Communications*, **58**(8), 507–509, 1986.

[78] M. J. Rice. Electron-Electron Scattering in Transition Metals. *Physical Review Letters*, **20**(25), 1439–1441, 1968.

References

[79] T. M. Rice and W. F. Brinkman. Effects of Impurities on the Metal-Insulator Transition. *Physical Review B*, **5**, 4350–4357, 1972.

[80] F.M. Grosche, C. Pfleiderer, G.J. McMullan, G.G. Lonzarich, and N.R. Bernhoeft. Critical behaviour of ZrZn$_2$. *Physica B: Condensed Matter*, **206–207**, 20–22, 1995.

[81] F. Steglich, P. Hellmann, S. Thomas, P. Gegenwart, A. Link, R. Helfrich, G. Sparn, M. Lang, C. Geibel, and W. Assmus. "Non-Fermi-liquid" phenomena in heavy-fermion CeCu$_2$Si$_2$ and CeNi$_2$Ge$_2$. *Physica B: Condensed Matter*, **237–238**, 192–196, 1997.

[82] P. Hohenberg and W. Kohn. Inhomogeneous Electron Gas. *Physical Review*, **136**, 864–871, 1964.

[83] W. Kohn and L. J. Sham. Self-Consistent Equations Including Exchange and Correlation Effects. *Physical Review*, **140**, 1133–1138, 1965.

[84] P. G. A. de Gennes. *Superconductivity of Metals and Alloys*. Advanced Book Classics. Addison-Wesley Publishing Company, 1966.

[85] E. Helfand and N. R. Werthamer. Temperature and Purity Dependence of the Superconducting Critical Field,Hc2. II. *Physical Review*, **147**(1), 288–294, 1966.

[86] D. J. Scalapino. A common thread: The pairing interaction for unconventional superconductors. *Reviews of Modern Physics*, **84**, 1383–1417, 2012.

[87] G. E. Volovik and L. P. Gor'kov. Superconducting classes in heavy-fermion systems. *Perspectives in Condensed Matter Physics*, pages 144–155, 1985.

[88] T. D. Lee and C. N. Yang. Parity Nonconservation and a Two-Component Theory of the Neutrino. *Physical Review*, **105**(5), 1671–1675, 1957.

[89] A. Yaouanc and P.D. de Réotier. *Muon Spin Rotation, Relaxation, and Resonance: Applications to Condensed Matter*. International Series of Monogr. OUP Oxford, 2011.

[90] A Maisuradze, R Khasanov, A Shengelaya, and H Keller. Comparison of different methods for analyzing μSR line shapes in the vortex state of type-II superconductors. *Journal of Physics: Condensed Matter*, **21**(7), 075701, 2009.

[91] Hugo Keller, Annette Bussmann Holder, and K Alex Müller. Jahn–Teller physics and high-T$_c$ superconductivity. *Materials Today*, **11**(9), 38–46, 2008.

[92] L. Landau. Diamagnetismus der Metalle. *Zeitschrift für Physik*, **64**(9-10), 629–637, 1930.

[93] L. Schubnikov and W. J. de Haas. Magnetische Widerstandsvergrösserung in Einkristallen von Wismut bei tiefen Temperaturen. *Proceedings of the royal netherlands academy of arts and science*, **33**(2), 130–133, 1930.

[94] W. J. de Haas and P. M. van Alphen. The dependence of the susceptibility of diamagnetic metals upon the field. *Proceedings of the royal netherlands academy of arts and science*, **33**(10), 1106–1118, 1930.

[95] L. Onsager. Interpretation of the de Haas-van Alphen effect. *The London, Edinburgh, and Dublin Philosophical Magazine and Journal of Science*, **43**(344), 1006–1008, 1952.

[96] D. Shoenberg. The de Haas-Van Alphen Effect. *Philosophical Transactions of the Royal Society A: Mathematical, Physical and Engineering Sciences*, **245**(891), 1–57, 1952.

[97] D. Shoenberg. *Magnetic Oscillations in Metals*. Cambridge University Press, 1984.

[98] R. B. Dingle. Some Magnetic Properties of Metals. II. The Influence of Collisions on the Magnetic Behaviour of Large Systems. *Proceedings of the Royal Society of London Series A*, **211**, 517–525, 1952.

[99] I. M. Lifshitz and A. M. Kosevich. Theory of magnetic susceptibility in metals at low temperatures. *Sov. Phys. JETP*, **2**(4), 636–645, 1956.

[100] P. Kapitza. The Liquefaction of Helium by an Adiabatic Method. *Proceedings of the Royal Society of London Series A*, **147**, 189–211, 1934.

[101] F. Pobell. *Matter and methods at low temperatures*. Springer textbook. Springer-Verlag, 1992.

[102] R.C. Richardson and E.N. Smith. *Experimental Techniques In Condensed Matter Physics At Low Temperatures*. Advanced Book Program Series. Avalon Publishing, 1998.

[103] Physical Property Measurement System. https://www.qdusa.com/sitedocs/productBrochures/1070-002.pdf. Accessed in June 2017.

[104] N. Jiang, U. Lindemann, F. Giebeler, and G. Thummes. A ^{3}He pulse tube cooler operating down to 1.3 K. *Cryogenics*, **44**, 809–816, 2004.

[105] R.N. Richardson. Pulse tube refrigerator – an alternative cryocooler? *Cryogenics*, **26**(6), 331–340, 1986.

[106] A.T.A.M de Waele. Pulse-tube refrigerators: principle, recent developments, and prospects. *Physica B: Condensed Matter*, **280**(1-4), 479–482, 2000.

[107] Vitalij K. Pecharsky and Karl A. Gschneidner Jr. Magnetocaloric effect and magnetic refrigeration. *Journal of Magnetism and Magnetic Materials*, **200**(3), 44–56, 1999.

[108] S. Klotz, J.-C. Chervin, P. Munsch, and G. LeMarchand. Hydrostatic limits of 11 pressure transmitting media. *Journal of Physics D Applied Physics*, **42**(7), 075413, 2009.

References

[109] M. I. Eremets. *High Pressure Experimental Methods.* Oxford science publications. Oxford University Press, 1996.

[110] Patricia Lebre Alireza. *High Pressure Studies of Calcium Ruthenate.* PhD thesis, University of Cambridge, 2003.

[111] D. J. Dunstan and I. L. Spain. Technology of diamond anvil high-pressure cells: I. Principles, design and construction. *Journal of Physics E Scientific Instruments*, **22**, 913–923, 1989.

[112] D. J. Dunstan. Theory of the gasket in diamond anvil high-pressure cells. *Review of Scientific Instruments*, **60**, 3789–3795, 1989.

[113] J.W. Anthony, R.A. Bideaux, K.W. Bladh, and M.C. Nichols. *Handbook of mineralogy, Volume 2.* Mineral Data Publishing, 1995.

[114] High-field And Low temperature instrument (HAL-9500). https://www.psi.ch/smus/hal-9500. Accessed in June 2017.

[115] C. T. Van Degrift. Tunnel diode oscillator for 0.001 ppm measurements at low temperatures. *Review of Scientific Instruments*, **46**, 599–607, 1975.

[116] A. P. Mackenzie, R. K. W. Haselwimmer, A. W. Tyler, G. G. Lonzarich, Y. Mori, S. Nishizaki, and Y. Maeno. Extremely Strong Dependence of Superconductivity on Disorder in Sr_2RuO_4. *Physical Review Letters*, **80**(1), 161–164, 1998.

[117] H. Enoki, K. Ishida, and T. Nishizawa. Miscibility gap due to ordering in the BCC Fe-Ge system. *Metallurgical Transactions A*, **18**(13), 949–955, 1987.

[118] Keiichi Yokogawa, Keizo Murata, Harukazu Yoshino, and Shoji Aoyama. Solidification of High-Pressure Medium Daphne 7373. *Japanese Journal of Applied Physics*, **46**(6A), 3636–3639, 2007.

[119] Deepa Kasinathan, Miriam Schmitt, Klaus Koepernik, Alim Ormeci, Katrin Meier, Ulrich Schwarz, Michael Hanfland, Christoph Geibel, Yuri Grin, Andreas Leithe Jasper, and et al. Symmetry-preserving lattice collapse in tetragonal $SrFe_{2-x}Ru_xAs_2$ (x=0,0.2): A combined experimental and theoretical study. *Physical Review B*, **84**(5), 2011.

[120] Elissaios Stavrou, Xiao-Jia Chen, Artem R. Oganov, A. F. Wang, Y. J. Yan, X. G. Luo, X. H. Chen, and Alexander F. Goncharov. Formation of As-As Interlayer Bonding in the collapsed tetragonal phase of $NaFe_2As_2$ under pressure. *Scientific Reports*, **5**(1), 2015.

[121] W J Duncan, O P Welzel, C Harrison, X F Wang, X H Chen, F M Grosche, and P G Niklowitz. High pressure study of $BaFe_2As_2$ – the role of hydrostaticity and uniaxial stress. *Journal of Physics: Condensed Matter*, **22**(5), 052201, 2010.

[122] Hisashi Kotegawa, Takayuki Kawazoe, Hitoshi Sugawara, Keizo Murata, and Hideki Tou. Effect of Uniaxial Stress for Pressure-Induced Superconductor $SrFe_2As_2$. *Journal of the Physical Society of Japan*, **78**(8), 083702, 2009.

[123] R.D. Parks. *Superconductivity: Part 1 (In Two Parts)*. Taylor & Francis, 1969.

[124] A. A. Abrikosov and L. P. Gor'kov. On the Problem of the Knight Shift in Superconductors. *Sov. Phys. JETP*, **12**(2), 337, 1956.

[125] R. J. Radtke, K. Levin, H.-B. Schüttler, and M. R. Norman. Predictions for impurity-induced T_c suppression in the high-temperature superconductors. *Physical Review B*, **48**, 653–656, 1993.

[126] J. A. Osborn. Demagnetizing Factors of the General Ellipsoid. *Physical Review*, **67**, 351–357, 1945.

[127] R. Khasanov, K. Conder, E. Pomjakushina, A. Amato, C. Baines, Z. Bukowski, J. Karpinski, S. Katrych, H.-H. Klauss, H. Luetkens, A. Shengelaya, and N. D. Zhigadlo. Evidence of nodeless superconductivity in $FeSe_{0.85}$ from a muon-spin-rotation study of the in-plane magnetic penetration depth. *Physical Review B*, **78**(22), 220510, 2008.

[128] Z. Guguchia, A. Amato, J. Kang, H. Luetkens, P. K. Biswas, G. Prando, F. von Rohr, Z. Bukowski, A. Shengelaya, H. Keller, E. Morenzoni, R. M. Fernandes, and R. Khasanov. Direct evidence for a pressure-induced nodal superconducting gap in the $Ba_{0.65}Rb_{0.35}Fe_2As_2$ superconductor. *Nature Communications*, 1505.01223, **6**, 8863, 2015.

[129] E. R. Andrew. Developments in the motional narrowing of the NMR spectra of solids - microscopic and macroscopic. *Pure and Applied Chemistry*, **32**, 41–50, 1972.

[130] K. Kitagawa, H. Gotou, T. Yagi, A. Yamada, T. Matsumoto, Y. Uwatoko, and M. Takigawa. Space Efficient Opposed-Anvil High-Pressure Cell and Its Application to Optical and NMR Measurements up to 9 GPa. *Journal of the Physical Society of Japan*, 0910.1767, **79**(2), 024001–024001, 2010.

[131] O. Lutz, H. Oehler, and P. Kroneck. ^{63}Cu and ^{65}Cu Fourier transform nuclear magnetic resonance studies. *Zeitschrift für Physik A Hadrons and Nuclei*, **288**, 17–21, 1978.

[132] O. Lutz, H. Oehler, and P. Kroneck. Chemical Shifts and Coupling Constants in Copper (I)-Compounds by ^{63}Cu and ^{65}Cu FT-NMR Studies. *Zeitschrift Naturforschung Teil A*, **33**, 1021–1024, 1978.

[133] J. Keeler. *Understanding NMR Spectroscopy*. Wiley, 2011.

[134] S. Miyasaka, H. Takagi, Y. Sekine, H. Takahashi, N. Môri, and R. Cava. Metal-Insulator Transition and Itinerant Antiferromagnetism in $NiS_{2-x}Se_x$ Pyrite. *Journal of the Physical Society of Japan*, **69**, 3166, 2000.

[135] P. J. W. Moll, B. Zeng, L. Balicas, S. Galeski, F. F. Balakirev, E. D. Bauer, and F. Ronning. Field-induced density wave in the heavy-fermion compound CeRhIn$_5$. *Nature Communications*, **6**, 6663, 2015.

[136] P. J. W. Moll, L. Balicas, X. Zhu, H.-H. Wen, N. D. Zhigadlo, J. Karpinski, and B. Batlogg. Critical Current Oscillations in the Intrinsic Hybrid Vortex State of SmFeAs(O,F). *Physical Review Letters*, **113**(18), 186402, 2014.